NORTHWESTERN UNIVERSITY

Advanced Study of Electrode Materials

A DISSERTATION

SUBMITTED TO THE GRADUATE SCHOOL
IN PARTIAL FULFILLMENT OF THE REQUIREMENTS

for the degree

DOCTOR OF PHILOSOPHY

Field of Applied Physics

By

Xiao Chen

EVANSTON, ILLINOIS

December 2017

ABSTRACT

Advanced Study of Electrode Materials

Xiao Chen

Applied Physics, Northwestern University

The anode and cathode are main components in a battery system. In this dissertation, Group IV inter-metallics and $LiMn_2O_4$ are studied as anode and cathode materials for Li-ion batteries respectively. Preliminary investigation of a multi-valent cathode material for next generation batteries is also introduced.

Group IV inter-metallics electrochemically alloy with Li with stoichiometries as high as $Li_{4.4}M$ (M=Si, Ge, Sn or Pb). This provides the second highest known specific capacity (after pure lithium metal) for lithium ion batteries, but the dramatic volume change during cycling greatly limits their use as anodes in Li-ion batteries. We describe an approach to overcome this limitation by constructing electrodes using a Ge/Ti multilayer architecture. *In operando* X-ray reflectivity and *ex situ* transmission electron microscopy are used to characterize the hetero-layer structure at various lithium stoichiometries along a lithiation/delithiation cycle. The as-deposited multilayer spontaneously forms a one-dimensional $Ti_xGe/Ti/Ti_xGe$ core-shell planar structure embedded in a Ge matrix. The interfacial Ti_xGe alloy is observed to be electrochemically active and exhibits reversible phase separation (i.e. a conversion reaction). The overall multilayer structure exhibits a

2.3-fold reversible vertical expansion and contraction and is shown to have improved capacity and capacity retention with respect to a Ge film with equivalent active material thickness.

The $Li_xMn_2O_4$ (LMO) spinel is a well-established lithium ion battery cathode having a 3D framework with alternating layers of a close-packed array of oxygen, fixed Mn sites and variable Li occupation. We choose LMO epitaxial thin films as our experimental subject based on their advantage of well-defined structure and orientation. Through a systematic pathway, we optimized the deposition condition and conducting buffer layer selection for LMO epitaxial thin film preparing. In the following *operando* experiments on LMO epitaxial thin films, we observed the reorganization of Mn locations under compressive strain. This artificial strain is achieved through epitaxially bounding $LiMn_2O_4$ thin films on $SrTiO_3$ (111) substrates.

Multi-valent batteries are promising successors of current Li-ion batteries due to higher energy capacity and density. We report different electrochemical activities (i.e., extraction / insertion) of Mg^{2+} in epitaxially stabilized $MgMn_2O_4$ (MMO) thin films with distinct tetragonal and cubic phases. Tetragonal MMO shows negligible activity, while the cubic MMO exhibits reversible Mg^{2+} activity with associated changes in film structure and Mn oxidation state. These results demonstrate a novel strategy for identifying the factors that control Multi-valent cation mobility in next generation battery materials.

ACKNOWLEDGEMENTS

I would like to thank my advisors Prof. Michael Bedzyk and Dr. Paul Fenter for their support and guidance during my work at Northwestern University and Argonne National Lab. They brought me into this scientific world, showed me the direction, gave me enough space to explore and helped me face the problems I encountered during research. I also appreciate their patience to answer my questions and edit my papers.

I thank Prof. Mark Hersam and Prof. Chris Wolverton for serving on my thesis committee. Their suggestions in my thesis proposal provided me with new ideas and insights about my research.

I thank Dr. Tim Fister and Prof. Zhenxing Feng for their kindly and patient tutoring. Dr. Tim Fister taught me how to operate most of research equipment, from using potentiostat to running synchrotron X-ray beam. Prof. Zhenxing Feng, as my former groupmate and "big brother", helped me design experiments, analyze problems and even run experiments for me when I'm out of energy.

I thank Dr. D. Bruce Buchholz, Dr. Joseph Franklin and Dr. Bin Shi for helping prepare high quality thin films samples. Those are the key points for the success of my research. I thank the beamline scientists Dr. Jenia Karapetrova, Dr. Hua Zhou, Dr. Christian Schlepuetz and the manager of J.B.Cohen X-Ray Diffraction Facility Jerry Carsello for their instructions of X-ray instrument use and technical suggestions.

I'm also thankful to past and present groupmates in Argonne and Northwestern: Dr. Sang Soo Lee, Dr. Ke Yuan, Dr. Jonathan Emery, Dr. Sumit Kewalramani, Dr. Guennadi A Evmenenko, Dr. Curtis Leung, Dr. I-Chang Tung, Dr. Bohong Liu, Dr. Bor-Rong Chen, Dr. Li Zeng, Gavin Campbell, Dr. Liane Michelle Moreau, Changrui Gao, Dr. Stephanie Moffitt, Janak Thapa, Kurinji Krishnamoorthy, Boris Harutyunyan. They helped me a lot with my research as well as my social life.

I'm especially grateful to my 10-years roommate Siyuan Shi and all of my friends who shared joys and sorrows with me. They decorated and enriched my graduate life.

Finally, I would like to dedicate this dissertation to my dear parents in China. It is their love, encouragement and support without any expectation of return that help me grow up and conquer any difficulties in life and work.

LIST OF ABBREVIATIONS

AFM	Atomic-Force Microscopy
CE	Coulombic Efficiency
CTR	Crystal Truncation Rod
CV	Cyclic Voltammetry
LMO	$Li_xMn_2O_4$, Lithium Magnate
MMO	$MgMn_2O_4$, Magnesium Magnate
MV	Multivalent
PLD	Pulsed Laser Deposition
SEI	Solid/Electrolyte Interface
SRO	$SrRuO_3$, Strontium Ruthenate
STO	$SrTiO_3$, Strontium titanate
TEM	Transmission Electron Microscopy
XRD	X-ray Diffraction
XRR	X-ray Reflectivity
XPS	X-ray Photoelectron Spectroscopy

TABLE OF CONTENTS

LIST OF FIGURES

Chapter 1 : Introduction and Motivation

With the rhythm of people's living speeding up steadily, devices with high mobility become more and more favored. Cellphones are the most typical mobile device which are essential in this modern life. Besides mobile devices, another application raised up rapidly in recent years is electric vehicles (EVs). As the power supply for mobile devices and EVs, batteries attract unprecedented attention. Figure 1.1 shows the evolution of Li-ion batteries market in the past decade. The demand

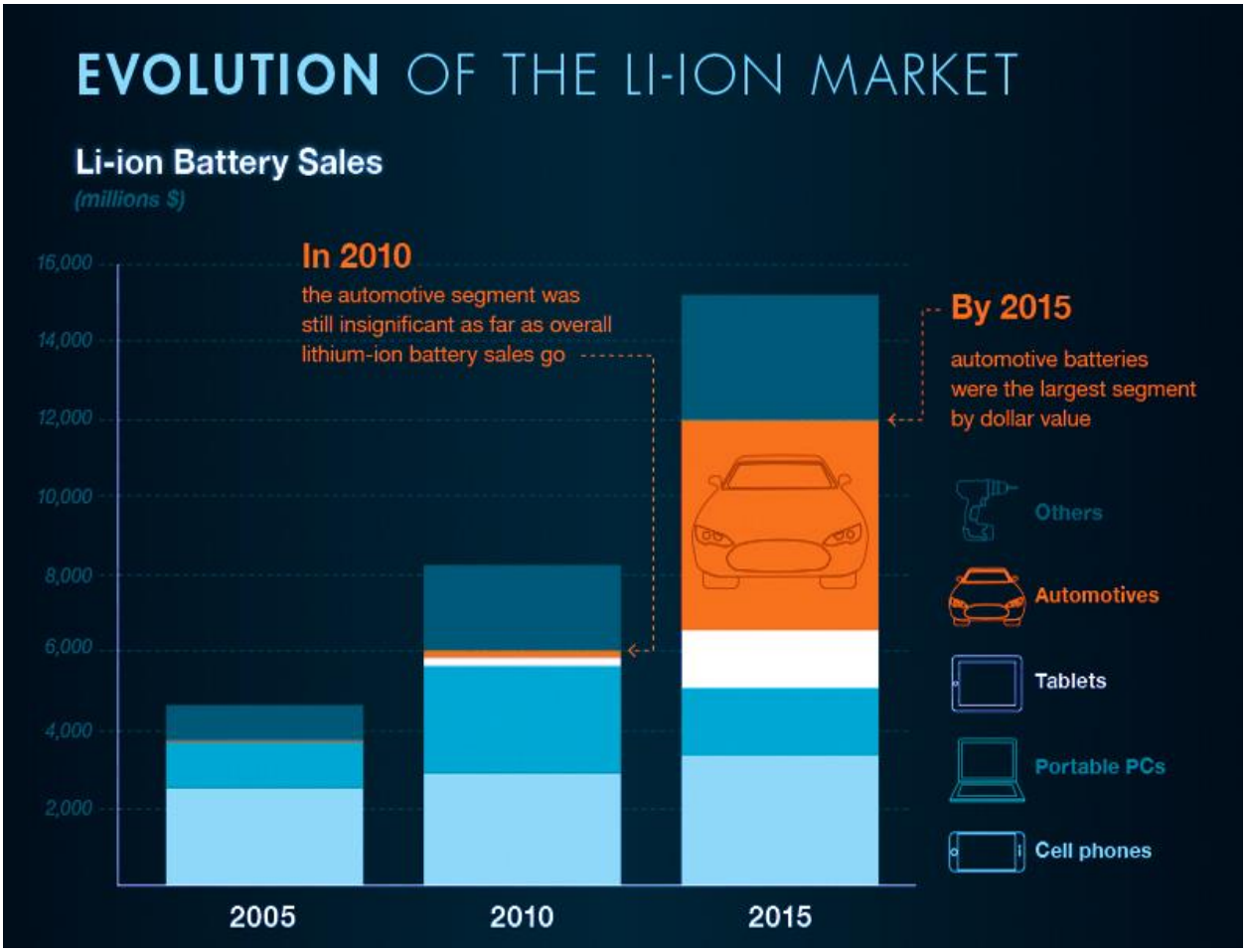

Figure 1.1 Evolution of the Li-ion battery market in past decade (from ValueWalk).

of Li-ion battery grows exponentially with nearly double of the amount every 5 years. However, this growth becomes even more explosive with the popularization of EVs. According to International Renewable Energy Agency (IRENA), the battery use for electricity could hit 250 GWh by 2030, from just 1 GWh today. Therefore, the research and study on batteries are worthwhile.

Safety, cost, lifetime, capacity and energy density are some of the main issues which should be considered when choosing battery materials. The original though for developing Li based battery technology relied on the fact that Li is the lightest metal (with equivalent weight 6.94g/mol and specific gravity 0.53g/cm^3) as well as relative low electrode potential (-3.04V relative to the standard hydrogen electrode). From cost and environment aspects, Li based battery is also a good choice due to its relatively low cost and environmental benignity.

The earliest common concept of Li battery comes from Japan. Because of its relatively low gravimetric density, Li metal was used as anode material to make primary batteries. The most remarkable one is Lithium/Silver primary battery which uses $Ag_2V_4O_{11}$ as cathode material[1]. Exxon reported the first rechargeable Li-ion batteries with cathode of layered TiS_2 and anode of metallic Li in 1976[2]. Another type of prototypical rechargeable lithium batteries work was done at Argonne National Laboratory (ANL) with Molten Salt Systems. Molten lithium and molten

sulfur were used as anode and cathode respectively[3, 4]. However, the effort to commercialize the Li-ion batteries with Li anode was not successful due to the problem of Li dendrite formation and short circuit which lead to severe safety issues[5]. To make rechargeable Li batteries more practical, researchers struggled to find new electrode material to meet the requirement of room temperature using. Over that period, numerous inorganic compounds were shown to react with alkali metals in a reversible way. The discovery of such materials was finally narrowed by the concept of electrochemical intercalation at around 1972[6]. This concept was further investigated by Besenhard and he proposed to reversibly intercalate Li-ions into graphite and oxides as anodes and cathodes, respectively[7, 8]. Based on the intercalation concept, various kinds of compounds are found and studied, including layered (e.g. $LiMO_2$[9]), spinel (e.g. LiM_2O_4[10]), olivine ($LiMPO_4$[11, 12]), silicate (e.g. Li_2MSiO_4[13]), tavorite (e.g. $LiMPO_4F$[14]) and borate (e.g. $LiMBO_3$[15]) compounds. In 1981, Goodenough first proposed to use layered $LiCoO_2$ as high energy and high voltage cathode materials. Interestingly, layered $LiCoO_2$ did not attract much attention initially[16]. In 1983, Thackeray and Goodenough identified manganese spinel as a low-cost cathode materials[17]. As to the anode aspect, it was discovered by Besenhard[7], Yazami[18], and Basu[19] that graphite, also with layered structure, could be a good candidate to reversibly store Li by intercalation/deintercalation in late 1970s and early 1980s. The modern commercial Li-ion

batteries started by Yohsion who carried out first safety test on Li-ion batteries and demonstrated enhanced safety features without ignition by dropping iron lump on the battery cells[20]. In the past two decades, there is some notable progress in the development of Li-ion batteries, particularly the introduction of low-cost cathode of $LiFePO_4$ by Goodenough[21] in 1996 and high capacity anode of C–Sn–Co by Sony[22] in 2005.

Fig 1.2 shows the structure for a traditional Graphite/$LiCoO_2$ Li-ion battery system. There are three main parts in a battery system, anode (negative electrode), cathode (positive electrode) and electrolyte. During charging process, the two electrodes are connected externally to an external

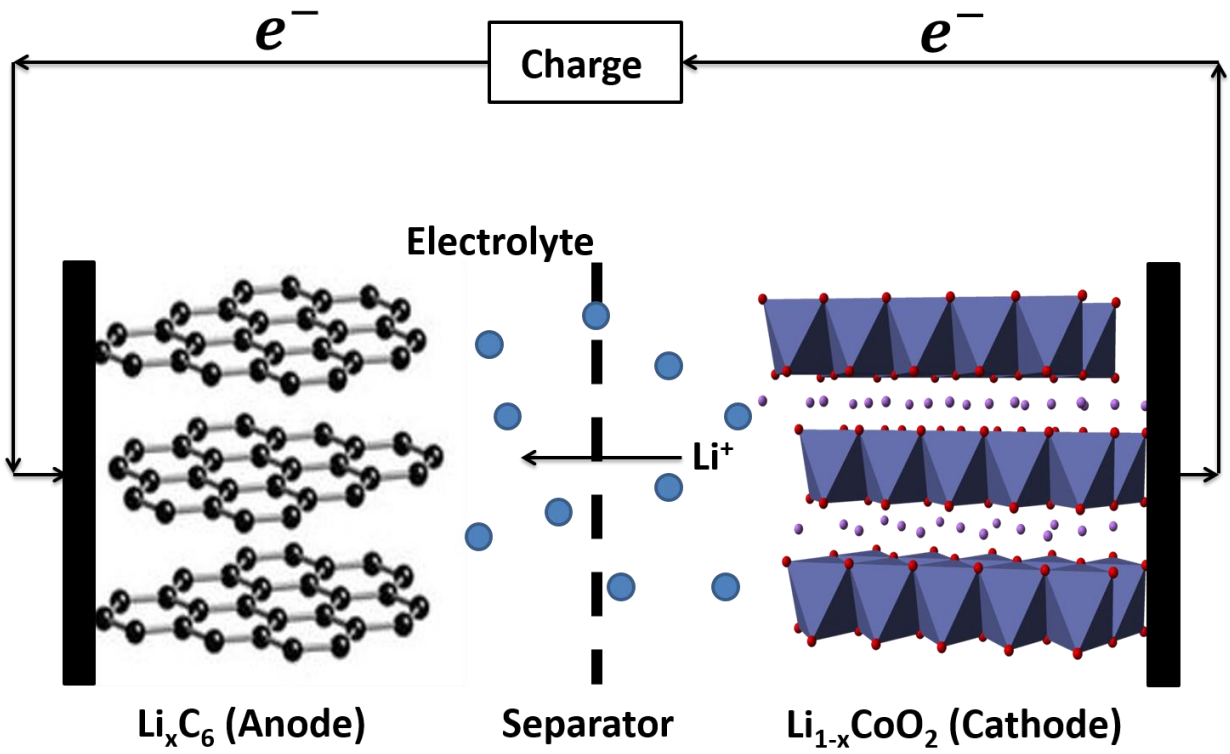

Figure 1.2 Structure of traditional Graphite/$LiCoO_2$ battery system (charging).

electrical supply. The cations in cathode are charged to higher chemical state and the extra electrons in cathode move externally to the anode. Simultaneously the lithium ions move in the same direction, but internally, from cathode to anode via the electrolyte. In this way the external energy are electrochemically stored in the battery in the form of chemical energy in the anode and cathode materials with different chemical potentials. The opposite occurs during discharging process: electrons move from anode to the cathode through the external load to do the work and Li ions move from anode to the cathode in the electrolyte. This is also known as "rocking-chair" mechanism, where the Li ions shuttle between the anode and cathodes during charge and discharge cycles[23].

The battery's performance (e.g. working potential, capacity and energy density) is related to the intrinsic property of the materials that form the cathode and anode. The capacity retention and life-time are largely dependent on the nature of the interfaces between the electrodes and electrolyte[24]. Therefore, our research mainly focuses on the study of electrode on both sides and the solid/electrolyte interface (SEI).

Chapter 2 : Background for Proposed Electrode Materials

2.1 Group IV intermetallic anode materials

In Li-ion battery ("rocking-chair" system), anode is the place to store Li ions in the charge state. Figure 2.1 shows the common categories of anode materials with their capacities and electrochemical potentials against Li/Li^+. As mentioned in battery history, pure lithium metal was use as anode material at the very beginning. Although lithium metal holds one of the highest capacities (3860 mAh/g) among anode materials, its formation of dendrites which can cause short circuit between anode and cathode[25]. Instead, graphite becomes the most popular and widely used anode material over the past decades. Graphite has low electrochemical potential (slightly above Li/Li^+ to avoid dendrite formation), good rate capability, low volume expansion during lithiation, high coulombic efficiency (CE), good electronic conductivity and is totally based on carbon which is inexpensive and abundant[26]. However, graphite can only accommodate one Li-ion per six carbon atoms with a stoichiometry of LiC_6 and thus a theoretical capacity of 372 mAh/g. Moreover, the diffusion rate of lithium into graphite is about 10^{-10} cm^2/s which largely limits power density of batteries and ultimately limits its usage in EVs. Hence, there is and urgency to replace graphite anodes to materials with higher capacity, energy and power density.

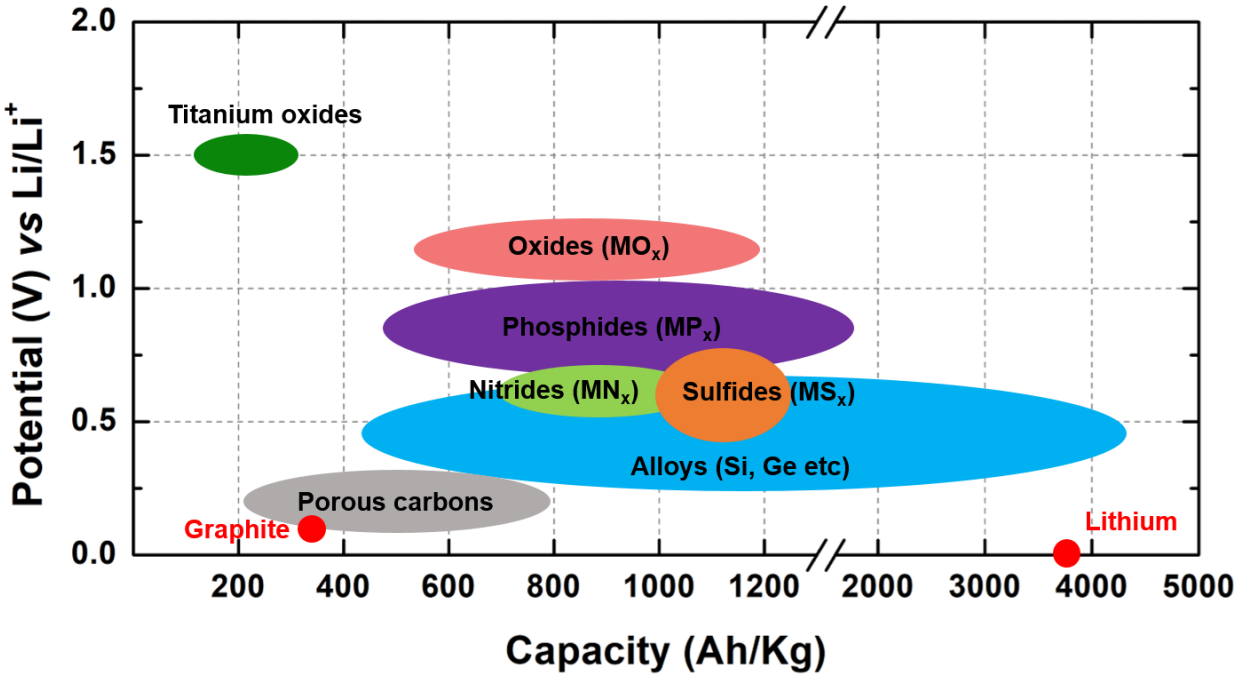

Figure 2.1 Range of average electrochemical potential and capacity of anode materials.

Many anode material candidates have been investigated. As shown in Figure 2.1, there are carbon family (e.g. carbon nanotubes, graphene, etc), intermetallic alloys, nitrides, sulfides, phosphides and oxides. Generally, anode materials can be classified into 3 groups with respect to the reaction mechanism[27].

1) Intercalation materials, such as carbon based materials, $Li_4Ti_5O_{12}$, etc.;
2) Alloy materials, such as Si, Ge, Al, etc.;
3) Conversion materials, such as transition metal oxides, metal sulphides, metal phosphides and metal nitrides.

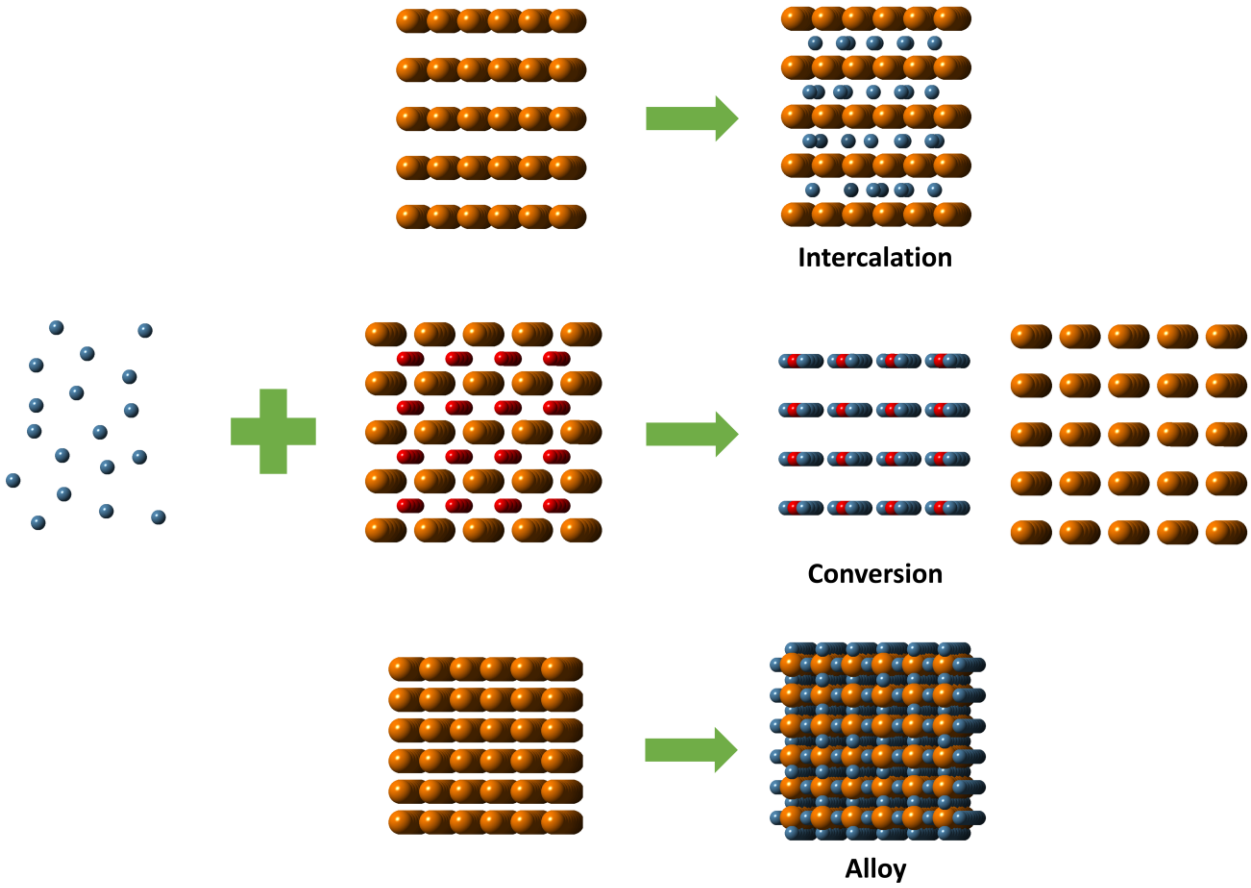

Figure 2.2 Schematic of reaction mechanism for 3 different types of anode materials.

Figure 2.2 depicts the reaction mechanism for each type of anode materials. For intercalation anodes, a well-defined crystal framework is required. But for alloy and conversion anodes, crystallization is not necessary. The reaction formulas for each reaction mechanism can be describes as following:

1) Interaction: $M_iO + Li^+ + e^- \leftrightarrow LiM_iO$ (for carbon: $C_i + Li^+ + e^- \leftrightarrow LiC_i$)
2) Alloy: $aLi^+ + ae^- + M \leftrightarrow Li_aM$
3) Conversion: $MO_c + 2cLi^+ + 2ce^- \leftrightarrow M + cLi_2O$

Among these anode materials, group IV intermetallics possess the high end of capacity (as shown in Figure 2.1). Si, as one member in group IV, has both the highest gravimetric capacity (4200 mAh/g) and volumetric capacity (9786 mAh/cm^3) when lithiated to $Li_{22}Si_5$[28-30]. However, the large volume variation (up to 400% for Si) during Li insertion and extraction greatly affects its performance in battery cells[31]. The volume variation induces large internal stress and strain which can cause a severe material collapse and electrical isolation, resulting in a low coulombic efficiency and rapid capacity fading[32]. Moreover, repeated volume expansion and contraction yields an unstable SEI between the re-exposed Si surface and electrolyte during cycling, which leads to an increase in the internal impedance and a deleterious effect on the electrochemical reactivity due to the accumulation of insulated SEI products[33].

In order to make better use of this high capacity anode material, much effort has been made to alleviate the huge volume variation and its influence. Reducing the size of the active particles to the nanometric range is the most popular method to address this problem. This method effectively shortens the Li-ions and electrons diffusion path in active materials, which accelerates charge and discharge rate. Moreover, the surface area of active materials is largely increased, making electrochemical reactions easier and quicker[34]. However, size reduction of active material is not sufficient to ensure high capacity and high-power density. Researchers have introduced other

complementary components to form composites and further optimized the performance of alloy anode materials. In such a composite material, one component functions as a stress absorber whereas the other provides the boost in capacity[23].

In our research[35], we followed the trend to reduce alloy anode material into nano-sized thin films and adopted metals (Cr, Ti, etc.) as complimentary components. However, instead of simply mixing components, we use a synthetic way to combine them, the multi-layer architecture. As schematically shown in Figure 2.3, the conducting metals and active anode materials are

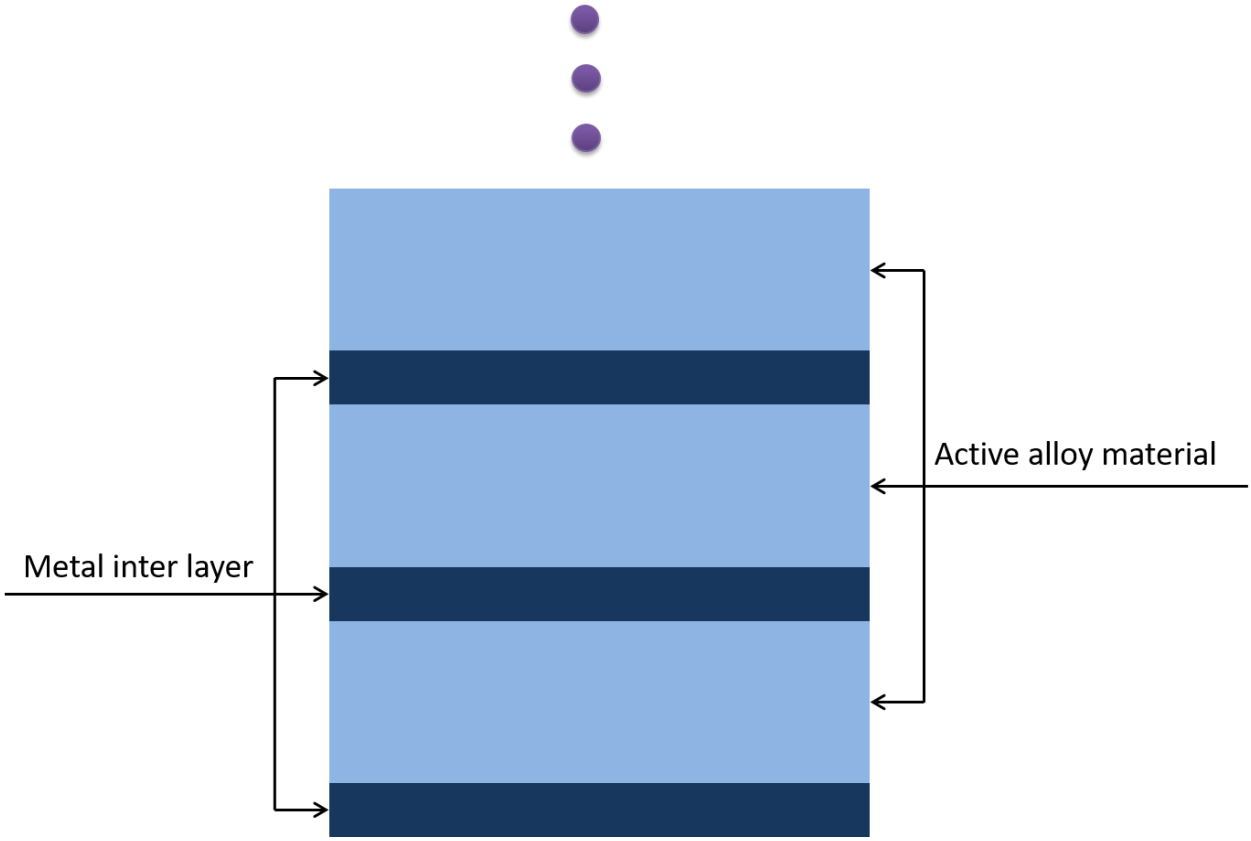

Figure 2.3 Schematic of multi-layer system

alternatively stacked on each other to from a multi-layer structure. In this way, the high energy density of alloy materials is combined with the structural reversibility, the advantage of intercalation materials. Moreover, the high conductivity of metal inter layers largely increases the electrochemical performance of the whole system.

We investigated both Si-based and Ge-based multi-layer systems with Cr and Ti as interlayers respectively. Though Si is favored over other group IV elements, due to its highest capacity, low cost and abundance, Ge is also attractive due to its intrinsically high electronic conductivity at room temperature (2.1 S/m), which is 3 orders of magnitude higher than that of Si (1.6×10^{-3} S/m).[36] Also Li diffusivity in Ge (6.25×10^{-12} cm^2/s) is 2 orders of magnitude higher than Si (1.9×10^{-14} cm^2/s).[37] These electronic and ionic transport properties make Ge electrodes more suitable for high power anodes. Ge also benefits from its minimal surface native oxide, in contrast to silicon[38], that reacts with Li during the initial charging to form Li_2O. This native oxide can lead to a large irreversible capacity loss during the first cycle for nanostructured anodes that have intrinsically large surface areas.

2.2 $LiMn_2O_4$ cathode material

Since 1980 when $LiCoO_2$ was firstly demonstrated as a good cathode for Li-ion battery, the intercalation concept became the general principle for exploring new cathode materials. An intercalation cathode is a solid host network, which can store guest ions. The guest ions can be inserted into and be removed from the host network reversibly. In a Li-ion battery, Li^+ is the guest ion and the host network compounds are metal chalcogenides, transition metal oxides, and polyanion compounds[39]. Prof. Whittingham listed several key requirements for cathode material in his review paper[40].

(1) The material should contain a readily reducible/oxidizable ion to form redox couple with Li (e.g. transition metal).

(2) The material reacts with lithium in a reversible manner. The host structure cannot change dramatically as lithium is added or removed.

(3) The material reacts with lithium with a high free energy of reaction. This can guarantee relatively high energy density and capacity.

(4) The material reacts with lithium very rapidly both during insertion and removal. High power density requires reaction occurring fast. For electric vehicles, both charging and discharging rates should be taken into consideration.

(5) The material should be stable upon overdischarge and overcharge (i.e. for safety).

(6) The materials should be low cost and environmentally benign.

Under intercalation principle and these six key requirements above, researchers have investigated hundreds of cathode candidates. Figure 2.4 has listed some of widely studied cathode materials with their capacity and working potential. Among them, $LiFePO_4$ (LFP), $LiCoO_2$ (LCO)

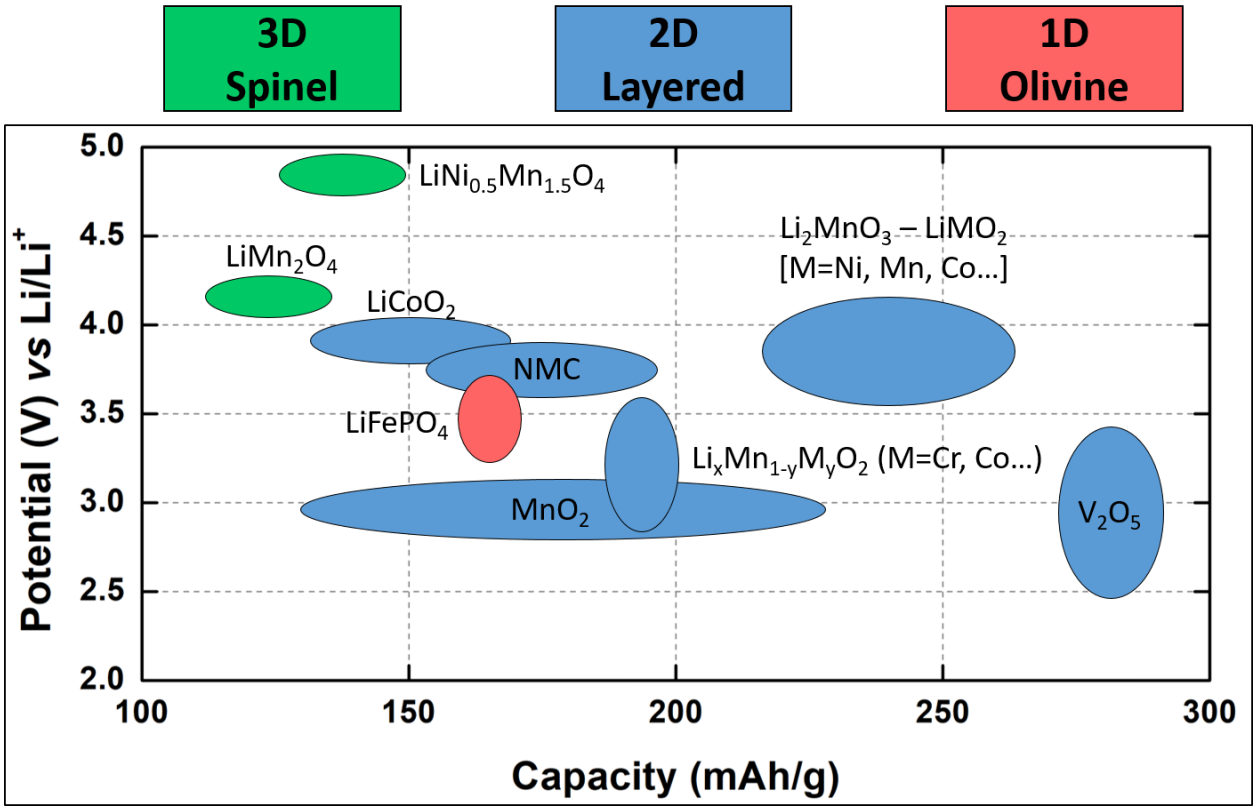

Figure 2.4 Range of average electrochemical potential and capacity of cathode materials

and $LiMn_2O_4$ (LMO) are the three most typical ones. These three cathode materials also represent three categories, namely 1D, 2D and 3D intercalation cathodes.

Figure 2.5 shows the crystal structures for these three typical cathode materials. The olivine structure of LFP has a hexagonally-close-packed oxygen array in which there are corner-shared FeO_6 octahedra (brown) and PO_4 tetrahedra (light purple). The layered structure of LCO has a face-centered cubic oxygen array providing a two-dimensional network of edge-shared CoO_6 octahedra (blue) for the

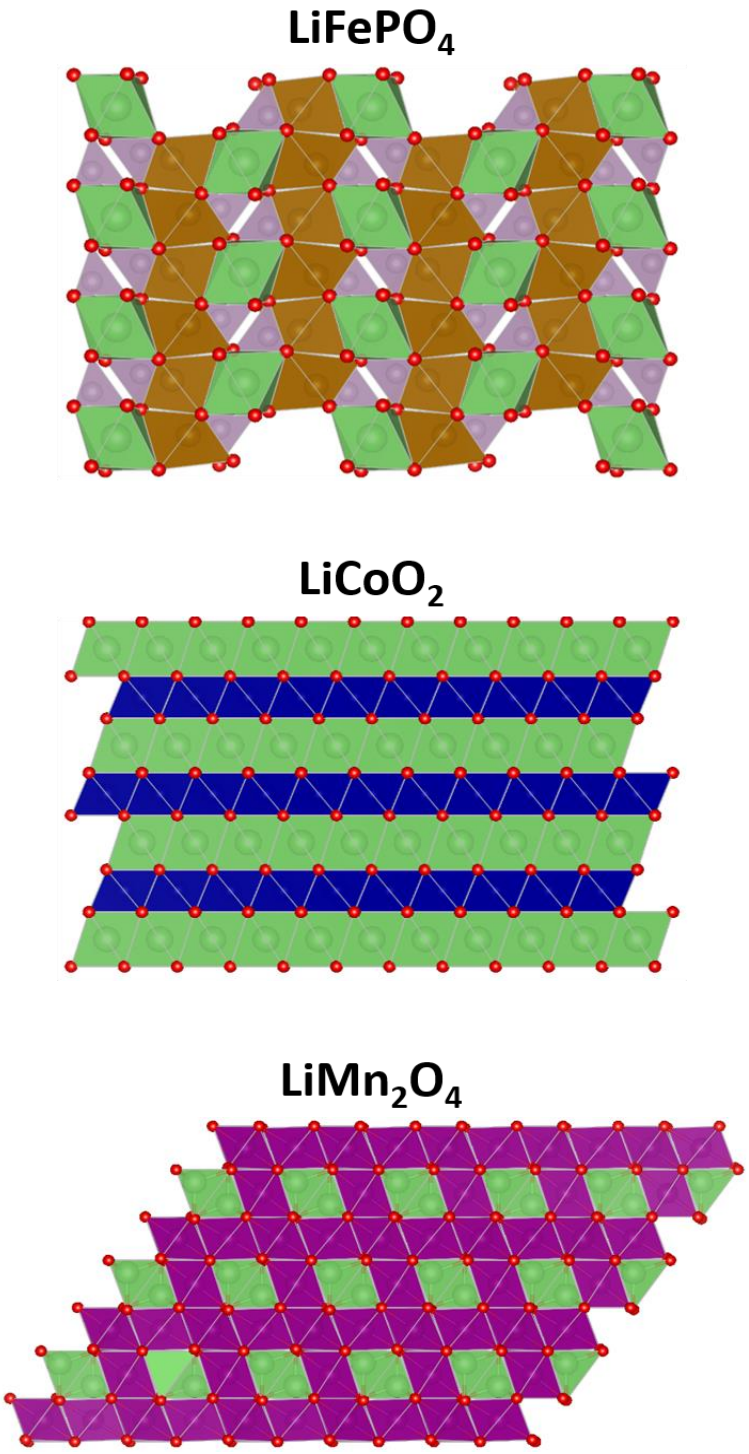

Figure 2.5 Crystal structure of $LiFePO_4$, $LiCoO_2$, $LiMn_2O_4$. Li is represented in green.

lithium ions. The spinel structure of LMO also has a face-centered cubic oxygen array, providing a three-dimensional array of edge-shared MnO_6 octahedra (purple) for the lithium ions.

So far, there is no single cathode material with all advantages overwhelming others. Table 2.1 lists the advantages and disadvantages for these three typical cathode materials. Our research mainly focuses on LMO as a cathode material, to carry forward its benefits as well as to explore the solutions for its problems.

As mentioned above, the main problem for LMO cathode is capacity fading, which will largely limit the life-time of batteries. At elevated temperature, this phenomenon becomes even more severe [41] (Figure 2.6). Two reasons have been considered as the main sources for this capacity fading. One of them is the disproportional degeneration of Mn^{3+} as

Material	Advantage	Disadvantage
$LiFePO_4$	Inexpensive and environmentally benign of Fe; Excellent safety due to covalently bonded PO_4 groups.	Low electronic and Li^+ ion conductivity; High processing cost.
$LiCoO_2$	High electronic and Li+ ion conductivity; Good cycle life and reliability.	Expensive and toxic of Co; Only 50% of the theoretical capacity can be utilized.
$LiMn_2O_4$	Inexpensive and environmentally benign of Mn; Excellent rate capability.	Severe capacity fading, especially at elevated temperature.

Table 2.1 Advantages and disadvantages of three typical cathode materials for Li-ion battery.

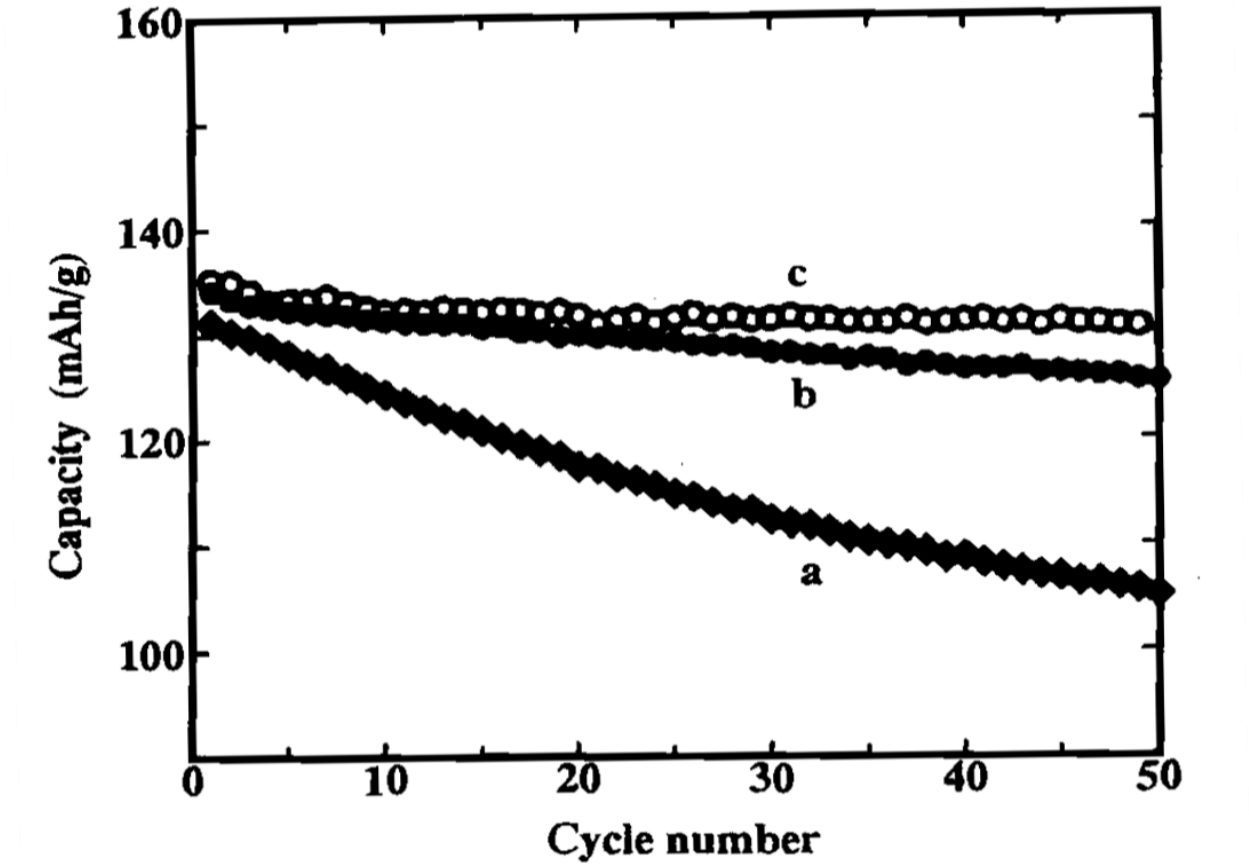

Figure 2.6 Cycling behavior of $LiMn_2O_4$ at various operating temperatures: (a) 50℃, (b) 25℃ and (c) 0℃.

$$2Mn^{3+} \rightarrow Mn^{2+} + Mn^{4+}$$

After this reaction, the soluble Mn^{2+} ion will be dissolved into electrolyte [42, 43]. Both cathode material loss and Mn^{2+} precipitation on anode [44] will dramatically influence the whole battery performance. The other reason is so called Jahn-Teller effect, which is the geometric distortion of nonlinear complexes of certain transition metal ion to remove degeneracy. Mn(III) in octahedral coordination is expected to have an electronic configuration of $t_{2g}^3 e_g^1$. Elongation along one axis of the octahedron decreases the symmetry and removes the degeneracy. This geometric distortion

leads to stress within the cathode and phase change [43, 45].

Although the two reasons stated above are bulk phenomena, their impacts are most seen at the surface of active materials. Standard electrochemical and *ex situ* surface methods have clearly revealed the correlation between manganese surface reactions and battery performance. Based on that, the studies of doping and coating[45-63] are also proved to be useful. However, those studies mostly focus on bulk LMO (polycrystal). Further study is needed to investigate the reactions at a specific surface. Hence, in order to acquire the essential idea about how these reactions occur and their difference on different surfaces, we keep studying the structure changes at the electrode / electrolyte interface of epitaxial thin film electrodes with well-defined orientations using *in situ* X-ray surface sensitive methods (e.g. crystal truncation rod) and *in situ* AFM assisted by other supplementary techniques such as XPS, TEM *etc*.

2.3 $MgMn_2O_4$ multivalent cathode material

Although the study of Li-ion battery developed rapidly in the past decades, the long-term concerns of high cost, limited reserves of lithium and safety are still big issues that need to be faced. Moreover, advancements at the materials level are approaching a fundamental limit in Li-ion batteries. In order to achieve even higher energy densities, pioneers have turned their attention to “beyond Li-ion” materials. The goal for “beyond Li-ion” technology is seeking alternative

energy storage solutions such as other alkaline, alkaline earth and transition metal based rechargeable batteries[64, 65]. As a promising successor of Li-ion battery, “beyond Li-ion” technology should not only significantly improve energy density and reduce cost but also be compatible with existing, highly optimized Li-ion battery architecture and fabrication to take advantage of the knowledge accumulated over the past decades. Following these criteria, the Mg multivalent (MV) battery with intercalation cathode becomes one of the most attractive topic.

There were some initial efforts in the early 1990s by Gregory *et al.*[66] and Novak *et al.*[67-69]on non-aqueous MV Mn-ion batteries. Then in 1998, Le *et al.*[70] investigated the intercalation of Mn^{2+} into V_2O_5 aerogels for the first time. Two years after, Aurbach *et al.*[71] further illustrated the feasibility of MV intercalation based Mg-ion battery technology using ether electrolytes. Comparing with Li and Na, Mg metal anode has the advantages of less reactiveness in the ambient atmosphere and absence of dendritic growth issues during electrochemical cycling. Therefore, the main focus of research on Mg-ion batteries is on the cathode and electrolyte. As a consequence of transferring two electrons per ion, Mg based cathodes can potentially achieve nearly twice the capacities compared to Li based cathodes when occupying a similar number of intercalant sites. While the literature reports a few works on MV cathode materials, the intercalation host space is relatively unexplored compared to Li-ion.

In our research[72], we present a novel approach to explore and understand factors that control reversible electrochemical activity of a Mg based cathode using model epitaxial thin film cathodes. Specifically, the use of epitaxial stabilization allows the comparison of electrochemical activity for structurally distinct materials that are compositionally identical. We demonstrate this approach by studying Mg^{2+} insertion and extraction from spinel oxides, AB_2O_4, which are attractive cathode materials because they have low cost, low toxicity, and good safety characteristics[63]. This choice is based on the success of Li-based spinel cathodes, such as $LiMn_2O_4$ (LMO) and $LiNi_xMn_{2-x}O_4$[73]. Mg spinels, e.g., $MgMn_2O_4$ (MMO), might be expected to reversibly incorporate Mg^{2+}, since it has a diameter that is similar to Li+ (~86 pm and ~90 pm, respectively)[74] and MMO has a theoretical gravimetric capacity of ~270 mAh/g[75]. Unlike LMO, MMO adopts a tetragonal spinel structure with space group $D^{19}{}_{4h} - I4_1/amd$ with a = b = 5.727 Å and c = 9.284 Å[76]. This structure is a partially inverted spinel with a majority of Mn(III) in the octahedral site as well as a fraction of Mn(IV) and Mn(II) in the octahedral and tetrahedral sites, respectively[77] (indicated as $(A_{1-\lambda}B_\lambda)[A_{\lambda/2}B_{1-\lambda/2}]_2O_4$ where λ is the inversion degree and the parentheses and brackets denote the tetrahedral and octahedral sites, respectively). Theoretical investigations of this tetragonal spinel[75] as a possible insertion host for MV ions suggest that its primary limitation as a MV cathode is due to its intrinsically sluggish diffusion of Mg^{2+}, moving between the tetrahedral and

octahedral sites (with barriers of ~600−800 meV), which is a common limitation for MV cathodes. A recent experimental study shows that the delithiated cubic phase λ-Mn_2O_4 can be inserted by Mg^{2+} in both aqueous and non-aqueous electrolytes. However, this insertion drives a phase transformation from cubic Mn_2O_4 to tetragonal $MgMn_2O_4$[78]. In comparison, the stable operation of $Li_xMn_2O_4$ as a cathode in LIBs makes use only of the cubic phase (i.e., $x < 1$), as complications, such as capacity fade, become apparent for $x > 1$ where LMO transitions to the tetragonal phase[79]. These comparisons suggest that one possible route to improving the electrochemical properties of MMO as a MV cathode is the stabilization of the cubic $MgMn_2O_4$ (or Mn_2O_4) host lattice.

To test this idea, we compare the electrochemical activity of Mg^{2+} in two epitaxially stabilized polymorphs of MMO thin films: the tetragonal vs cubic spinel structures of MMO. While the former is the stable phase under ambient conditions, the latter is found as the stable bulk phase only at high temperature (>950 °C)[76, 80] or high pressure (>15.6 GPa)[81]. Phase-pure epitaxially stabilized MMO thin films are synthesized on conducting buffer layers so that the intrinsic relationships between cathode crystal structure and its electrochemical activity can be explored.

Chapter 3 : Experimental Methods and Instrumentation

3.1 Physical vapor deposition

Physical vapor deposition (PVD) processes (often just called thin film processes) are atomistic deposition processes in which material is vaporized from a solid or liquid source in the form of atoms or molecules and transported in the form of a vapor through a vacuum or low pressure gaseous (or plasma) environment to the substrate, where it condenses.[82]

3.1.1 Thermal evaporation deposition

Thermal evaporation is one of the most widely used PVD techniques. It is a type of thin film deposition, which is a vacuum process wherein coatings of pure materials are applied over the surface of many different objects. The deposited coatings or films usually have a thickness in the range of angstroms to microns and are composed of a single material or layers of multiple materials. Thermal evaporation mainly involves two basic processes, which are hot source material evaporating and condensing on the substrates (Figure 3.1). The evaporant is heated to the melting point in the filament boat, which will generate a certain vapor pressure. Inside the vacuum, even a very low vapor pressure is

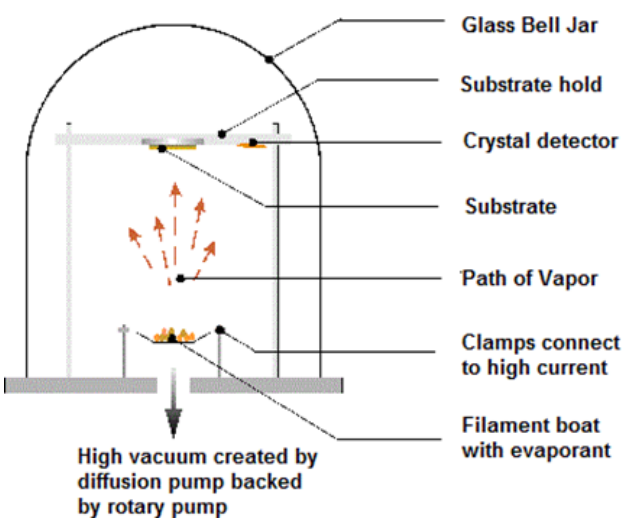

Figure 3.1 Schematic of thermal evaporation

adequate to create a vapor cloud within the chamber. The vapor then rises above from this bottom source and reaches the substrates that are held inverted in suitable fixtures at the top of the chamber, with surfaces to be coated facing down toward the rising vapor to acquire their coating.

3.1.2 Sputtering deposition

Sputtering deposition (Figure 3.2) is also a PVD technique which includes several subcategories such as DC/RF, magnetron and Ion-assisted. Instead of particle vapor created by heating, the particle stream is the ejection of atoms by the bombardment of a solid or liquid target by energetic particles, mostly ions. It results from collisions between the incident energetic

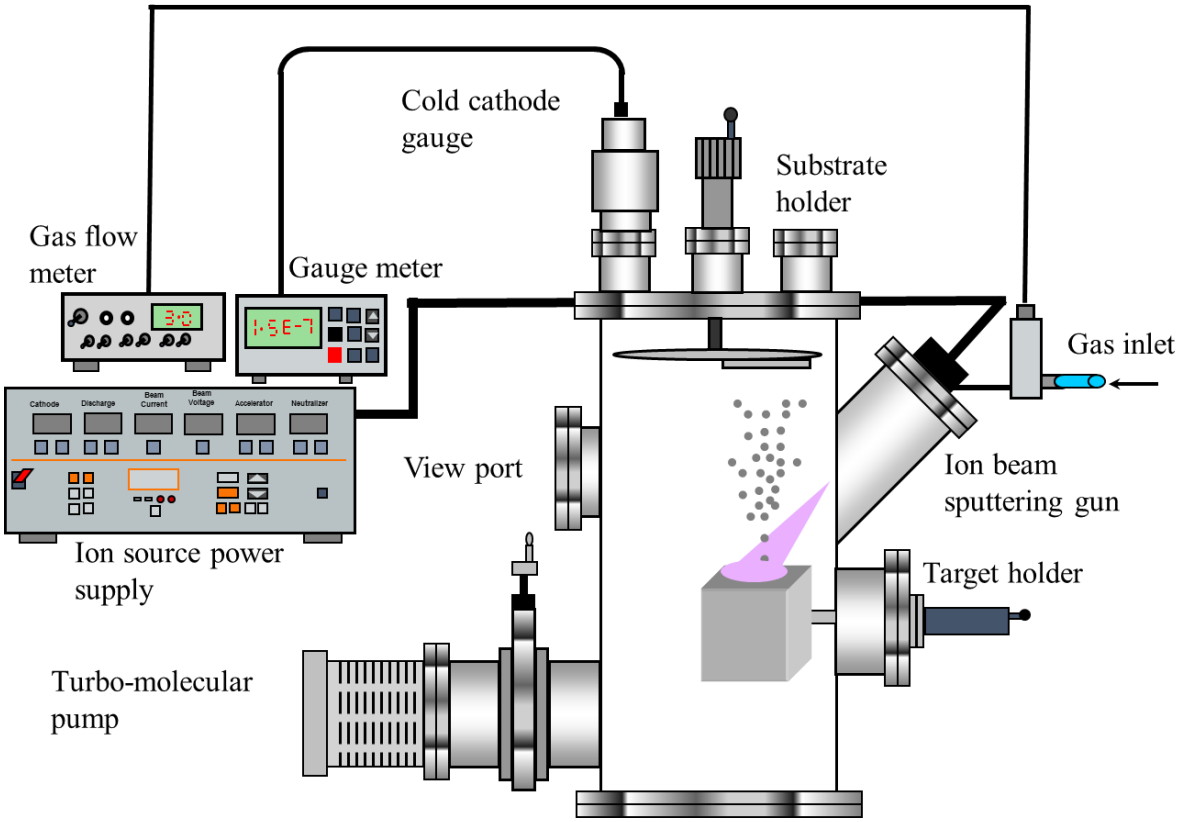

Figure 3.2 Schematic of universal sputtering deposition system

particles, and/or resultant recoil atoms, with surface atoms. When an energetic particle strikes a surface (the target), a plume of material is released, like the shower of sand when a golf ball lands in the bunker.

Normally, there are four steps for the sputtering deposition process (DC model as example). First step is the energetic particles generating. Argon is generally used as sputtering gas. If a high negative potential difference (~1000V) is applied between the target and the substrate in a rarefied Argon environment, electrons released from the target (cathode) collide with Ar atoms and ionize them, giving them a positive charge. Then, also in this high electric field, Ar^+ ions will be accelerated towards target and energetic particles. Second step is energetic particles (Ar^+) bombarding target and releasing target material. After that, the sputtering material (released from target) is transported to the substrate. On the substrate surface, the atom stream will condense and finally become a thin film coating on the substrate.

3.1.3 Pulsed laser deposition (PLD)

Pulsed laser deposition is another member of physical vapor deposition process that shares some process characteristics common with molecular beam epitaxy and some with sputtering deposition. In PLD, shown schematically in Figure 3.3, a pulsed laser is focused onto a target of the material to be deposited. For sufficiently high laser energy density, each laser pulse vaporizes

or ablates a small amount of the material creating a plasma plume. The ablated material is ejected from the target in a highly forward-directed plume. The ablation plume provides the material flux for film growth[83]. This process is a conceptually and experimentally simple yet highly versatile tool for thin-film and multilayer research. It has several superior characteristics which include congruent (stoichiometric) transfer of material, capability for reactive deposition in ambient gases, growth of multilayered epitaxial hetero-structures, uniform thickness of films and more[84]. Those

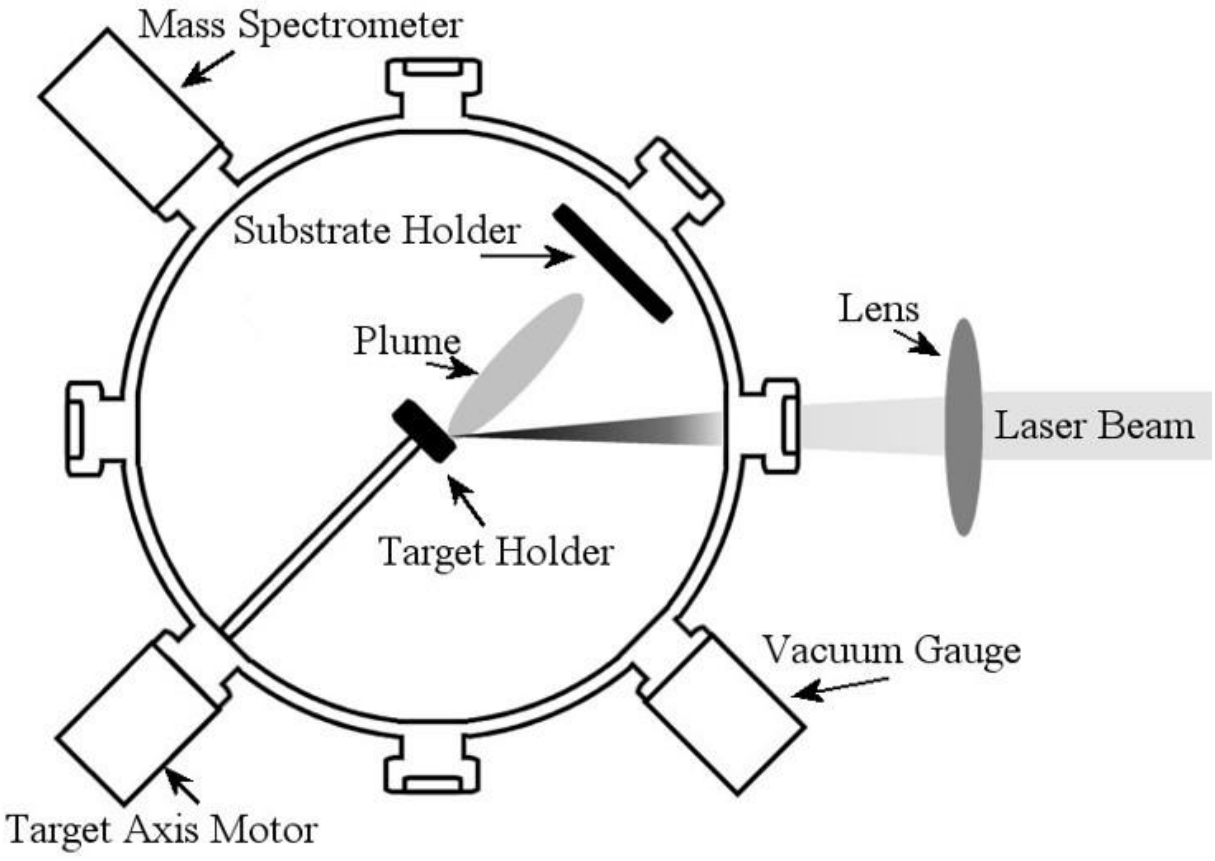

Figure 3.3 Schematic of Pulsed Laser Deposition system

merits distinguish it from other film-growth methods and provide special advantages for the growth of oxides and other chemically complex (multielement) materials.

3.2 Atomic force microscopy (AFM)

The atomic force microscope is a combination of the principles of the scanning tunneling microscope and the stylus profilometer[85] which measures the surface morphology in three-dimensional detail down to the nanometer scale. AFM can image all materials, hard or soft, synthetic or natural, irrespective of opaqueness or conductivity[86]. The images are not obtained in the usual way (i.e. by line-of sight, reflections or shadows). Instead, at each point or pixel within a 2D array over the surface, a measurement of surface height is made using a sharp solid force probe which essentially uses touch to image a surface. Then, the measured 2D array with height information at each point can be displayed with a gradient of color or even rebuilt into a 3D perspective. The typical range of these measurements is several micrometers vertically with sub-nanometer height resolution and several micrometers laterally with hundreds of pixels resolution.

However, the height variance can be as small as sub-nanometers. Therefore, an indirect method is introduced to keep track of vertical displacement of probes. In a common design of AFM (Figure 3.4a), the sharp tips (probes) are attached to a flexible microcantilever which bends under the influence of force. The bending is usually measured by reflecting a laser beam off the

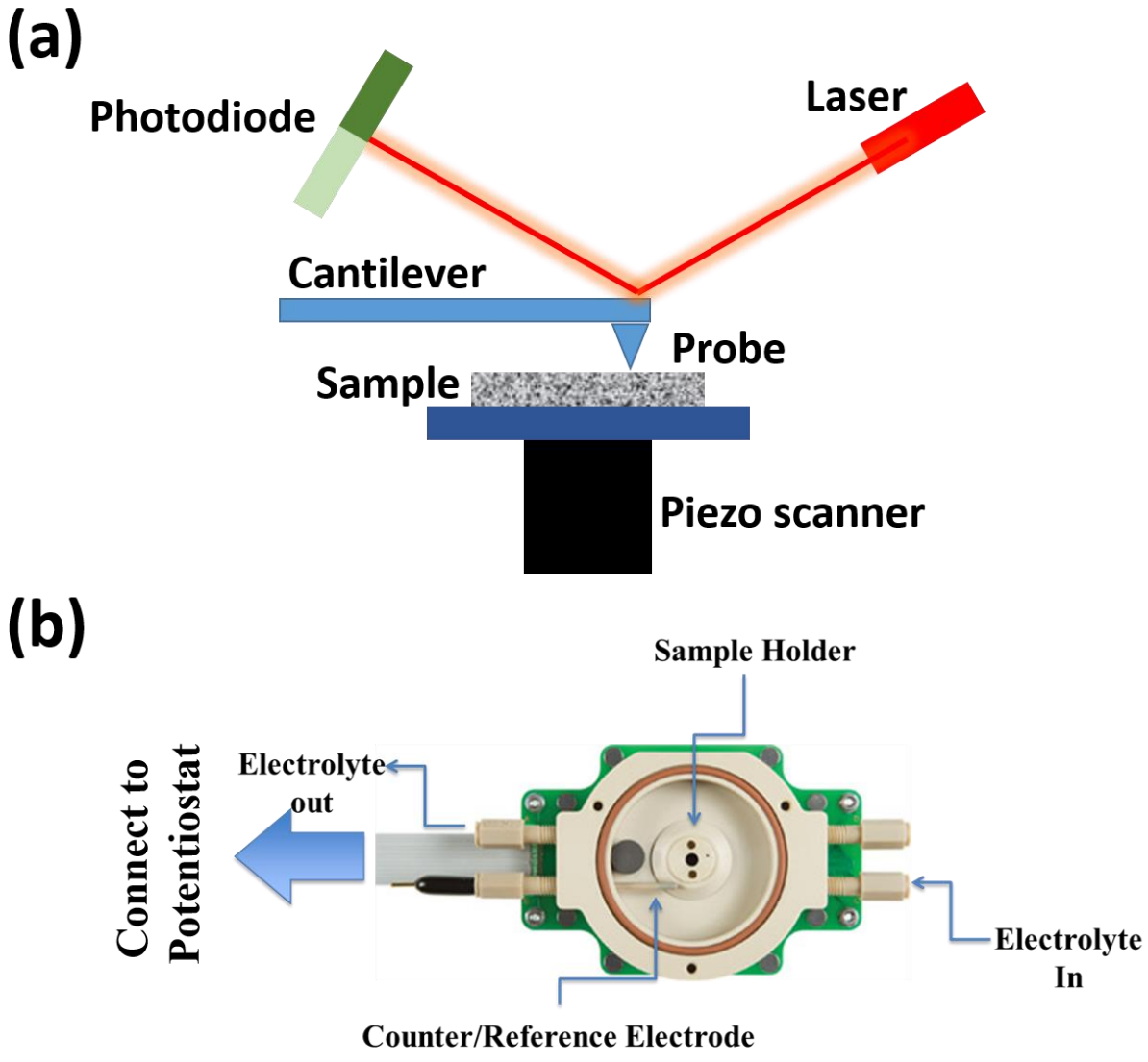

Figure 3.4 (a) Schematic of Atomic Force Microscopy system. (b) Customized electrochemistry sample holder for *in situ* AFM measurements.

cantilever and onto a split photodiode (a horizontal “knife edge”), the output of which gauges the position of laser spot. The vertical tip movement, in turn, is quantified from this cantilever bending. Lateral forces that torque the tip which causes the cantilever to twist can be measured via the horizontal movement of the laser spot. This measurement typically will handle a vertical tip range of hundreds of nanometers with sub-nanometer resolution which essentially decides the vertical resolution of AFM.

In order to perform *in situ* AFM measurements on battery electrode materials. We have customized an EC cell (Figure 3.4b) which can create an airtight space to hold the sample and electrolyte. Through the connection embedded on the circuit board, current and voltage can be applied onto the samples with in situ AFM measurements in the meanwhile.

3.3 Synchrotron X-ray source, optics, diffractometers and detectors

When electrons or other charged particles moving at relativistic speeds are forced by magnetic fields to follow curved trajectories they emit electromagnetic radiation in the direction of their motion which is called synchrotron radiation. The theoretical basis for synchrotron radiation was illustrated by Joseph Larmor[87] in 1897, the same year of Thomson’s discovery of the electron. Joseph derived and expression from classical electrodynamics for the instantaneous total power

radiated by an accelerated charged particle and then the Alfred Lienard showed the radiated power emitted by electrons moving on a circular path to be proportional to $(\varepsilon/(mc^2)^4/R^2$, where ε is the electron's kinetic energy, m is the electron rest mass and R is the radius of the trajectory[88]. Initially, synchrotron radiation was treated as an unwanted but unavoidable loss of energy in high energy physics accelerators until Diran Tomboulian and Paul Hartman from Cornell University demonstrated the potential advantages of synchrotron radiation[89]. Therefore, the first-generation synchrotron radiation facilities were built in a parasitic way which were not dedicated to synchrotron radiation studies but to high energy physics experiments. Normally, the synchrotron radiation is produce by high energy electron centripetal accelerators such as storage rings (Figure 3.5 left). They consist of circular evacuated pipes where the electrons are forced to follow circular

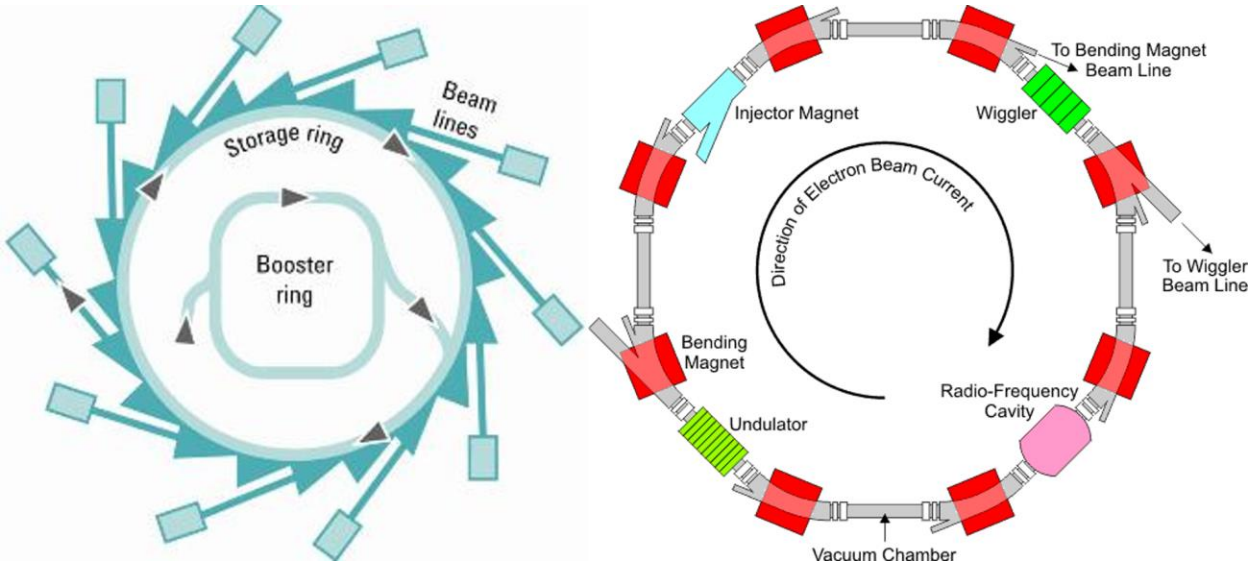

Figure 3.5 Schematic planar view of a synchrotron radiation facility (left) and a storage ring which includes RF cavity and three types of magnetic elements (right).

paths under the action of magnets placed along the circumference (bending magnets). The electrons enter the storage ring only after they have been accelerated by a linear accelerator until their energy reaches several millions of electron volts (MeV) and then by a booster ring that gives them a boost in energy from millions to billions or Giga electron volts (GeV); at that point they are transferred to the final circular accelerator (storage ring). Besides the bending magnets, storage ring also consists of many insertion devices (Figure 3.5 right). The Radio-Frequency cavities are used to replenish the energy of electrons which was lost due to the generation of synchrotron radiation. While the wigglers and undulators acts as an upgrade to bending magnets for focusing and bending the beam.

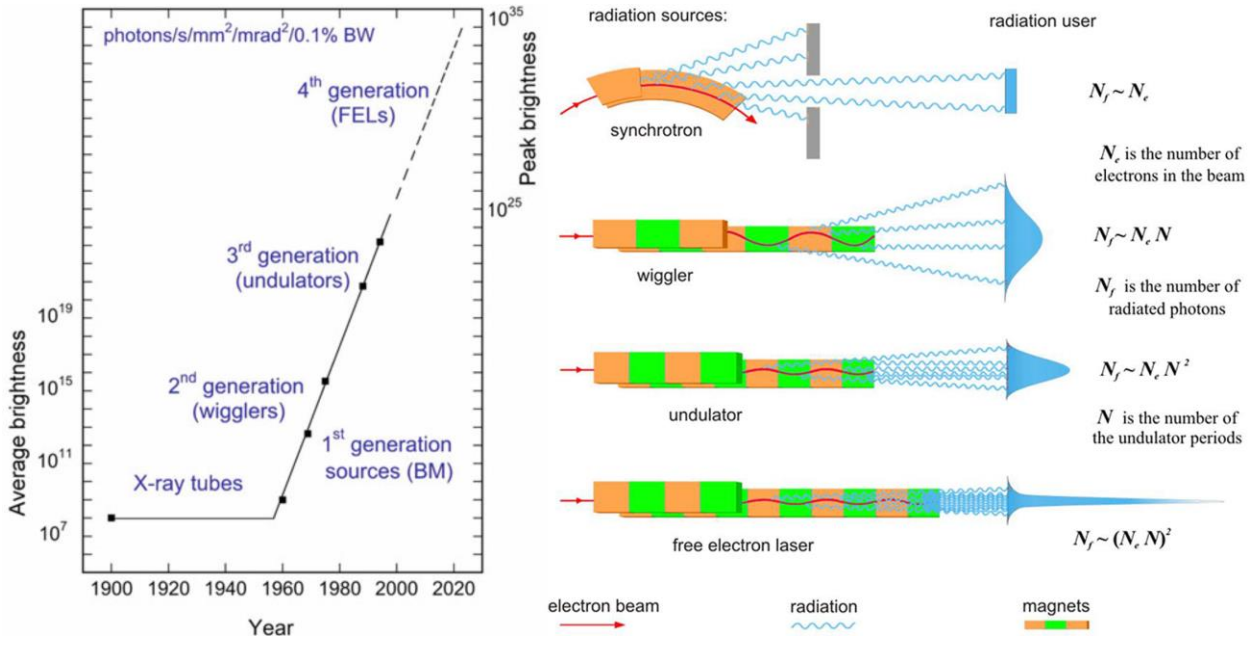

Figure 3.6 Comparison between the average brightness of storage rings of different generations (left); Comparison between the synchrotron radiation from three different types of magnetic elements as well as the free electron laser (right).

The three types of magnetic elements in the storage ring classifies the three generation of synchrotron radiation source (Figure 3.6 left)[90]. Figure 3.6 right depicts the characteristics of the radiation from these three magnetic elements[91, 92]. The bending magnet effectively generates a sweeping searchlight pattern. Due to the relativistic velocity of the electrons, the radiation pulsed are highly collimated with a vertical opening angle of $1/\gamma$, where $\gamma = E_0/m_e c^2$, near the synchrotron emission critical energy[93]. A wiggler is a series of magnets designed to periodically laterally deflect the electron beam. These deflections create a change in acceleration which in turn produces emission of broad synchrotron radiation tangent to the curve, much like that of a bending magnet, but the intensity is N times higher, where N is the number of magnetic dipoles in the wiggler[94]. Furthermore, due to the decrease of wavelength, the wiggler creates a wavelength of light with higher energy. An undulator consists of a periodic structure of dipole magnets[95]. Electrons traversing the periodic magnet structure are forced to undergo oscillations with small amplitude and the radiation displays interference patterns which leads to narrow energy bands and very intense radiation. For an undulator with N periods, the intensity can be up to N^2 times higher than bending magnet.

Comparing with the traditionally radiation source, such as rotating anode, synchrotron radiation is more favored with several overwhelming advantages. First of all, the high intensity as

well as brightness, which can be up to 10 orders of magnitude higher than X-ray tube; Second, the very broad and continuous spectral range from infrared to hard X-ray region, which can afford the requirements for different uses; Third, the high degree of polarization which makes coherent diffraction possible; Last but not least, the ultra-high vacuum environment and high bean stability[96].

Usually, there will be several beamlines around one storage ring. An individual synchrotron beamline can be divided into two main parts, the optical section and the experimental station[97]. A typical optical scheme for a beamline working in the hard X-ray range is shown in Figure 3.7. Also, the three most important optics are listed below the beamline scheme which are slits (including filters and shutters), monochromator and X-ray mirrors[98-102].

Slits, as well as filters and shutters, are used to control the beam flux and size[103]. The slits are usually movable beam stops with precise motors to control their positions. They are used to

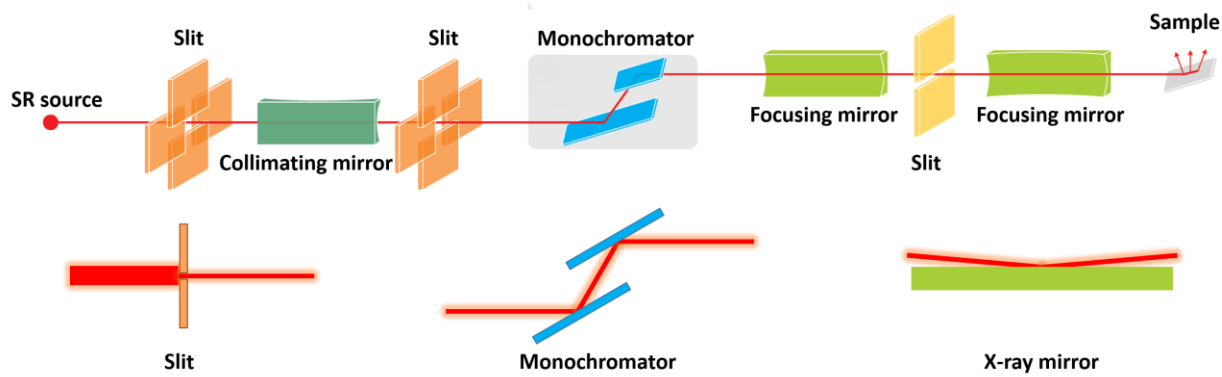

Figure 3.7 Schematic overview of the optics of typical beamline operating in the hard X-ray range (top) and the list of 3 most important parts: slit, monochromator and X-ray mirror (bottom).

define the beam either horizontally or vertically and can be used in pairs to define the beam in both directions as well. Beam filters (or attenuators) attenuate the beam flux by passing the incident synchrotron radiation through a thin transmissive foil. A typical filter has two or three racks, with each rack holding three or four separate foils with different thicknesses which stand for different attenuation factors. The racks are motorized to move perpendicular to the beam to select between particular foils. A beam shutter is a total beam stop which is used to interrupt radiation from the front end or optics enclosure when it is not required downstream.

The role of the monochromators is to deliver an X-ray beam with a high monochromaticity with an energy resolution $\Delta E/E \leq 10^{-4}$ for the most common applications and high intensity of reflections. In X-ray monochromators, diffraction from perfect crystals is used to monochromatized the beam. The condition for X-ray diffraction is expressed by Bragg's law:

$$2dsin\theta = n\lambda \qquad \text{Eq. 3.1}$$

where d is the spacing of crystal lattice planes, λ is the wavelength and θ is the incident angle. In order to achieve the required monochromacy, multiple Bragg reflections are usually used to monochromatize one beam. The typical double crystal monochromator with two parallel crystals produces a monochromatic bean running parallel to incident white X-ray beam. Moreover, the crystals of the monochromator can also be used to provide sagittal focusing[104] by bending them

into a proper radian.

The X-ray mirrors are used both as high-energy cut-off filters and as focusing devices. When used as high-energy cut-off, specular reflection mush be taken into account. This is related to the index of refraction *n* in the X-ray regime[105]:

$$n = (1 - \delta) - i\beta \qquad \text{Eq. 3.2}$$

where the quantities δ and β are related to dispersive and absorptive nature of the materials. δ is related to reflecting material and incident beam energy. As the index of refraction is less than unity, X-rays incident on a material are totally reflected if the incident angle θ is less than the critical angle θ_c. Otherwise, they are absorbed by the material. The critical angle is derived from Snell's law:

$$\theta_c = \sqrt{2\delta} \qquad \text{Eq. 3.3}$$

The mirror reflectivity R as a function of angle (or energy) is a step-like function which immediately drops towards 0 beyond critical angle (or energy). Therefore, at a specific glancing angle, the beam flux with energy higher than critical energy are absorbed instead of reflected. The other application of X-ray mirrors is to collimate and focus the beam onto the following optics or the sample. Similar to the monochromator, the surface of X-ray mirror can be bent to change the bean divergence.

After the adjustment through X-ray optics, the beam reaches experimental station. In general, there are 2 core instruments in this part, diffractometer and X-ray detector. Diffractometer is designed to control the angle between the incident beam and a specific direction of the sample[106]. Based on the number of rotation axes, the diffractometer can be divided into 3 main categories which are 2-circle (sector 5BM-C, APS), 4-circle (sector 33BM-C, APS) and 6-circle (sector 33ID-D, APS). Figure 3.8 shows the schematic design (left) of the 6-circle diffractometer (most popular type) at sector 33BM-C in APS and the notation of each axis (right). In 4-circle diffractometer, 3 of the 4 axes (ω, χ and φ) control the rotation of sample in 3D geometry. While the last axis, 2θ, control the angle between the incident beam and X-ray detector (outgoing beam). This is called "3S + 1D configuration"[107]. If we define the plane which is identified by incident beam and outgoing beam as reference plane, then the φ and χ rotation have axes in the reference plane and

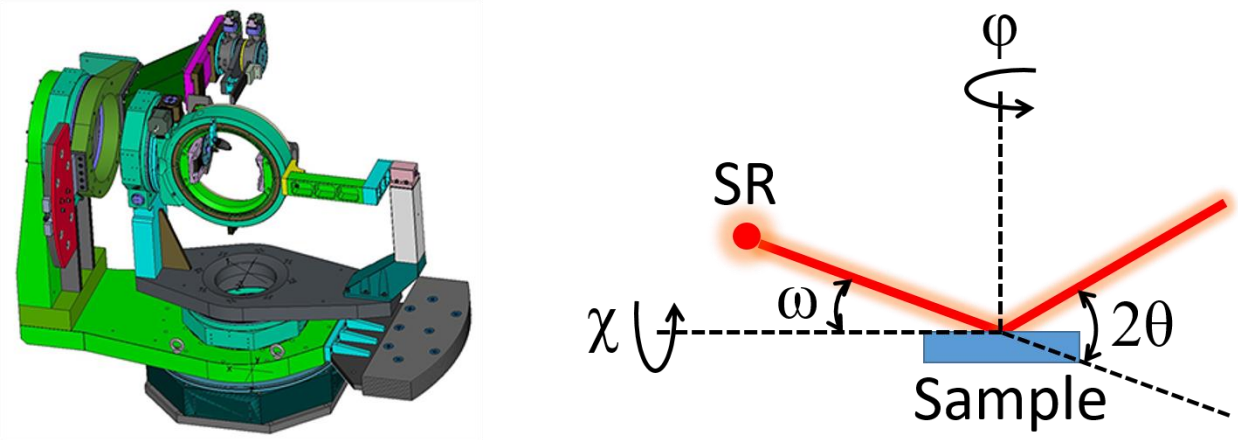

Figure 3.8 Schematic of Huber 6-circle diffractometer (left) and illustration for each axis (right).

perpendicular to each other, while the axis for ω rotation is parallel to the normal of the reference plane and perpendicular to the other 2 rotation axes[108]. The 2θ rotation axis essentially follows the same direction of ω rotation. However, they are 2 different rotation axes since 2θ is used for the control the position of detector while ω is used to adjust samples' orientation. Based on the specific experiment requirement, the 4-circle diffractometer can be simplified to 2-circle or complicated to 6-circle. In 2-circle geometry, there are only ω and 2θ rotation axes (1S + 1D configuration) which is designed for the measurement on isotropic samples such as amorphous, powder or polycrystalline materials[109]. In principle, 3 degrees of freedom can position a sample in crystal in any orientation. However, in some cases, the accessible solid angle for X-rays is often limited, making it impossible for the orienting the sample to a desired direction with respect to resolutions and polarization of the incident X-rays. Therefore, an additional sample rotation axis and an additional detector rotation axis are added to form a "4S + 2D configuration" . The extra degree of freedom are coupled with the original 3 degrees of freedom and can be converted to each other through mathematic calculation[110]. Normally, the sample is mounted on a goniometer head and then put on the diffractometer. The goniometer head can manually change the relative position of the sample to the rotation center of the diffractometer.

Usually, an X-ray detector is the end point for the whole X-ray measurement system. There are various kinds of X-ray detectors which can cover different experimental requirements[111]. By detecting format, X-ray detector can be divided into 3 categories which are point, linear and area. Point detectors have a versatile sensitive area which can be manually defined by a slit or a pinhole mask. Therefore, its spatial resolution can be made arbitrarily fine. Linear detectors have limited usage which is mainly used to record small angle X-ray scattering. Area detectors are most favorable detector format at present due to much larger throughput, Essentially, an area detector is an array of detecting units[112]. Each unit or pixel can record X-ray flux individually just like a point detector. If divided by signal recording type, the X-ray detectors have 2 general types, photon counters and photon integrators. Both have their own advantages and disadvantages. The photon counters can discriminate photon energy which allow them to reject inelastically scattered radiation or XRF and thus improve the signal-to-noise ratio. However it always has a count-rate

Figure 3.9 Photo of PILATUS 100K (left) (487 x 195 = 94 965 pixels with 172 x 172 μm^2 for each pixel) and schematic of hybrid pixel array (right).

limitation and begins to miss photons above that limitation (i.e. dead time)[113]. On the contrary, integrating detectors have no inherent count-rate limitation, but they will record much more noise due to the lack of energy discrimination[114].

The X-ray detector I used most in my research was a PILATUS 100K (Figure 3.9 left). PILATUS is a type of X-ray detector which is developed at Paul Scherrer institute in Switzerland. This detector consists of a two-dimensional hybrid pixel array which operates in single-photon counting mode and therefore enables relatively high counting rate as well as low background noise. In the detector X-rays are converted to an electrical signal by the photoelectric effect on X-ray sensors and then counted directly by a series of cells in an ASIC bonded to the silicon detector, rather than relying on a phosphor. Thus, each pixel has its own amplifier, discriminator (for distinguishing X-rays of the desired energy from noise) and counter circuit. In principle, the sensor can be chosen out of a variety of materials in order to accommodate specific usage and that why it is often called hybrid pixel array (Figure 3.9 right). Moreover, PILATUS is a solid-state detector which is not affected by parallax like a gas counter[115-117].

3.4 X-ray scattering and diffraction

3.4.1 General X-ray scattering principle and experimental geometry

X-ray scattering is a physical phenomenon resulting from the interactions between X-ray and materials. In classic explanation, when X-rays interact with an atom, the electrons in atomic shells start oscillating. This dipolar behavior of electrons will send out a spherical wave with same wavelength (elastic scattering)[118-122]. When a coherent X-ray is scattered my multiple atoms, the scattered waves will interfere with each other and generate interference pattern which can be detected and recorded. The observation of X-ray scattered from a sample as a function of incident and scattered angle, polarization and wavelength (or energy) is called X-ray scattering technique. This technique can be non-destructive and can reveal information about the crystal structure, chemical composition and some physical properties of materials. X-ray diffracting is often considered as a sub-category of X-ray scattering in which the scattering object is crystalline.

Since the scattering pattern comes from the interference of waves scattered by atoms, it's essentially the square of the Fourier transform of the atomic array[123]. The Young's double slit experiment is a simple one-dimensional example. If the atomic array is periodic and highly ordered (e.g. crystal), the incident X-rays will be scattered in very specific directions to produce a scattering pattern with sharp maxima which are called diffraction peaks. All the diffraction peaks together

form the square of the Fourier transform of the electron-density distribution with in the crystal. Therefore, through the analysis of diffraction peaks, we can reveal the electron-density distribution of a material and thus, it's structure and other properties.

X-ray scattering can be measured on a diffractometer as described in section 3.3. Since my research mostly focuses on crystalline thin film, all the illustration will be based on the thin film sample. The general X-ray scattering geometry is described in Figure 3.10. The most important parameter in this geometry is called "momentum transfer" which is often noted as $\vec{Q}$. It's defined as the momentum difference of the scattered wave vector to the incident wave vector.

$$\vec{Q} = \vec{k}_f - \vec{k}_i \qquad \text{Eq. 3.4}$$

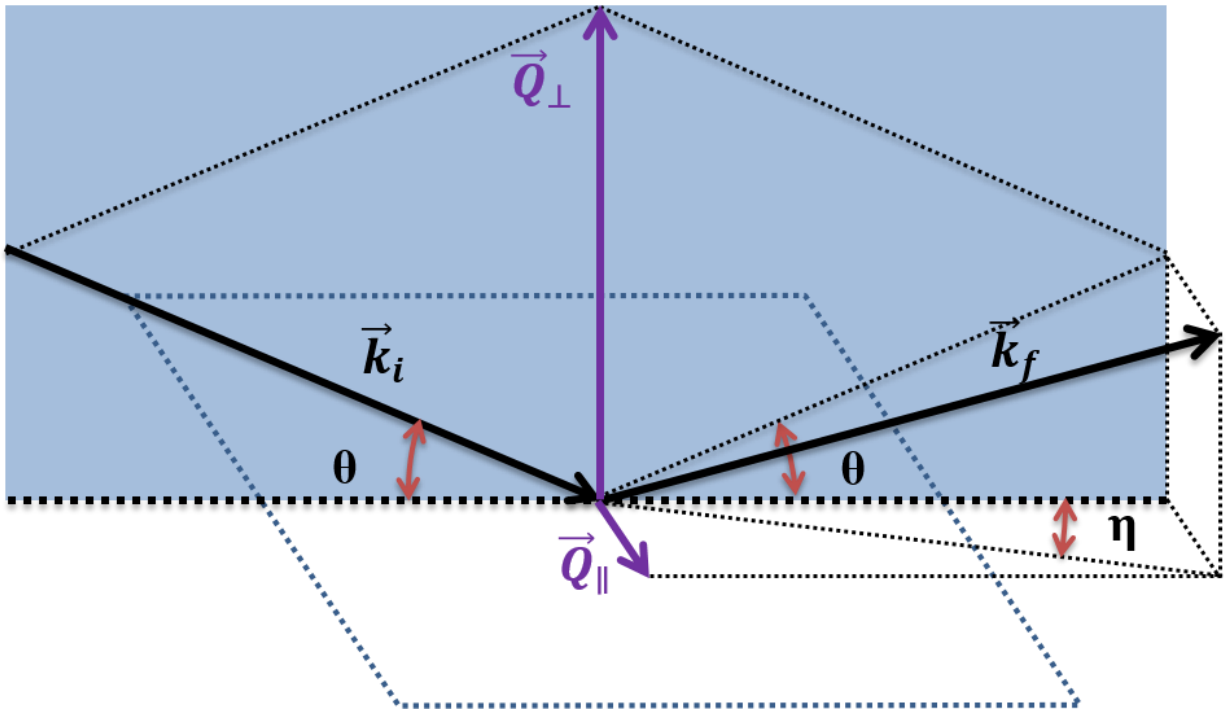

Figure 3.10 Generally X-ray scattering geometry

where $\vec{k}_i$ and $\vec{k}_f$ are the wave vectors of incident beam and scattered beam, respectively. Since X-ray scattering pattern is related to the Fourier transform of the atomic array, it will be convenient for calculation and peak searching in reciprocal space, where the atomic array is already Fourier transformed. The diffraction intensity will reach a maximum when $\vec{Q}$ can exactly connect the origin 000 to a *hkl* point (matches both in direction and distance) in the reciprocal space. Therefore, through the manipulation of $\vec{Q}$ (direction and scale), we can find out all the *hkl* diffraction peaks in principle.

As we mostly deal with thin film sample with a well-defined surface, it will be useful to orthogonally decompose $\vec{Q}$ into $\vec{Q}_{\parallel}$ and $\vec{Q}_{\perp}$. The $\vec{Q}_{\perp}$.is the component of momentum transfer along surface normal, while $\vec{Q}_{\parallel}$ is the component lying in the surface. In most cases, we are only concerned about the structure along surface normal, then $\vec{Q}_{\parallel}$ will be set to zero. Therefore, the total momentum transfer will be along surface normal. This geometry is called Bragg–Brentano geometry[124].

3.4.2 X-ray reflectivity

X-ray reflectivity (XRR) normally refers to the low-angle ($Q < 1$ Å^{-1}) X-ray specular reflection. The basic idea is measuring the X-ray intensity reflected from a flat surface at the specular position of the incident beam. The reflected X-ray intensity is affected by the specimen's

surface information (i.e. roughness, film thickness, electron density etc.)[125-130]. Therefore, this technique is a surface-sensitive analytical technique and mostly used to characterize surface, thin films and multilayers. The analysis of XRR can reveal the electron density profile (can be converted to mass density in most cases) along surface normal of samples. Since this technique probes contrast in the average electron density rather than scattering from individual atoms, it works equally well for amorphous, polycrystalline or even liquid materials as for crystalline materials.

Since both X-ray and visible light are essentially electromagnetic waves, they share most of the common and basic concept. The theoretical basis of XRR technique derive from the Snell's law and Fresnel equations. According to classical optics, a ray of light will change its moving direction and intensity when transmitted through a

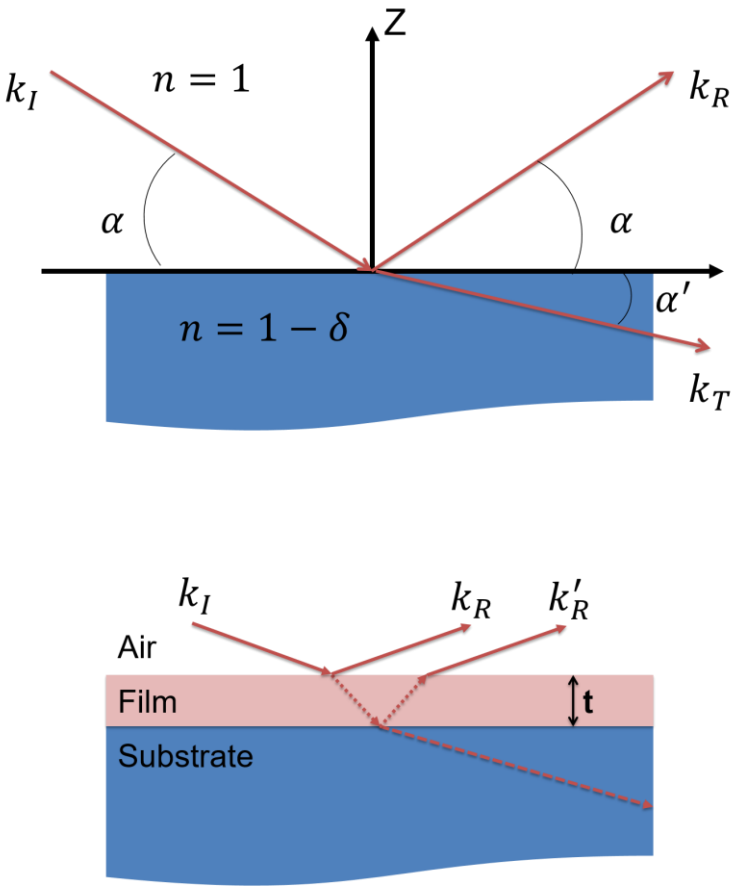

Figure 3.11 Sketch of reflection and refraction on single interface (top) and on a thin film sample with 2 interfaces (bottom).

sharp interface separating two materials. The change of the direction is dominated by the difference of index of refraction. In X-ray region, the index of refraction n is typically less than unit[122], described as $n = 1 - \delta$ (absorption effect is neglected) where $\delta = \frac{2\pi\rho r_0}{k^2}$ and is normally in the order of 10^{-6}, ρ is the number density of electrons and r_0 is the scattering amplitude per electron. As depicted in Figure 3.11 top, the incident wave vector is noted as k_I, and the amplitude is a_I. Similarly, the reflected and the transmitted wave vectors are k_R and k_T, with amplitudes a_R and a_T, respectively. So, deriving from boundary conditions, the Snell's law can be expressed as[131]

$$cos\alpha = ncos\alpha' \qquad \text{Eq. 3.5}$$

And Fresnel equation can be written as[132]

$$r = \frac{sin\alpha - nsin\alpha'}{sin\alpha + nsin\alpha'} \qquad \text{Eq. 3.6}$$

$$t = \frac{2sin\alpha}{sin\alpha + nsin\alpha'} \qquad \text{Eq. 3.7}$$

where r and t are the amplitude reflectivity and transmittivity, respectively. If we make $\alpha' = 0$ in the Eq. 3.5 and ignore the high order of small number δ, then the critical angle α_c for total external reflection can be obtained as $sin\alpha_c = \sqrt{2\delta}$. Then, we introduce 2 dimensionless counterparts $q = \frac{sin\alpha}{sin\alpha_c}$ and $q' = \frac{sin\alpha'}{sin\alpha_c}$. Thus, the Eq. 3.5 and Eq. 3.6 can be expressed as

$$q^2 = q'^2 + 1 \qquad \text{Eq. 3.8}$$

$$r(q) = \frac{q - q'}{q + q'} \qquad \text{Eq. 3.9}$$

$r(q)$ is complex function of q (related to the incident angle) and the measured XRR intensity $R(q)$ equals $r(q)r(q)^*$. Therefore, when $q \gg 1$ (i.e. much higher above critical angle), the reflectivity intensity falls off as $R(q) \cong (2q)^{-4}$, which is also called kinematical regime. When $q < 1$, q' is a pure imaginary number and therefore the measured intensity $R(q)$ identically equals to 1, which is total reflection. The reflectivity from a well-defined interface is called Fresnel reflectivity[133].

If we introduce one more interface into the system (e.g. one layer of thin film as depicted in Figure 3.11 bottom), then the reflected waves from two interfaces will interfere with each other and cause an oscillation of amplitude (known as Kiessig fringes). Similar to the Bragg's law, the thickness of the film can be derived from the period of this oscillation through[134]

$$n\lambda = 2tsin\theta \qquad \text{Eq. 3.10}$$

where n is an integer, λ is the x-ray wavelength, t is the film thickness and θ is the incident angle. Since momentum transfer in this geometry $Q = \frac{4\pi}{\lambda} sin\theta$. The thickness can be expressed as

$$t = \frac{2\pi}{\Delta Q} \qquad \text{Eq. 3.11}$$

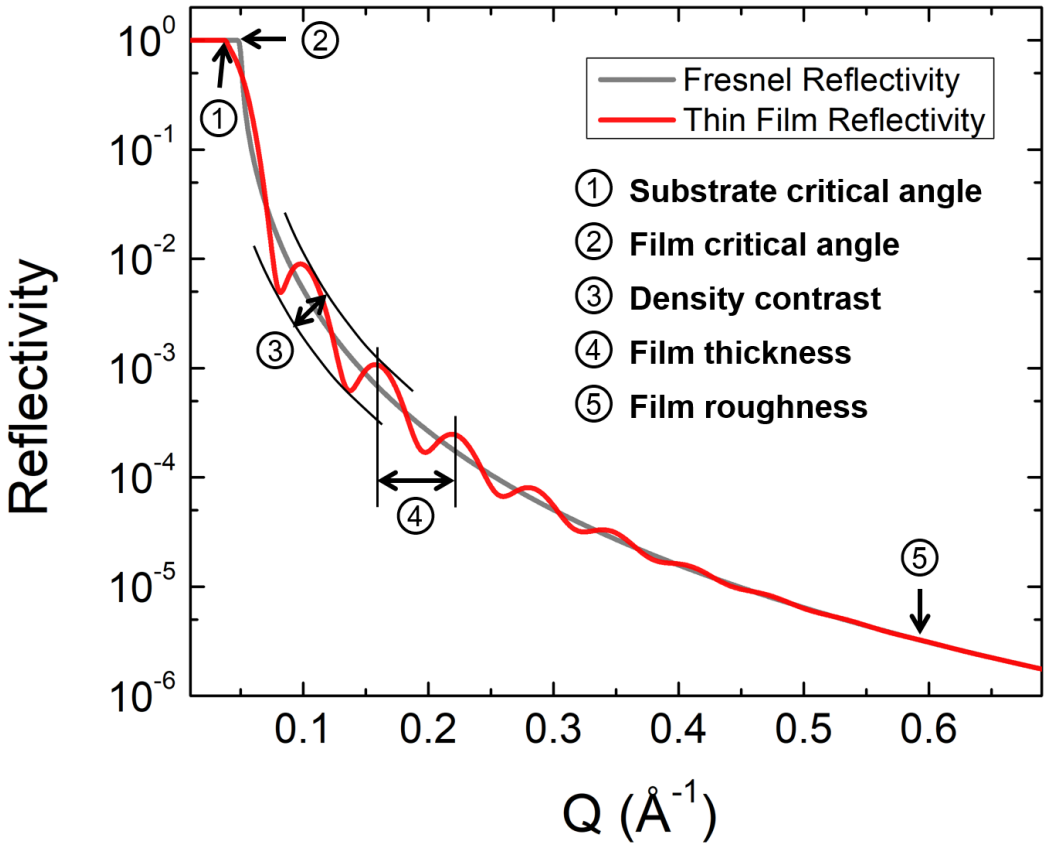

Figure 3.12 Theoretically calculated XRR for a model thin film sample with 100Å thickness and 5Å roughness (red line) as well as Fresnel reflectivity background (gray line).

Since XRR is a technique to reveal electron density profile, it also contains the information about the electron density and interface roughness. Figure 3.12 red line gives an example XRR of 100Å thick film with 5Å rms roughness[135]. The gray line is Fresnel reflectivity from an ideal mirror. The point marked as ① and ② are critical angles for substrate and film, respectively. ③ is the oscillation amplitude which depends on the electron density contrast of both interfaces. ④ is the oscillation period from which the film thickness derives. ⑤ is the damping point at

which the Kiessig fringes totally disappear. At this point, $\frac{2\pi}{Q}$ is comparable with film roughness and leads to an average of constructive and destructive interference. Therefore, through the analysis (fitting) of XRR measured on thin film sample, one can obtain the information about film density, thickness and roughness.

3.4.3 Crystal Truncation Rod

In previous section, we have explained that the diffraction pattern of a crystal is essentially the Fourier transform of its lattice in real space. For an infinite 3D periodic structure (i.e. a perfect

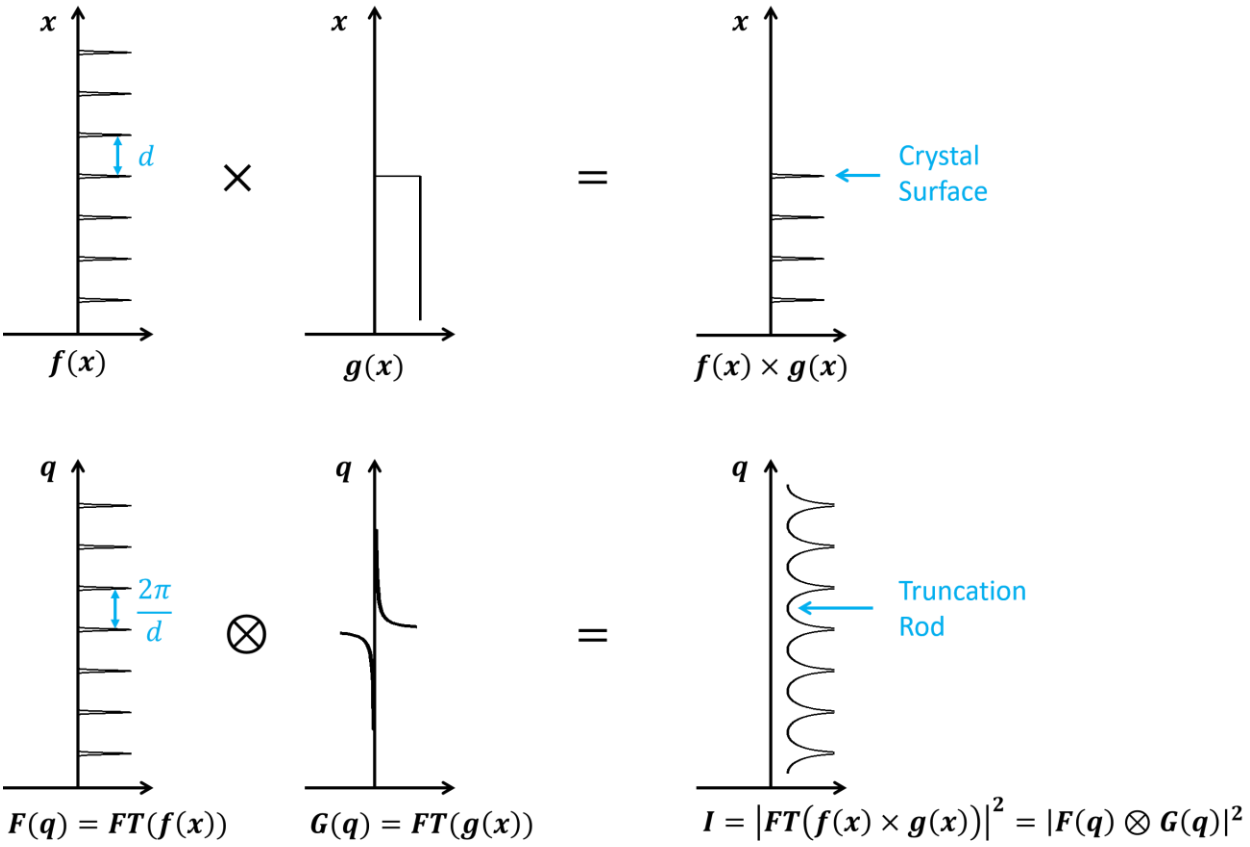

Figure 3.13 Illustration of how CTR generates through convolution theorem.

single crystal with infinite volume), the Fourier transformation yields the discrete points, which are known as Bragg peaks, in the reciprocal space. Those Bragg peaks are infinitely narrow and described by "delta function". However, if the real space structure is not infinite along one of the dimensions, instead, with a surface (i.e. a truncated crystal), a step function needs to be multiplied in real space. The Parseval's theorem tells us that the Fourier transform of the product of two functions equals the convolution of the Fourier transform of each function. As illustrated in Figure 3.13, $\boldsymbol{f(x)}$ is the periodic crystal lattice array along one direction with infinite range and $\boldsymbol{g(x)}$ is a step

function which defines the crystal truncated surface. Then the measured intensity is

$$\boldsymbol{I = \left|FT\left(f(x)\times g(x)\right)\right|^2 = |F(q) \otimes G(q)|^2} \qquad \text{Eq. 3.12}$$

where $\boldsymbol{F(q)}$ and $\boldsymbol{G(q)}$ are the Fourier transform of $\boldsymbol{f(x)}$ and $\boldsymbol{g(x)}$ respectively. The difference between $\boldsymbol{I}$ and $\boldsymbol{F(q)}$ clearly shows that the "ideal" diffraction pattern is smeared out to produce a series of rods in the direction perpendicular to the truncation surface. Those are the so called surface truncation rods, or crystal truncation rods (CTR)[136-141].

Since CTR analysis includes a step function, it's very sensitive to the perturbation at the edge of the step function. Here, we present another approximation to numerically derive CTR intensity. In the specular reflection geometry, we need only consider the lattice sum in the direction of the

surface normal (usually denoted as z direction). The sum over the other two directions leads to the usual product of delta function. Assuming A(Q) is the scattering amplitude from a layer of atoms and same for all layers. Therefore, the whole scattering amplitude, which is also proportional to the structure factor, can be expressed as

$$F^{CTR}(Q) = A(Q)\sum_{n=0}^{\infty} e^{iQ_z an} = \frac{A(Q)}{1 - e^{iQ_z a}} \qquad \text{Eq. 3.13}$$

where Q_z is momentum transfer in z direction and a is lattice constant in z direction.

Now we are considering a simple deviation of the top layer from the bulk in the direction of the surface normal (as shown in Figure 3.14 left). We denote this small displacement as $a(1+\delta)$, then the scattering amplitude with a surface layer is

$$F^{CTR}(Q) = \frac{A(Q)}{1 - e^{iQ_z a}} + e^{-iQ_z a(1+\delta)} \qquad \text{Eq. 3.14}$$

if we further simplify $A(Q)$ as a constant independent of Q, then we can plot the calculated CTR

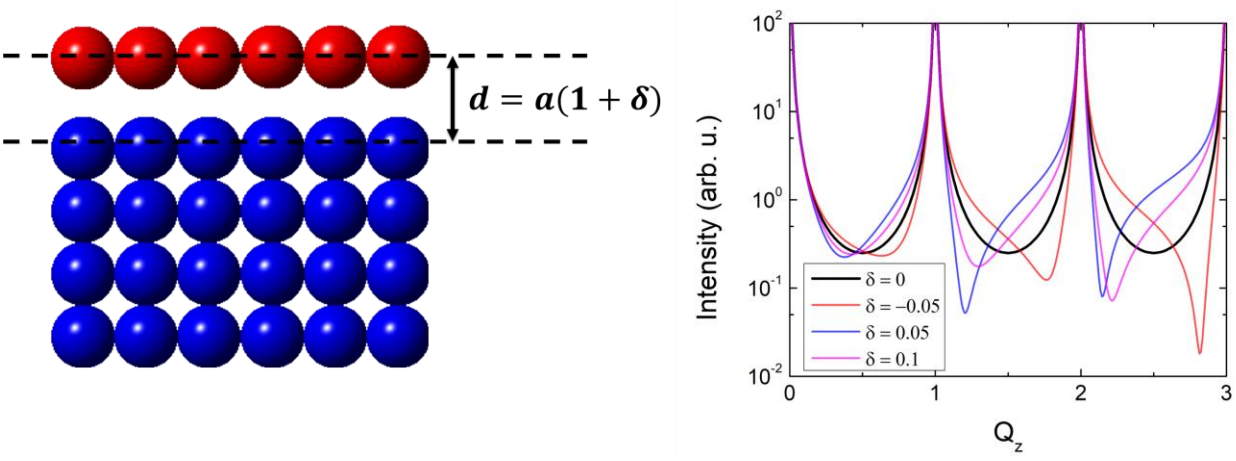

Figure 3.14 Sketch of surface layer displacement and CTR intensity simulation with different displacement δ.

intensity $I \propto |F^{CTR}|^2$ with different surface layer displacement δ (as shown in Figure 3.14 right).

From this theoretically calculated CTR, we can see that even 5% spacing shift for a single surface layer can obviously skew the intensity between the Bragg maxima. In real cases, we should consider more than one atoms layer as well as the roughness and some other parameters. The typical way to solve an unknown structure with CTR measurement is by model fitting. The final optimized model structure is only a possible structure and most likely a local minimum. Therefore, the proper starting structure is critical for CTR data analysis. Also the final structure should be physically and chemically reasonable.

3.4.4 Reciprocal Space Mapping

We have introduced reciprocal lattice in previous section, which is the Fourier transform of the Bravais lattice (also known as the direct lattice). While the direct lattice exists in real space and is what one would commonly understand as a physical lattice, the reciprocal lattice exists in reciprocal space (also known as momentum space). Due the properties of the Fourier transformation, the reciprocal lattice constant describes the period of direct lattice and vice versa. Therefore, even though 2 crystalized materials are physically separated in real space, their reciprocal lattices will share the same origin. In this way, it will be easy and obvious to compare

the difference of their reciprocal lattices, which can lead to an easily comparing of lattice constant in real space. As shown in Figure 3.15, 2 crystals (for simplification, both of them are cubic) are spatially separated in really space (top). The vertical and parallel lattice constants for them are $D_\perp$ and $D_\parallel$, $d_\perp$ and $d_\parallel$, respectively. After transformed into reciprocal space (bottom), their reciprocal lattices share the same origin (000). Since those 2 crystals share the same orientations in really space ($\vec{a}$ and $\vec{c}$), they still share the same orientations in reciprocal space ($\overrightarrow{a^*}$ and $\overrightarrow{c^*}$) but are with reciprocal

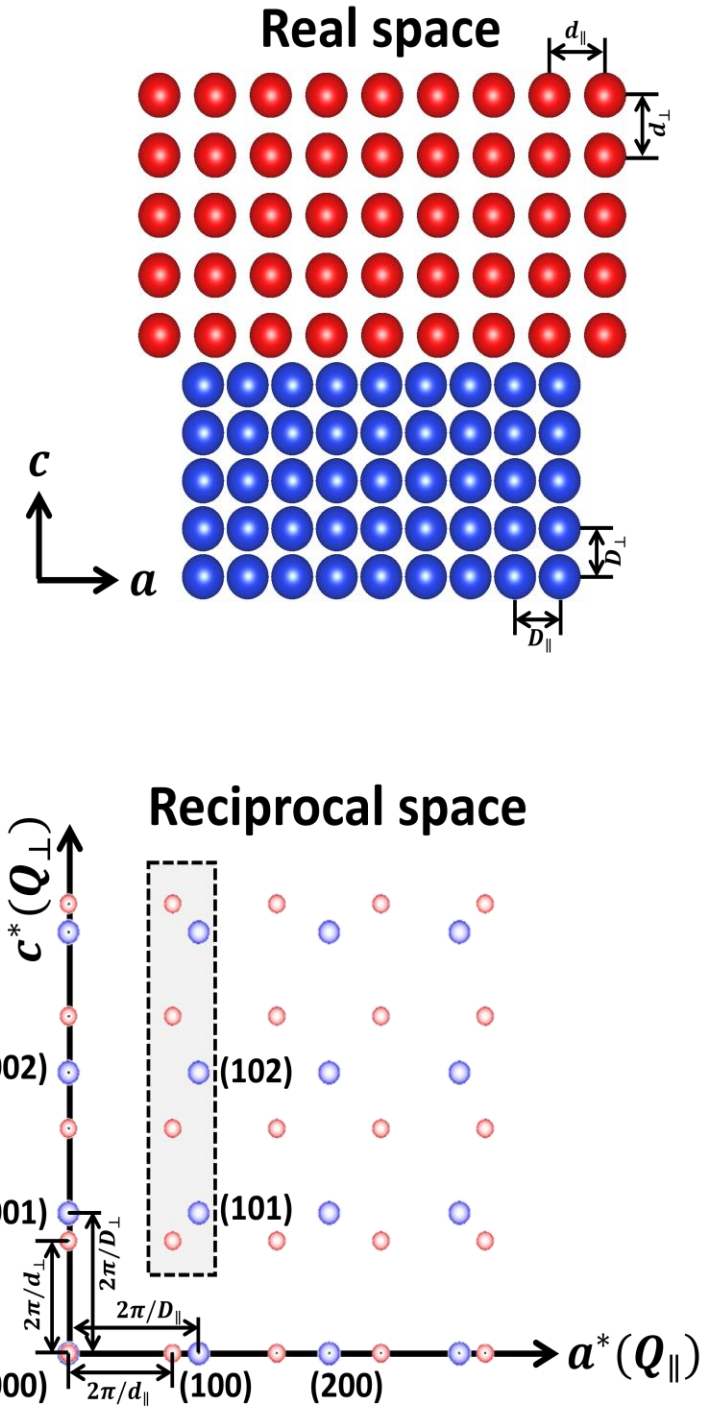

Figure 3.15 Bravais lattices of 2 crystals in real space (top) and the corresponding reciprocal lattices in reciprocal space (bottom).

lattice constant $\Delta Q = 2\pi/d$. The reciprocal space mapping (RSM) is a technique to map out all the scattered intensity in a confined area in reciprocal space[124, 140-145], as the area boxed out in Figure 3.15 bottom. It's very similar to the pole figure measurement but with much higher resolution and in a more restricted Q area. In the reciprocal space map, the location difference (both the direction and distance from the origin) of the reciprocal lattice points for 2 crystals represents their structural differences (orientation and lattice constant, respectively) in real space. If 2 sets of reciprocal lattices are overlapped, that means those 2 crystals share identical structure in the really space. This conclusion is also true for individual directions. Since RSM is a way to distinguish the structure differences of multiple crystals, it's very useful to investigate the epitaxy of crystalized thin films.

3.5 In operando X-ray and electrochemistry experimental setup

In order to simultaneously perform X-ray scattering and electrochemistry measurements, a specially designed transmission cell[146] (Figure 3.16) was used to hold samples in a sealed space which allowed the X-ray beam to pass through. The thin film samples are cut into 10mm × 3mm size and sealed into transmission cell in the glovebox filled with Argon. Li metal is used as both the counter and reference electrodes which forms a half-cell geometry. The electrolyte inlet and outlet (syringe + stopcock + Teflon tubing) are attached via PVDF compression fittings on the cell

body's NPT fittings. Electrolyte (1:1 EC/DMC + 1M $LiPF_6$) is injected into the cell right before in operando measurement. The extra electrolyte left the in syringes can make up the possible electrolyte leakage in the cell body as well as keep it fresh.

The electrochemical potential of the working electrode and its associated current are controlled by a CHI760E potentiostat. Usually two modes of cycling will be performed, Potentiostatic and Galvanostatic. In the potentiostatic mode, we commonly sweep the potential at the rate of 0.2 – 1 mV/s and measure the current. In the Galvanostatic mode, the applied current depends on the sample's capacity and how fast we want to cycle, typical tens of micro Ampere.

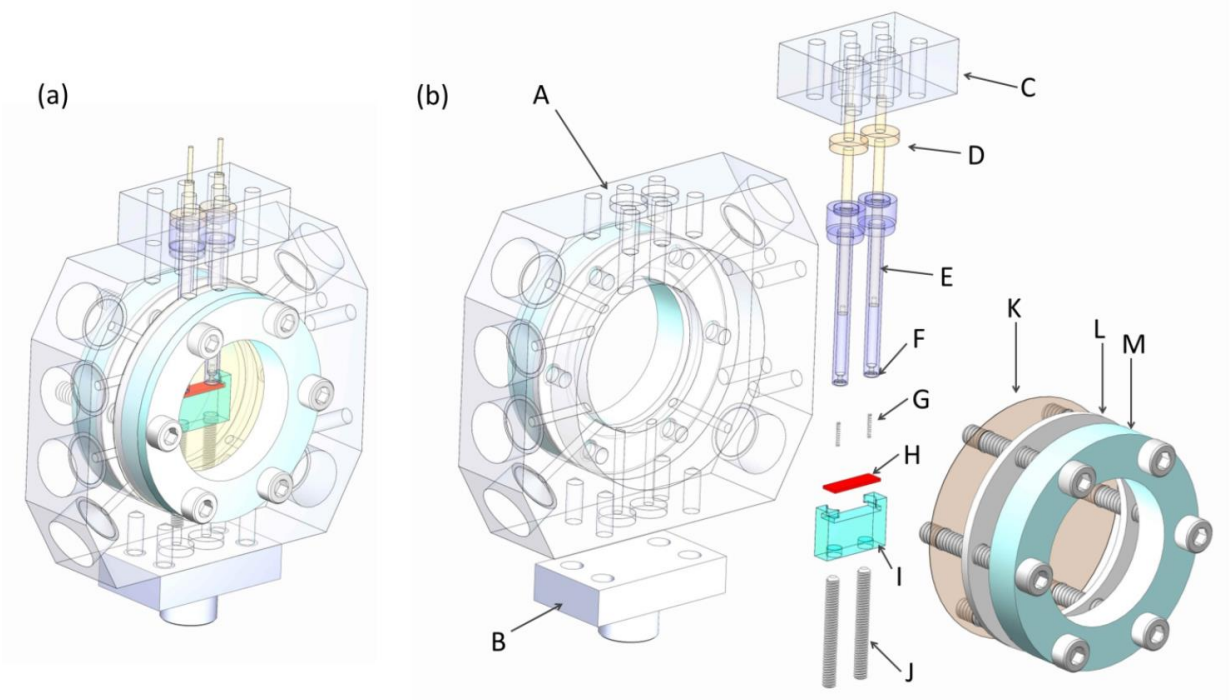

Figure 3.16 (a) assembled transmission cell and (b) exploded view. (Designed by T.T. Fister)

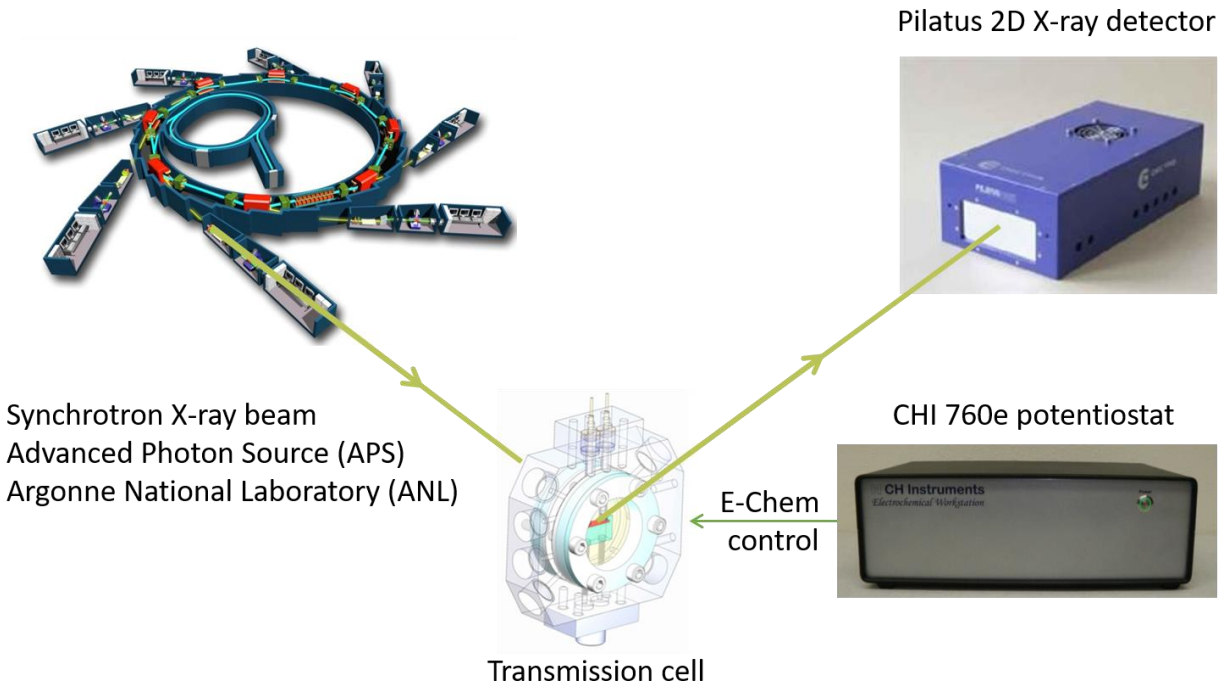

Figure 3.17 Scheme of the *in operando* X-ray measurement setup

The overall in operando experiment setup is shown in Figure 3.17. The transmission cell is mounted on the synchrotron X-ray diffractometer. Due the open angle limitation of the transmission cell, all the in operando X-ray measurements are performed in Bragg–Brentano geometry below 30° incident beam angle. With typical 20 keV photon energy, it can reach 10 $Å^{-1}$ vertical momentum transfer (Q_z). The CHI 760E potentiostat is connected to the transmission cell through the 2 working electrodes on the top of cell body and counter/reference electrode on the side. The X-ray scattering and electrochemical cycling can be performed and recorded simultaneously to in operando monitor the structure changes in different electrochemical states.

Chapter 4 : Patterson Function Analysis and *In Operando* Study of Ge/Ti Multilayer

In the previous chapter, we have briefly introduced the idea of multi-layer architecture for group IV intermetallic anodes. Since those anodes materials undergo alloy reaction during lithiation / delithiation, they are not required to be crystalized. Therefore, the low angle XRR becomes the most useful measurement to monitor the structure changes. The common analysis for XRR is through model fitting which starts from a guessed model. However, this method is intrinsically hard and inaccurate for multilayer due to large number of fitting parameters. In this chapter, we will introduce a Patterson function based analysis method which can directly give out the structure of multi-layer thin films from the XRR.

4.1 Mathematical principles for Patterson function

For X-ray scattering, the measured intensity is the modulus squared of the *scattering amplitude* $\mathcal{A}(\boldsymbol{Q})$ $(I(\boldsymbol{Q}) = |\mathcal{A}(\boldsymbol{Q})|^2)$. Under the kinematical approximation where multiple scattering effects can be neglected, the scattering amplitude $\mathcal{A}(\boldsymbol{Q})$ is given by[147]

$$\mathcal{A}(\boldsymbol{Q}) = \int_V \varrho(\boldsymbol{r}) e^{-i\boldsymbol{Q}\boldsymbol{r}} d\boldsymbol{r} \qquad \text{Eq. 4.1}$$

where $\boldsymbol{Q}$ is momentum transfer (scattering vector), $\boldsymbol{r}$ is real space position, and $\varrho(\boldsymbol{r})$ is the *scattering length density* distribution, equal, in the case of X-ray scattering, to the *electron density*

distribution $\rho(\boldsymbol{r})$ multiplied by scattering length of an electron $b_e = r_e(\frac{1+cos^2 2\theta}{2})^{1/2}$.

In specular reflection system (Bragg–Brentano geometry), we are considering one dimension system with one variable z (along the surface normal of sample). The scattering vector $\boldsymbol{Q}$ can be simplified into a scalar $Q = \boldsymbol{Q}_z$ Then the *scattering amplitude* can be described as

$$\mathcal{A}(Q) = b_e \int_{-\infty}^{\infty} \rho(z) e^{iQz} dz \qquad \text{Eq. 4.2}$$

By partial integration

$$\mathcal{A}(Q) = \frac{-b_e}{iQ} \int_{-\infty}^{\infty} \rho'(z) e^{iQz} dz \qquad \text{Eq. 4.3}$$

Applied this formula to Fresnel condition, where the electron density is a step function $\rho(z) = 0\ when\ z < 0$ and $\rho(z) = 1\ when\ z > 0$. Therefore, the derivative of $\rho(z)$ is a delta function, then

$$\mathcal{A}_F(Q) = \frac{-b_e}{iQ} \int_{-\infty}^{\infty} \delta(x)\, e^{iQz} dz = \frac{-b_e}{iQ} \qquad \text{Eq. 4.4}$$

Combing Eq. 4.3 and Eq. 4.4, it's gives

$$\mathcal{A}(Q) = \mathcal{A}_F(Q) \int_{-\infty}^{\infty} \rho'(z) e^{iQz} dz = FT(\rho'(z)) \qquad \text{Eq. 4.5}$$

Then the Fresnel-normalized reflection $nR(Q)$ intensity, $\frac{R(Q)}{R_F(Q)}$, where $R(Q)$ is measured specular reflectivity and $R_F(Q)$ is the calculated Fresnel reflectivity, can be written as

$$nR(Q) = \frac{R(Q)}{R_F(Q)} = \left|\frac{\mathcal{A}(Q)}{\mathcal{A}_F(Q)}\right|^2 = \left|\int_{-\infty}^{\infty} \rho'(z) e^{iQz} dz\right|^2 \qquad \text{Eq. 4.6}$$

This formula is called Master Formula, first proposed by Als-Nielsen in 1986[148]. Since all the

derivations are based on the kinematical approximation, this equation is only valid in the kinematical regime of X-ray reflectivity (i.e. the incident beam angle is well above the critical angle, $\theta \gg \alpha_c$).

By using Parseval's theorem, the Fourier transform of $nR(Q)$ can be described as

$$FT\big(nR(Q)\big) = FT\left(\frac{R(Q)}{R_F(Q)}\right)$$
$$= \frac{1}{2\pi}\int FT\big(\rho'(z)\big)FT^*\big(\rho'(z)\big)\, e^{-iQz}dQ$$
$$= \rho'(z) \otimes \rho'(-z) \qquad \text{Eq. 4.7}$$

The direct Fourier transformation of measured intensity (normalized by Fresnel reflectivity in low-angle regime) is also called Patterson function[149]. From the Eq. 4.7, we know that the Patterson function for low-angle reflectivity equals to the autocorrelation of vertical electron density gradient $\rho'(z)$. Since the Patterson function can be obtained directly by a numerical Fourier transformation of the data, it is a model-independent way to directly probe the electron density profile from XRR.

4.2 The application of Patterson function analysis to multi-layer thin film system

In principle, the Patterson function analysis can be used to investigate the X-ray reflectivity data of all thin film models, including single layer as well as multiple layers. However, its superior

advantages are best reflected when dealing with periodic multi-layer system. On the one hand, the model fitting analysis of XRR data for extended multilayer structures can be challenging, especially when each of the repeated layer pairs may not be precisely identical and thus requires a model with huge numbers of parameters to describe the structure. One the other hand, for a periodic function with limited number of periods, the amplitude of its autocorrelation function is proportional to its period quantity. That means, for a multi-layer system, more repeated unit layers will lead to higher Patterson function amplitude. Figure 4.1 compares the Patterson functions for

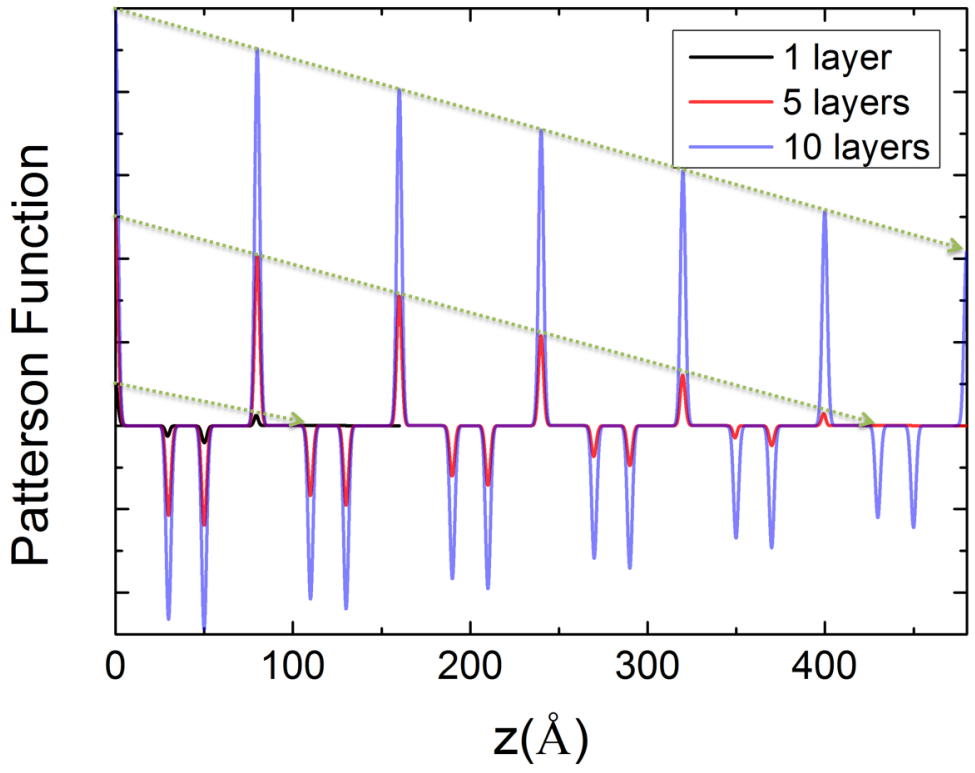

Figure 4.1 Patterson functions for a bilayer thin film(black) and periodic multi-layer thin films with 5 repeated (red) and 10 repeated (blue) identical bilayers. Dash line shows the decay trend.

a bilayer, 5 repeated bilayers and 10 repeated bilayers systems. The amplitude of Patterson function for 10 repeated bilayers are much higher than the amplitude for a single bilayer unit. This increase in Patterson function amplitude makes its features to be more distinguishable and easier for analysis.

An illustration of the Patterson function analysis for a simple two-layer multilayer is depicted in Figure 4.2. The simulated multilayer system consists of N_{ML}=10 periods of a 30 Å thick high-density layer followed by a 50 Å thick low-density layer on top of a semi-infinite substrate. It also shows the electron density profile for two bilayers, along with its derivative (Figure 4.2(a)). The simulated X-ray reflectivity, R, from the entire multilayer structure (Figure 4.2(b)) includes Bragg peaks associated with the multilayer periodicity ($Q = 2\pi/d_{ML}$, where d_{ML} = 80 Å), and high frequency oscillations associated with the total multilayer thickness (with a period of $\delta Q = 2\pi/[N_{ML}d_{ML}]$. Also shown is the Fresnel reflectivity from the substrate, R_F . The Patterson function ($FT(R/R_f)$) is compared with the autocorrelation of the derivative of the election density in Figure 4.2(c), providing a graphical demonstration of the validity of Eq. 4.7. Here, it can be seen that first three features in the Patterson function correspond to the thicknesses of the high density layer (at 30 Å), the low density layer (at 50 Å) and the multilayer period (at 80 Å). Note that in this case, the individual layer thicknesses appear as *negative* peaks while the multilayer

period appears as a *positive* peak, since the sign of these features are due to the product of the interfacial density discontinuities associated with these features (i.e., negative peaks in P(z) are due to interference between interfaces with "up" and "down" density changes, while positive peaks are associated with two "up" or two "down" interfaces). Also seen in the derived Patterson function

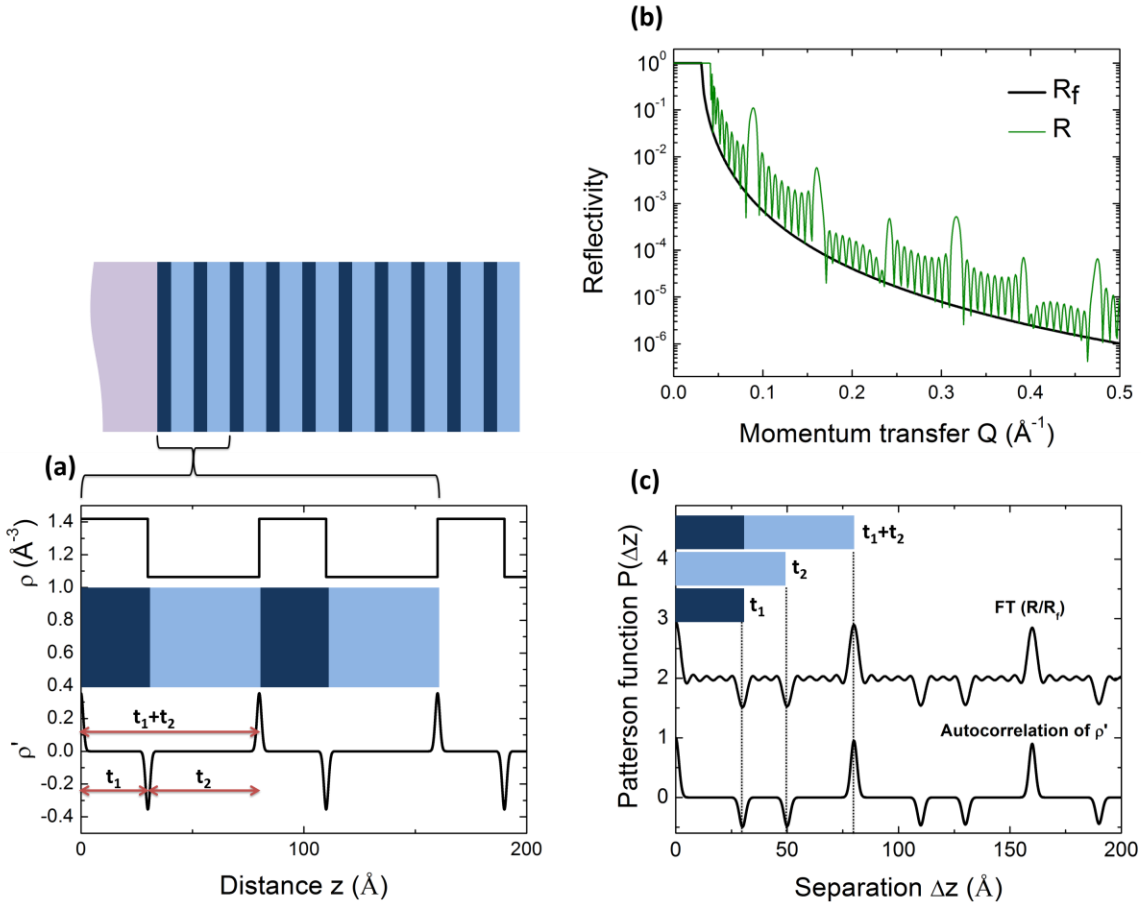

Figure 4.2 Patterson function simulation for an idealized periodic multilayer with N = 10 periods grown on a substrate. (a) Multilayer model for simulation (direct view of this multilayer architecture, electron density profile for two bilayers and its derivative). (b) Simulated X-ray reflectivity, R, and Fresnel reflectivity of the substrate, R_f. (c) Comparison between the derived Patterson Function (by Fourier transform (FT) of the normalized X-ray reflectivity signal, calculated to Q = 1 A^{-1}) and the autocorrelation of the derivative of the election density. The position of each peak within the first period of the Patterson function has been assigned to the associated film thickness.

are small high frequency oscillations with period $2\pi/Q_{max}$ that are due to the truncation of the Q-range ($0 – 1\ Å^{-1}$) over which the Fourier transform was calculated[150].

With increasing number of layers in one unit for a periodic multi-layer thin film, the featured peaks of Patterson function in one period will increase as $n(n-1)+1$, where n is the number of layers in one unit. Figure 4.3 shows the simulated Patterson functions for periodic multi-layer thin films with 2, 3 and 4 layers in each unit. When $n = 2$, there are $2\times(2-1)+1 = 3$ featured peaks in one period. While when $n = 4$, there are $4\times(4-1)+1 = 13$ featured peaks in one period.

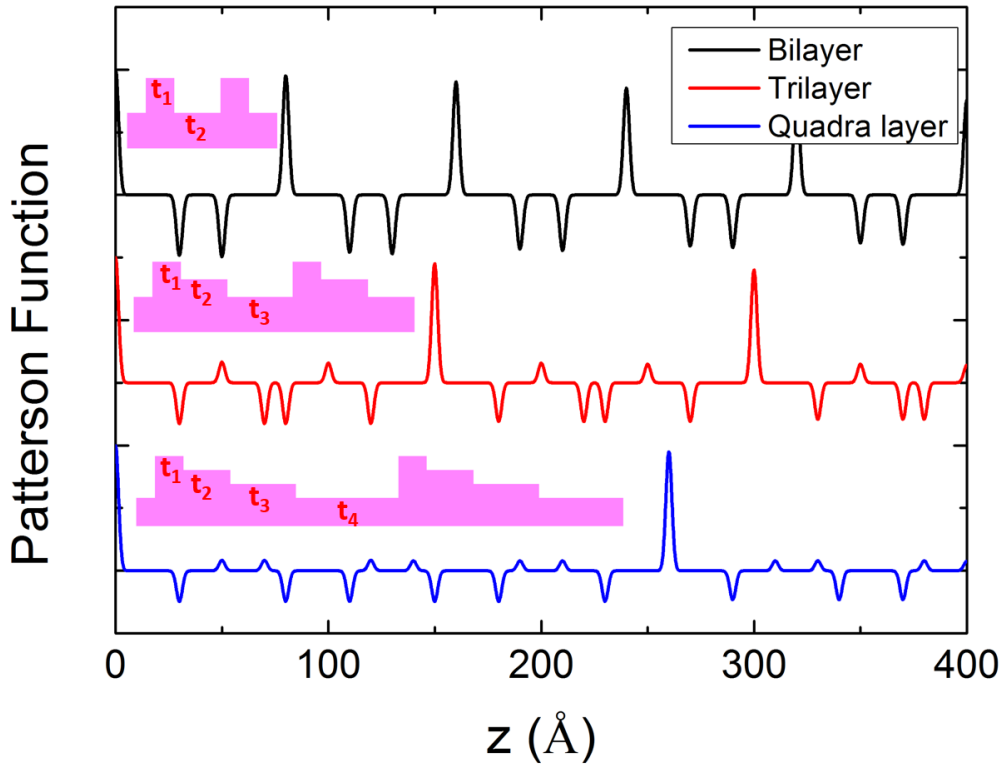

Figure 4.3 Simulated Patterson functions for periodic multi-layer thin films with 2, 3 and 4 layers in each unit

In the first period of the Patterson function, the positions of each featured peak is the thickness of a single layer or a combination of adjacent layers in one unit. As shown in Figure 4.4, all of the 13 featured peaks in the first period of Patterson function (for a periodic multi-layer thin film with 4 layers in one unit) have been assigned to the corresponding thicknesses of layer(s) in one unit. The sign of each peak obeys the same rule as described above, as the product of interfacial density discontinuities at 2 boundaries of a layer (or a combination of adjacent layers). Due to the one-to-one correspondence between the peak position and layer thickness, one can easily tell the

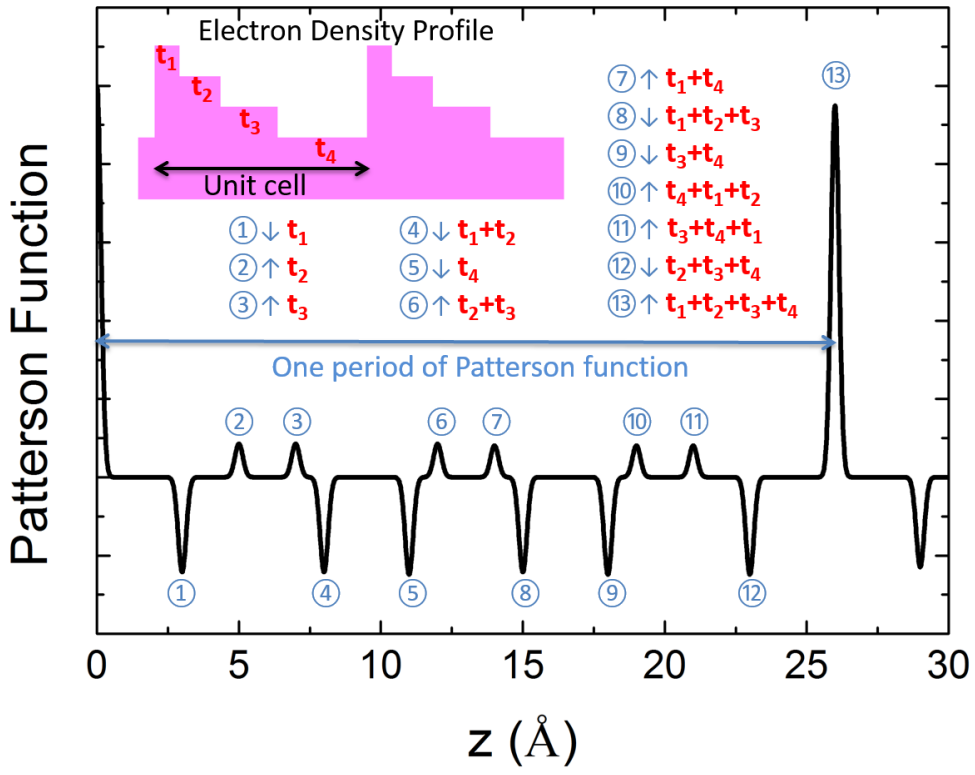

Figure 4.4 The 13 featured peaks in the first period of Patterson function for a periodic multi-layer thin film with 4 layers in one unit and their corresponding thickness

thickness of each individual layers in one unit directly from the Patterson function. Combined with the sign of each peak, the electron density profile can also be distinguished.

In one Patterson function, there are 3 most obvious thicknesses which can be easily distinguished. The first two are the thickness for the 2 thinnest layers which are corresponding to the positions of first 2 peaks. And the third one is the thickness for a whole unit cell which is represented by the period of Patterson function. Therefore, when $n \leq 3$, it's quite straightforward to directly read the thicknesses of each layers from the Patterson function. However, when there are more than 3 layers in one unit, it becomes hard to directly tell the thicknesses without carefully

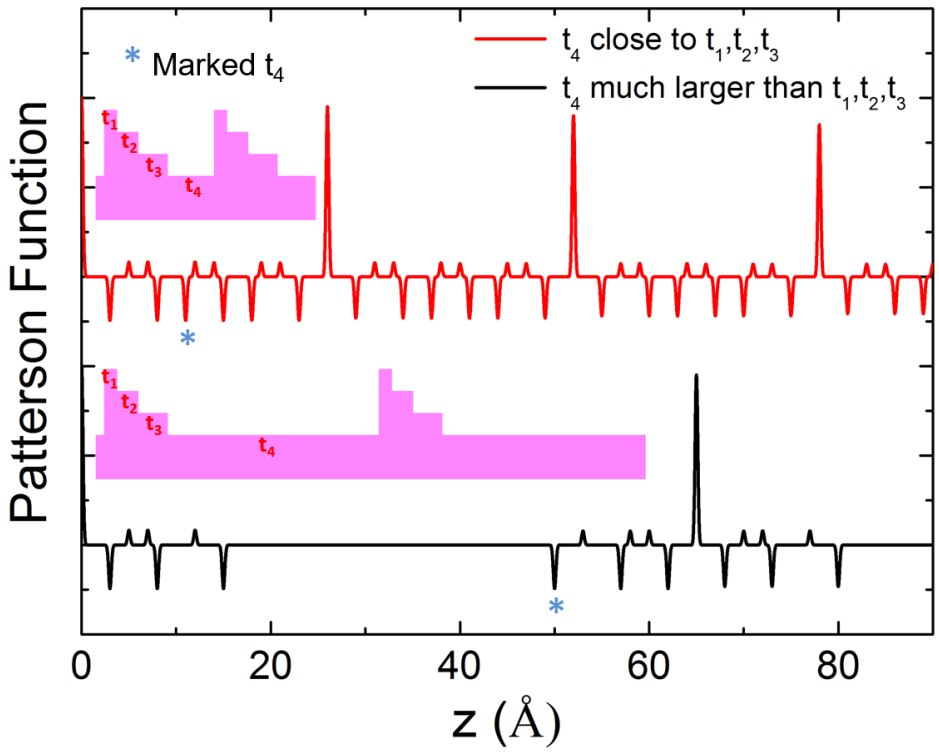

Figure 4.5 Illustration for the changes of Patterson function when dramatically increase the thickness of one component layer within the unit.

peak distinguishing and sorting. In this case, we may consider a way to make one thickness (and its corresponding peak) much more "outstanding" which can be directly acquired. For example, if allowed, we can prepare the multi-layer sample with a relatively much thicker layer within the unit (as shown in Figure 4.5, $t_4 \gg t_1,\ t_2, t_3$). Then the thickness of this thick layer can be directly read from the Patterson function as the position of first peak after a long flat inter-node region.

As we discussed above, one of the superior advantages for Patterson function analysis is the quick thickness estimation for multi-layer thin film. Figure 4.6 gives an example of thickness estimation for a real Ge/Ti multilayer. The top most curve is the Patterson function for this multilayer (i.e. Fourier transform of the Fresnel-normalized reflection), followed by the thickness estimating procedure.

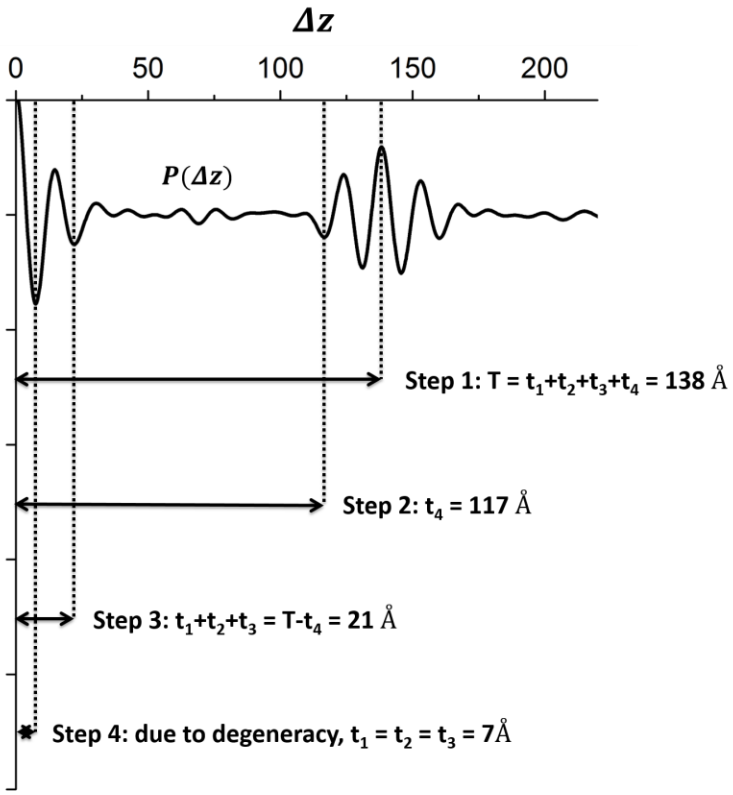

Figure 4.6 Step by step instruction about quick estimating for each layer's thickness of a Ge/Ti multilayer.

Step 1, the period of Patterson function represents the thickness of one unit cell (repeated layer).

Therefore, it can be easily read out that $T = t_1 + t_2 + t_3 + t_4 = 138$Å.

Step 2, since we artificially made Ge layer (t_4) much thicker than other layers, Patterson function became repeated pattern at each node with long flat inter-node region. The first peak in second pattern shows the thickness of Ge layer $t_4 = 117$Å.

Step 3, though calculation, the total thickness of other layers (Ti and Ti/Ge alloy) is $t_1 + t_2 + t_3 = 21$Å

Step 4, after locating the peak representing the total thickness of Ti and Ti/Ge alloy layers at 21Å, we found that there are only 3 peaks between 0 and 21Å instead of 6 peaks (t_1, t_2, t_3, $t_1 + t_2$, $t_2 + t_3$ and $t_1 + t_2 + t_3$) which means there is degeneracy (overlapping). This degeneracy can only happen when $t_1 = t_2 = t_3 = 7$Å.

For more precise study, an estimating without error is not enough. But this estimating provides good pre-knowledge for the its structure. Based on it, we can determine a model for the electron density profile $\rho(z)$ (or more direct, the derivative of the electron density profile $\rho'(z)$). In the limit of a step-wise electron density profile (i.e., as appropriate to a multilayer structure, each interface in the density gradient, $\rho'(z)$, can be described by a Gaussian function defined by three parameters, corresponding to the interface position z_0, an rms width σ (describing the interface roughness) and the interfacial density contrast $\Delta\rho$. Consequently, the Patterson function

is described by a sum of Gaussian functions that represent the convolution of the contributions from separate interfaces associated with the interference between X-rays scattered at each interface described by separations $z_i - z_j$, widths $(\sigma_i^2 + \sigma_j^2)^{1/2}$, and magnitudes $\Delta\rho_i\Delta\rho_j$ of the two interfaces (i and j). Ultimately, the structural model derived from the insights from the Patterson function analysis can be optimized and quantified by a χ^2 optimization along with the parameter uncertainties.

4.3 *In operando* study of reversible conversion reaction for Ti_xGe alloy in Ti/Ge multilayer

Previously it was demonstrated that multilayers consisting of alternating thin films of amorphous silicon and conducting adhesive metal layers allowed the intrinsically high Li-capacity of silicon to be combined with the reversibility of ultrathin silicon films and the conductivity of a composite material while maintaining a high Coulombic efficiency[146, 151, 152]. In analogy to Si, we furthered our research to another group IV intermetallics, Ge, due to some of its superior advantages over Si which we have discussed in Chapter 2.1. Ti was chosen as the conducting adhesive metal interlayers.

4.3.1 Experimental Details

Sample Fabrication: Ge/Ti multilayers were deposited using DC magnetron sputtering. The rotary magnetron sputtering system was customized with two sputtering targets set horizontally.

The base pressure was $5x10^{-7}$ Torr, the deposition pressure was 2.3 mTorr of Ar, and the power for both targets was 215 W. Target masks were designed to achieve uniform films. The growth rate was calibrated using XRR. The Ge/Ti multilayers were deposited on fused quartz at room temperature by translating the substrate holder between the Ti and Ge targets, to grow alternating layers of 20 Ti/Ge bilayers, with a bottom layer of Ti and a top layer of Ge. The sample used for XRR measurements had nominal film thicknesses of 20 Å Ti and 100 Å Ge, while that for the TEM results were 50Å Ti and 100Å Ge. Galvanostatic measurements of the extended cycling performance of the Ge/Ti multilayers were tested at a 1C rate (using a multichannel Arbin cycler) to probe the stability and performance of a 20 periods multilayer with 100Å Ge and 40 Å Ti layer thicknesses and is compared to a thin Ge film with the same overall thickness (2000 Å).

Transmission Electron Microscopy: The cross-sectional TEM samples were prepared by a FEI Helois focused ion beam (FIB). After the thin section has been mounted on a FIB-grid, it is transferred into a TEM. The Ge/Ti multilayers thin film was then studied by a JEOL-2100F transmission electron microscope at 200 kV. High resolution electron microscopy (HREM) image showing phase contrast were taken to study the interface structure.

X-ray Reflectivity Measurements: In Operando XRR measurements were performed at 33BM-C of the Advanced Photon Source (APS) in Argonne National Laboratory (ANL) using an

X-ray photon energy of 20.00 keV with an incident flux of ~ 10^{10} photons per second. The X-ray beam (with cross-section of 2 x 0.2 mm^2 and divergence of 40 μrad = 0.0005 $Å^{-1}$ along 2θ direction) illuminated a 2 mm-wide by 3 mm-long area on the sample. The overall experiment setup follows the description in Chapter 3.5. Data were collected at fine intervals (Δq = 0.001$Å^{-1}$) using an area detector (Pilatus 100k). Each XRR scan took 5 minutes. In the present data, the statistical uncertainties in the experimental data are smaller than the systematic errors (e.g., associated with inhomogeneities in the sample thickness, for instance, as evidenced by the lack of Kiessig fringes), and therefore we have assigned a nominal and uniform relative uncertainty of 2% for each data point.

4.3.2 Results and analysis

Determination of the As-Deposited Ge/Ti *Multilayer Structure:* The as-deposited multilayer film was characterized by transmission electron microscopy (TEM) (Figure 4.7) and X-ray reflectivity (Figure 4.8(a)). The TEM image clearly shows a well-defined periodic multilayer structure, as expected. The nominal film thicknesses from the TEM image are 40 Å for Ti and 100 Å for Ge, similar to that expected from the growth conditions. The image contrast is proportional to variations in the local electron density. Instead of the expected bilayer structure with alternatively stacking between the Ge and Ti layers, it is apparent that the structure is more

complex. The TEM image has the appearance of a "pin-stripe" morphology, with a thin denser layer (dark) appearing at each interface between the Ge and Ti layers. This interfacial layer between the Ge and Ti layers is thought to be the formation of a higher density Ti_xGe alloy layer[153].

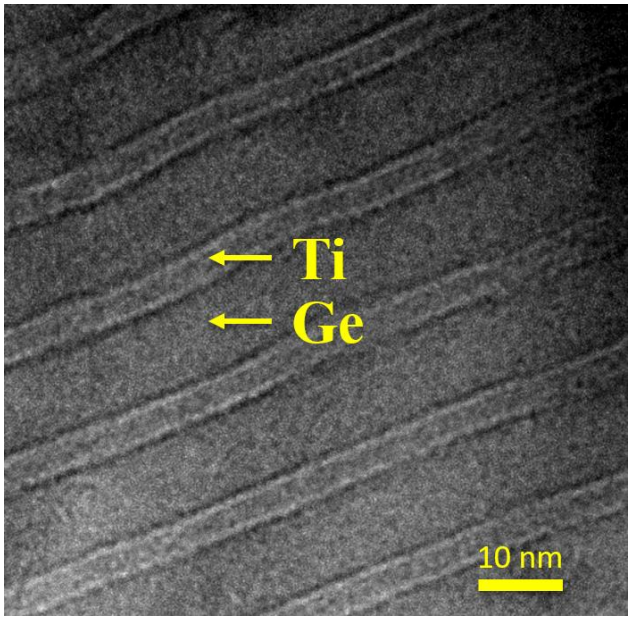

Figure 4.7 HREM image of the as-deposited Ge/Ti multilayer film. The contrast change is related to the electron density (darker areas correspond to higher electron densities).

The X-ray reflectivity data shows regular Bragg peaks associated with the multilayer structure, but without any evidence for the expected high frequency oscillations associated with total film thickness (e.g., Kiessig fringes). This, suggests that the multilayer structure and its morphology had a significant roughness. The derived Patterson function (Figure 4.8(b)) shows a more complex structure than expected for the simple bilayer. Instead of the expected bilayer structure shown in Figure 4.2 with three distinct spacings within each period, the Patterson function of the Ge/Ti multilayer has seven distinct intracell spacings. This is direct evidence that there are more than 2 layers in each unit multilayer period. Although this number directly matches $n = 3$ in the formula of $n(n-1)+1$, it cannot happen because of symmetry. Since the interface

layers between Ti and Ge should be identical, the simplest multilayer structure is one in which there are 4 layers within each unit period, corresponding to a core-shell structure embedded within a Ge matrix, which is also fully consistent with the TEM images. Model fitting of the Patterson function gives the average thickness for each layer (7.2 ± 0.1 Å for Ti layer, 115.7 ± 0.1 Å for Ge layer and 7.2 ± 0.1 Å for an intervening Ti_xGe alloy layer revealing that the thicker layer seen in the TEM images corresponds to Ge. Simulated electron density profile from model fitting is shown in Figure 4.8(c). This result is largely consistent with the intended deposition thicknesses (20 Å Ti and 100 Å Ge). The

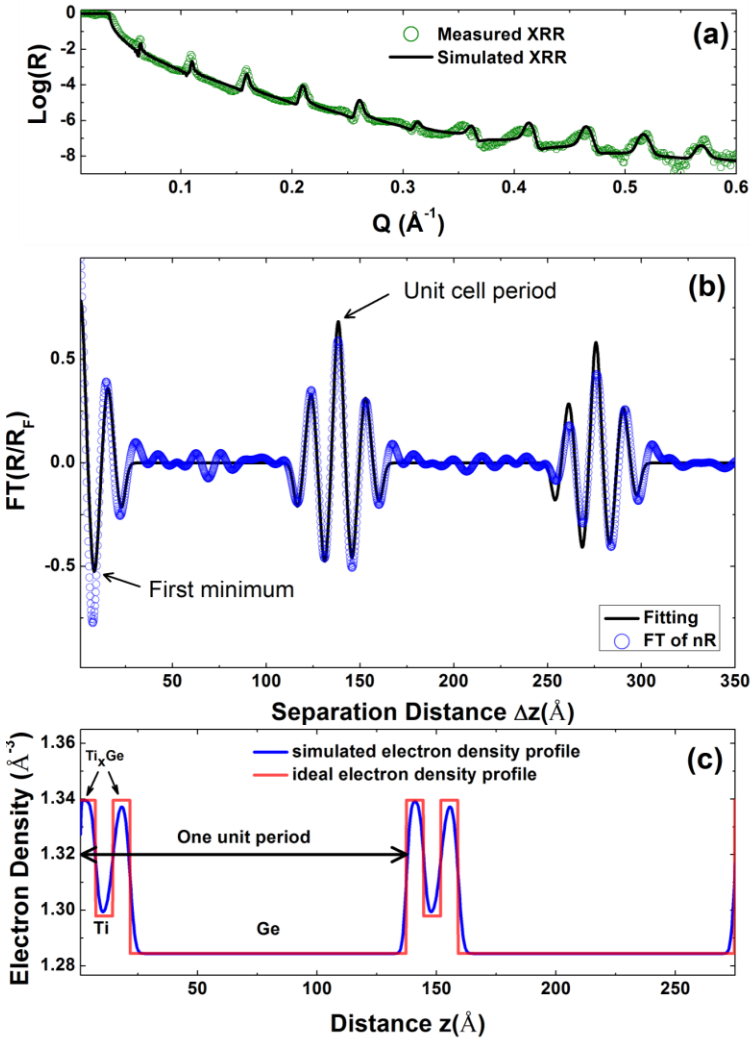

Figure 4.8 Patterson function analysis of the unlithiated Ge/Ti multilayer. (a) Specular X-ray Reflectivity data (green circle) and the calculated XRR signal (black line) using parameters obtained by fitting the observed Patterson function. (b) Calculated Patterson function (blue circle) and its fitting curve (black line). (c) Idealized model of electron density profile (red line) and calculated electron density profile from the Patterson function analysis (blue line).

simulated XRR signal, using fitted parameters (thickness, roughness and density contrast) from Patterson function, is then compared with the measured data in Figure 4.8(a). The good match indicates the effectiveness of our Patterson function analysis method for determining the layer thicknesses, densities and interface profiles in our complicated multilayer system. The small oscillations between the major peak in the Patterson function result from the termination of the Fourier transformation due to the finite measured range in Q (Q_{max} = 0.6 $Å^{-1}$).

In Operando Observations of Multilayer Lithiation and Delithiation: The normalized X-ray reflectivity data for the Ge/Ti multilayer sample under potentiostatic control are shown in Figure

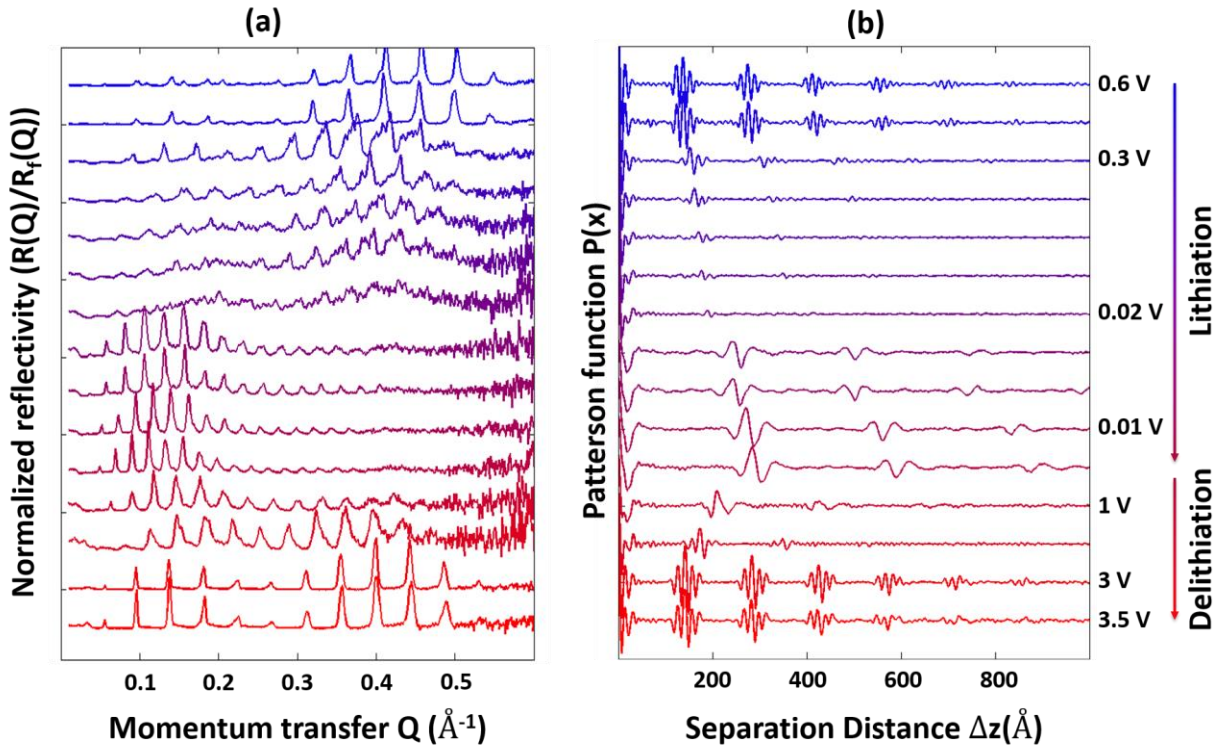

Figure 4.9 (a) In operando Fresnel-normalized X-ray reflectivity during electrochemical cycling. (b) The associated Patterson functions. The first measurement at each potential is denoted with its applied potential (right hand side).

4.9(a). The calculated Patterson function from XRR are shown in Figure 4.9(b). The measurements were performed as the applied electrochemical potential was subsequently held at 0.6 V, 0.3 V, 0.02 V, 0.01 V, 1 V, 3 V, and 3.5 V for a period. The seven-peak pattern in the Patterson function (with 3 positive and 4 negative peaks) observed at the start of cycle begins to diminish at voltages below 0.6 V as the multilayer loses coherence in response to lithiation (as seen previously)[146, 154, 155]. At the same time, the whole pattern gradually moves to larger distances, z, revealing that the multilayer period is increasing as expected for the lithiation of Ge, and suggesting that the whole multilayer increases in thickness. As the potential approaches 0.01 V, the shape of the Patterson function changes and evolves into a distinct three-peak pattern (with 1 positive and 2 negative peaks) slowly appears and becomes more defined as the potential is held at 0.01 V. Gradually sharper peaks result from the increasing coherence of the layers. This suggests that the whole film becomes homogeneously lithiated after being held at 0.01 V. Compared with the initial seven-peak pattern, the spacings in the three-peak pattern for the lithiated sample are found at much larger separations, indicating an expansion to more than two times that of the original thickness. The model fit to the Patterson function (Figure 4.10) at 0.01 V gives numerical results for the average thickness of each layer (22.3 ± 0.2Å for the Ti layer and 259.7 ± 0.2Å for the lithiated Ge layer). The Ti layer thickness is close to the sum of the Ti layer and two Ti_xGe alloy layers that

were found in the original core-shell structure, which indicates that the Ge in Ti_xGe alloy has been displaced from the original alloy layer and participated in the lithiation process. This implies that the Ti layer in the lithiated structure consists of the original Ti core as well as Ti from the Ge/Ti interfacial alloy coating to form a single Ti layer of increased thickness. At the same time, the lithiated Ge layer has expanded by 228% as expected for its lithiation.

Upon delithiation (0.01 V to 3.5 V), the Patterson function pattern peak heights initially decrease in magnitude at high z, which is likely due to the loss of coherence between the layers. The peaks gradually move to smaller heights as the

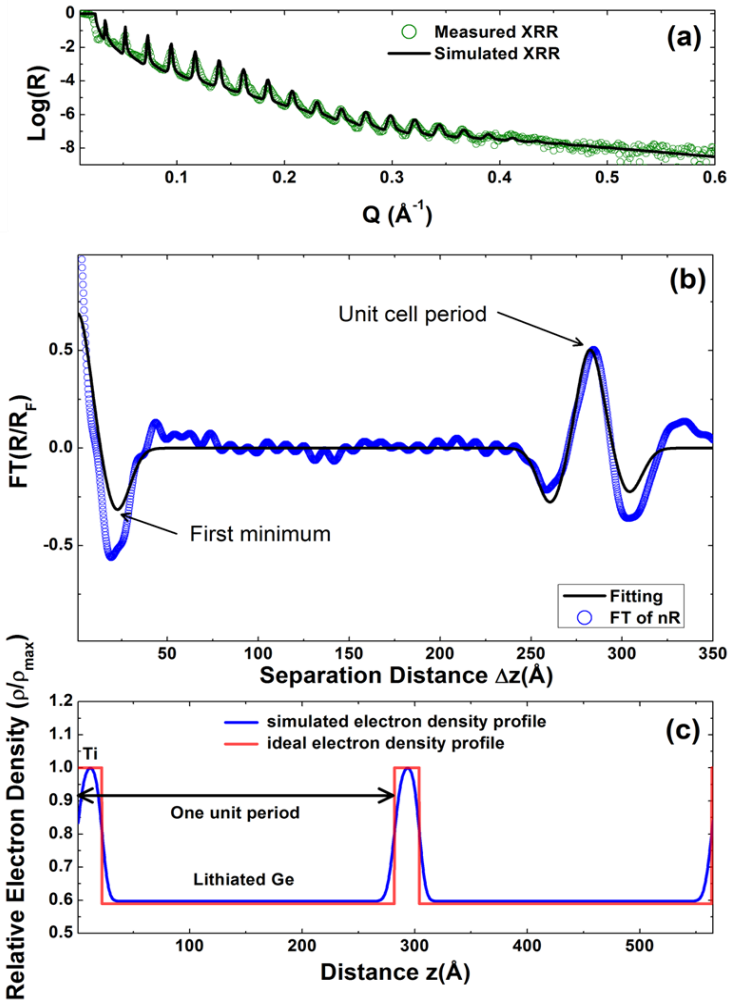

Figure 4.10 Patterson function analysis of the lithiated multilayer structure. (a) Specular X-ray Reflectivity data (green circle) of the and the calculated XRR signal (black line) using parameters obtained by fitting the observed Patterson function. (b) Calculated Patterson function (blue circle) and the model optimized Patterson function (black line). (c) Ideal model of electron density profile (red line) and optimized density profile obtained from Patterson function analysis (blue line).

potential is increased, and additional peaks appear in the Patterson functions as the applied potential approaches 1 V, where the Patterson function becomes sharper and more distinct. The re-appearance of features in the Patterson function at large separations z, indicates the recovery of coherence between the layers. We also find that the Patterson function reverts to the original seven-peak pattern towards the end of delithiation process, similar to that found for the as-deposited sample, revealing that Ge/Ti alloy observed for the as-deposited film reforms spontaneously upon delithiation. Model fitting of the Patterson function in the delithiated state (Figure 4.11) verifies this

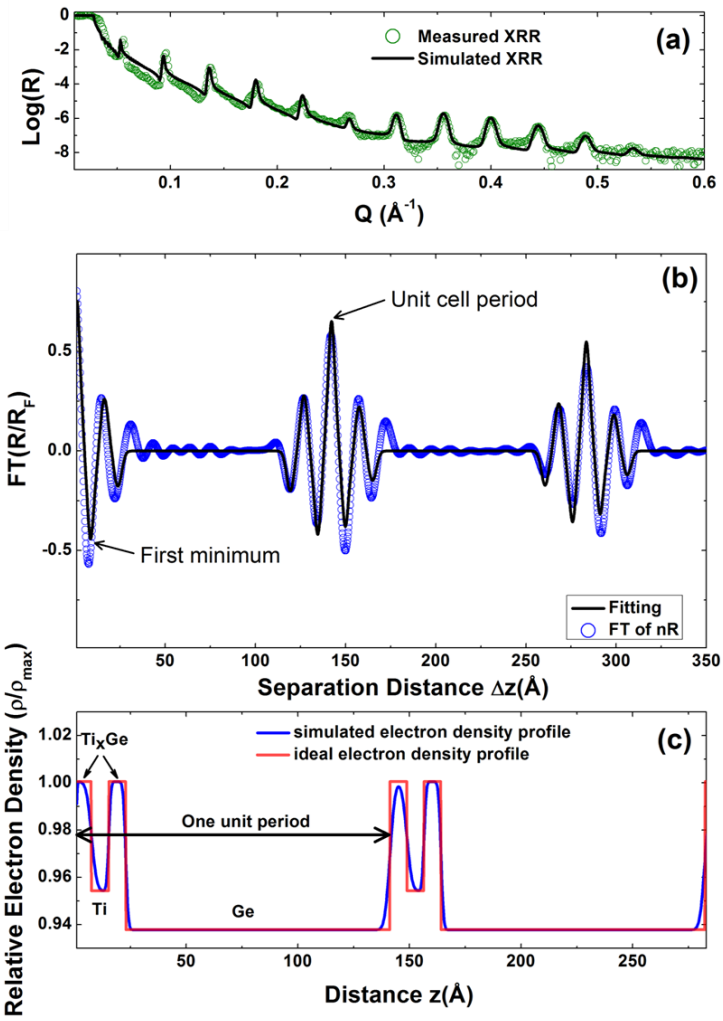

Figure 4.11 Patterson function analysis of the delithiated multilayer structure. (a) Specular X-ray reflectivity data (green circle) and the calculated XRR signal (black line) using parameters obtained by fitting the Patterson function. (b) Calculated Patterson function (blue circle) and its fitting curve (black line). (c) Ideal model of electron density profile (red line) and calculated electron density profile from Patterson Function (blue line).

structure with average thicknesses of 7.7 ± 0.1 Å for Ti, 118.3 ± 0.1 Å for Ge, and 7.6 ± 0.1 Å for the Ti_xGe alloy layer). The multilayer period of the delithiated structure is within 3% of the as-deposited structure even it had expanded by ~105% upon lithiation. This reveals that the multilayer structure provides a mechanism for high structural reversibility. These results are consistent with previous measurements using Si-based multilayers that revealed functional reversibility for more than 70 cycles)[146]. Compared with the original as-deposited state, the thicknesses of all layers have increased slightly, which is presumably due to an increase in porosity or trapped lithium within the layers.

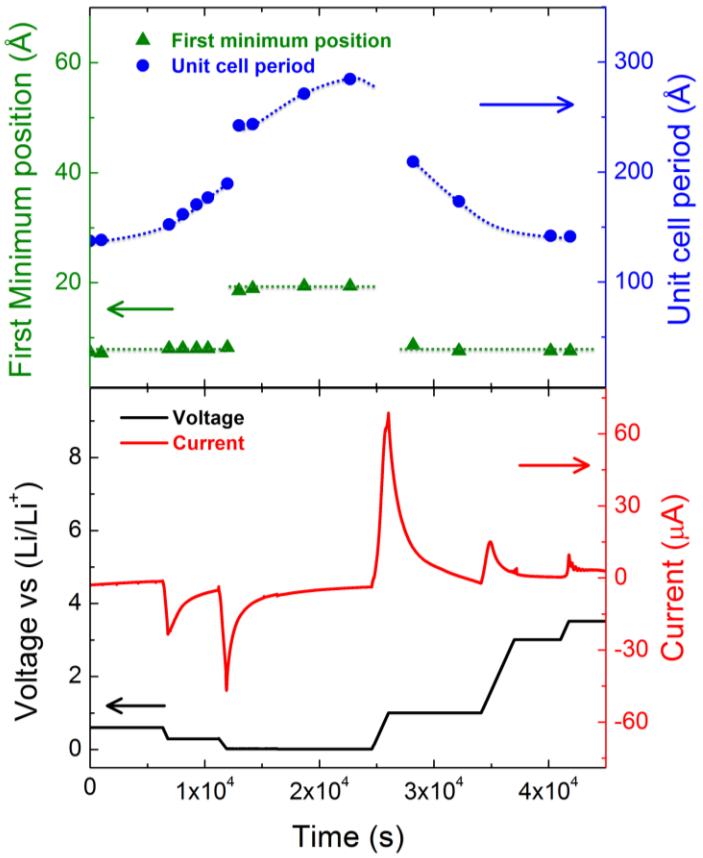

Figure 4.12 Time evolution of the applied voltage (black line) and the *in operando* measurements of the current (red line), as well as associated structural changes derived from the Patterson function analysis, including first minimum (i.e. negative peak) position (green triangles) and the multilayer unit cell period (blue circles). Dotted lines in the top panel are drawn to guide the eye. The first minimum position is associated with the Ti layer thickness and the period of the Patterson function is related to the thickness of one period in multilayer system.

To better understanding the separate processes of the lithiation of the Ge layer and that of the Ti_xGe alloy, we show the systematic variation of two characteristic spacings found in the Patterson function as a function of applied potential (Figure 4.12). The first minimum position of the Patterson function (green triangle) corresponds to the thickness of thinnest layer, which is the central Ti layer in our multi-layer system while the period of the multilayer, which is observed as the maximum of the Patterson function (blue circle), indicates the unit cell thickness. As the applied potential drops from 0.6 V to 0.3 V, the unit cell thickness gradually increases while the thickness of Ti layer remains the same, suggesting lithiation of only the Ge layers. Upon decreasing the potential to 0.01 V, the thickness of the Ti layer changes to a value of triple the original thickness and then remains constant. At the same time, the thickness of unit cell also exhibits a small jump, but the Ge layer thickness keeps increasing continuously until it is fully lithiated. The delithiation process shows similar behavior. When the applied potential increases, the Ti layer thickness returns to its original value, while the unit cell thickness decreases gradually until it is fully delithiated. This result reveals that this multilayer structure undergoes two separate reactions. The lithiation and delithiation reactions of the Ge layers occur gradually below 0.6 V (and are presumably strongly influenced by lithium ion transport through the multilayer structure). In addition, the lithiation of the Ti_xGe alloy core,

$$Ti_xGe + Li \leftrightarrow Ti + Li_xGe$$

is a reversible reaction that occurs between 0.3 V and 0.01 V. This reaction is better characterized as a conversion reaction due to the need to phase segregate the Ti and Ge components.

The schematic depiction in Figure 4.13 illustrates the overall changes to the multilayer structure in the first lithiation cycle. Ti_xGe alloy layers are found in the unlithiated state. Then during lithiation, the Ti and Ge in these alloy layers phase segregate, with the Ti from the

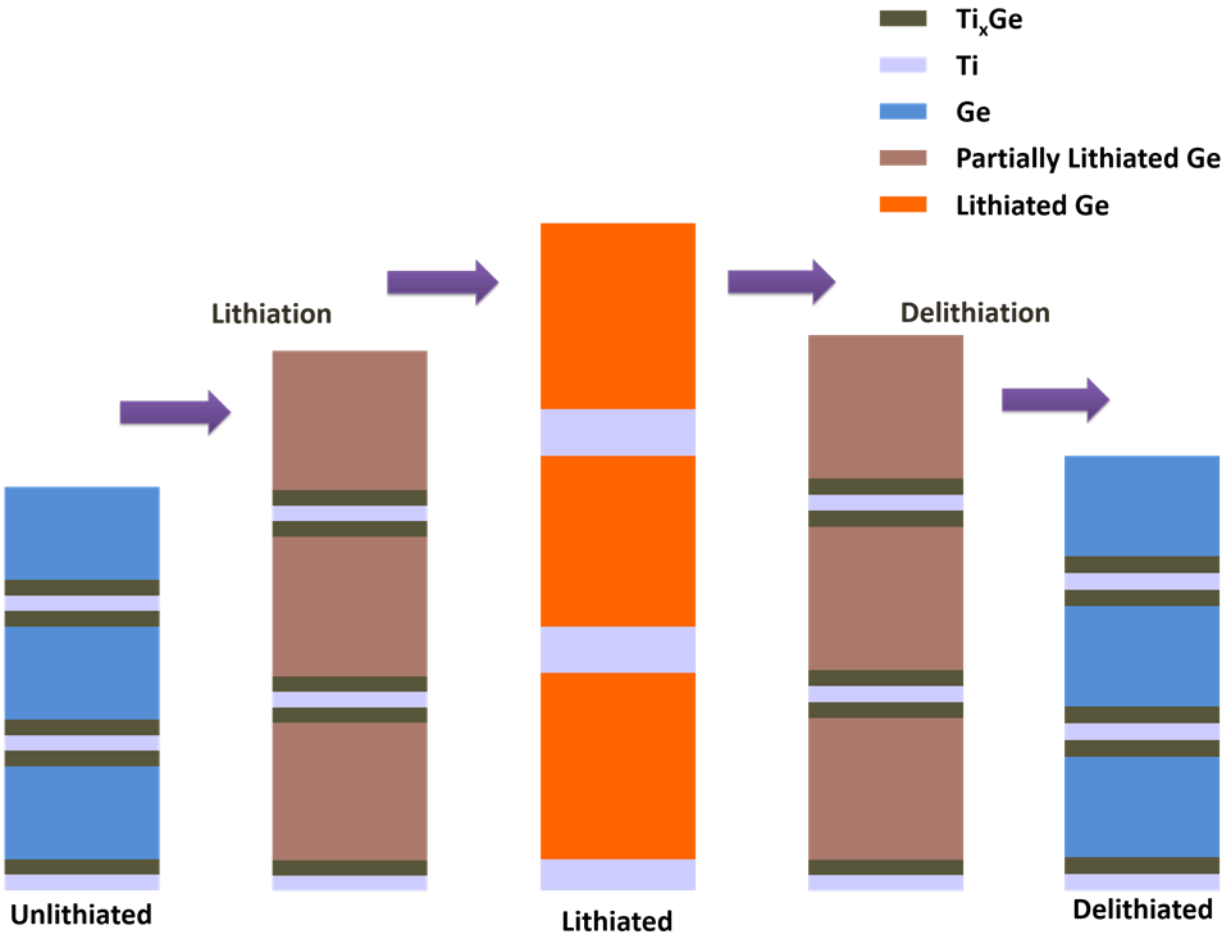

Figure 4.13 Schematic illustration of the structural changes that occur during lithiation and delithiation of the Ge/Ti multilayer structure.

surrounding alloy layers nucleating and growing at the Ti_xGe/Ti interface to form a thicker pure Ti layer, while the Ge in the alloy layers becomes lithiated along with the pure Ge layers. At this point, the lithiated multilayer structure consists of only 2 distinct layers per multilayer period: a Ti layer and a lithiated Ge layer. The reversibility of the reaction within the Ti_xGe alloy layer during delithiation is interesting, as it suggests that Ge diffuses into the Ti layer and re-forms a Ti_xGe alloy layer upon delithiation. This creates a hybrid electrode chemistry in which the lithiation of the Ge layers is a simple alloying reaction, while the lithiation of the Ti_xGe layers is a conversion reaction that leads to reversible phase segregation leading to Ti layers and lithiated Ge. From this observation, we infer that this central alloy layer exhibits multiple functionalities. It is active for lithiation as a conversion material, leading to a phase separation between the Ti and Ge, with the pre-existing Ti layers acting as a nucleation site for the phase segregation and contributing to a portion of the lithium capacity. It also acts as an adhesive that binds the Ge and Ti layers, preventing the working material from cracking or delaminating. Finally, the Ti layer acts as current collector, which ensures electrical conductivity within the multilayer structure.

extended electrochemical cycling: electrochemical stability of these multilayers were tested by lithiation/ delithiation cycling in a coin cell (CR2032, 20-mm diameter and 3.2-mm thick) with half-cell geometry (i.e., versus a lithium metal counter electrode). For these tests, the electrodes

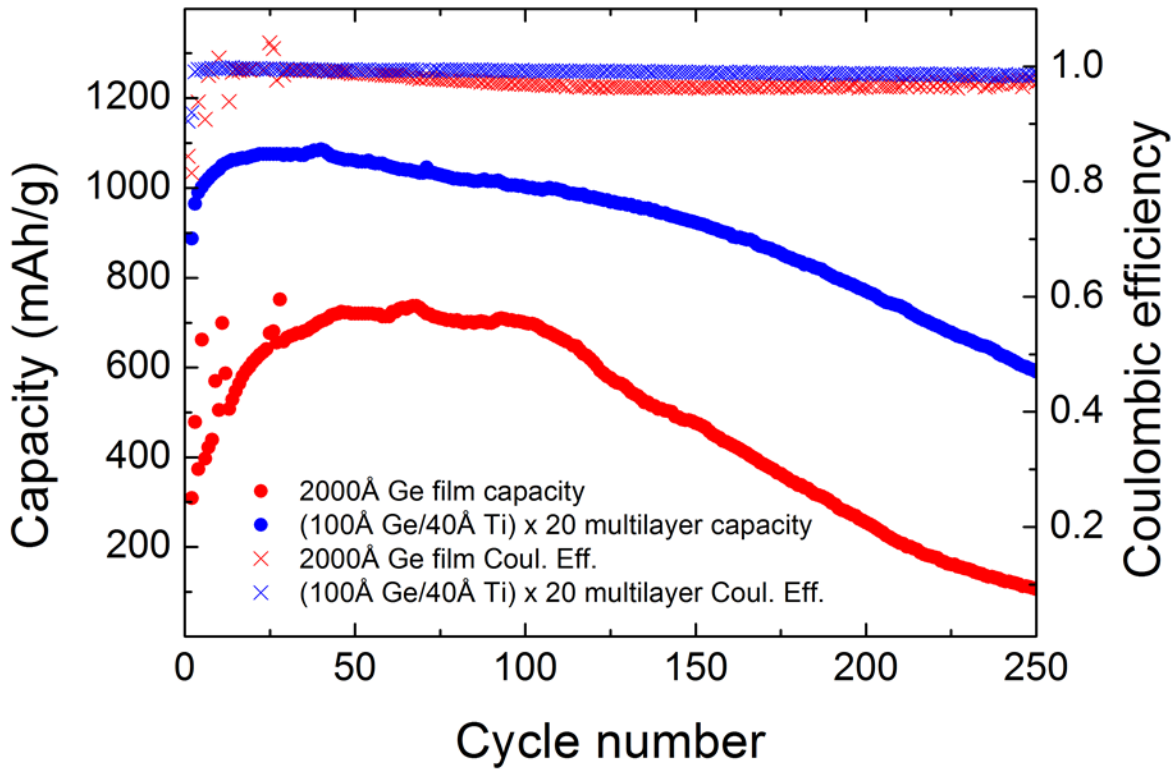

Figure 4.14 Galvanostatic cycling data for a Ge/Ti multilayer in a half-cell with a lithium anode, compared to a thin film with same overall Ge thickness grown on copper foil. (Solid circles indicate measured capacities and crosses indicate the associated Coulombic efficiency)

were deposited on copper foil. The performance of a multilayer having 20 periods of 100Å Ge and 40Å Ti layer thicknesses is compared to a thin Ge film with the same overall thickness (2000Å) (Figure 4.14). Galvanostatic cycling was performed between 3 V and 0.01 V with respect to Li/Li^+. The cycling rate was fixed at a current of 0.32mA corresponding to a 1C rate. Both electrodes show a trend of increasing capacity (calculated based on nominal mass of Ge) during the first ~20-50 initial cycles followed by a slow capacity loss. However, the measured capacity of the multilayer is ~30% higher than that of the Ge film (1100 mA/g vs. 750 mA/g, respectively) and

the multilayer capacity retention is substantially above that of the film after 250 charge cycles (600 mAh/g vs. 100 mAh/g, respectively). These results are consistent with the smaller Coulombic efficiency of the Ge thin film with respect to the multilayer and reveal that the multilayer architecture has superior electrochemical properties with respect to a comparable single layer Ge thin film.

4.4 Conclusion and discussion

Through the study of Ge/Ti multilayer thin film electrode system, we have gained useful knowledge both from the experiment results and the data analysis.

From the experiment aspect, we successfully demonstrated that the multilayer architecture can effectively address the capacity fading issues of Ge which results from the dramatic (up to 2.3-fold) volume changes during the lithiation/delithiation cycles. Moreover, with the introducing of Ti metal as the interlayer current collector, we found it more functional than expected. Due to the reversible conversion reactions of Ti_xGe alloy which naturally forms at the interface between Ge and Ti, Ti/Ge multilayer exhibits high structural reversibility during lithiation/delithiation cycles, and thus alleviates the capacity fading. Ti (with the forming of Ti_xGe alloy), acting like an elastic adhesive, helps to holds the whole morphology and prevent active Ge from cracking, delamination or pulverization. This provides more insight into the way of anodes synthesis, especially for those

undergoing large morphology variations during cycling. Additionally, the reversible conversion reaction of Ti_xGe itself is also worth further study to explore more materials with similar property.

From the data analysis aspect, we developed a method to quickly estimate the thickness of each layers in a multilayer system based on the Patterson function theory. If deeper and more precise analysis is need, the estimated thicknesses can be used to build the preliminary model, based on which Patterson function is directly fitted with the parameters we want to know. Comparing with the generally used model-dependent fitting of X-ray reflectivity, the Patterson function analysis can directly reveal approximate thicknesses of each layers by just a simple Fourier transformation. This method is especially good for in situ (operando) measurements which focus on the continuous structure changes.

Chapter 5 : $LiMn_2O_4$ Epitaxial Thin Film Growth

In the background section, I discussed the advantages of LMO as a cathode material as well as its main drawback, the server capacity fading. Lots of experiments and calculations have been done to understand the causes and try to find out solutions for this capacity fading [41, 42, 155], But electrochemistry is a quite complicated process, especially the reactions at electrode-electrolyte interface. The previous researches are mostly focused on bulk LMO which makes it even harder to observe and study the reactions at a specific interface. Therefore, an LMO electrode with well-defined surface and crystal structure with least other variables is needed for exploring the details of electrochemical process. Epitaxial thin film is one of the such experimental subjects that matches those requirements. In this chapter, we will introduce how to obtain a well-defined LMO epitaxial thin film with the ability to perform electrochemistry.

5.1 Growth conditions determination

In chapter 3.1, a few of physical vaper deposition techniques for thin film growth have been introduced. Among them, I have used sputtering and PLD for LMO deposition. If only considering depositing LMO single layer thin film, there isn't much difference between those 2 techniques. However, PLD is more general and has good capability for the deposition of most oxides. In case

we need more layers to deposit, I chose PLD as the main technique for the film deposition.

For a PLD deposition procedure, there are a few of parameters which can be optimized, such as substrate-target distance, laser energy density, pulse frequency, gas partial pressure and substrate temperature during deposition. Among them, the gas partial pressure and substrate temperature are most important since they can largely affect the phase and crystallinity of the film, respectively. Therefore, based on the deposition conditions reported by other researchers, we adjusted the O_2 partial pressure and substrate temperature to optimize the deposition. All the

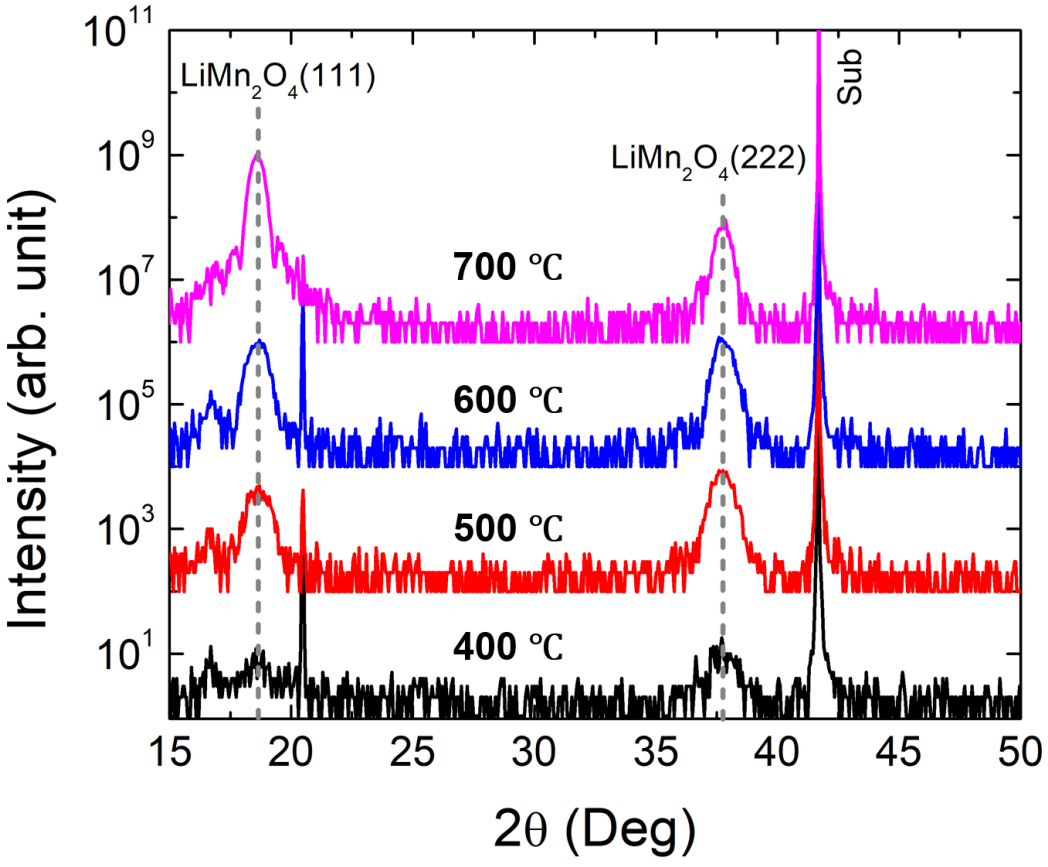

Figure 5.1 Specular XRD of LMO thin film deposited with different substrate temperatures by PLD.

depositions are performed using a KrF laser (248 nm) with a pulse duration and laser frequency set at 25 ns and 8 Hz respectively. The resulting energy of the laser beam was measured to be 100 mJ and focused on an area of 0.05 cm2 on the target surface (laser energy density of 2.0 J.cm-2). LMO target was held on a rotation stage at fixed distance (50 mm) from the substrate surface.

Figure 5.1 compares the specular X-ray diffraction of LMO thin film deposited with substrate temperature ranging from 400℃ to 700℃. The O_2 partial pressure was fixed to 50 mTorr. As we discussed in Chapter 3, the intensity and sharpness of the Bragg peak are related to the crystallinity and domain size of the film, respectively. When deposited at 400℃, LMO barely shows any Bragg peak, indicating a low crystallinity at this temperature. At 500 ℃, the LMO Bragg peaks become distinguishable. Then with the increase of substrate temperature during deposition, LMO Bragg peaks become sharper and more intense. At 700 ℃, the LMO(111) Bragg peak intensity is 3 order of magnitude higher than background. Moreover, the appearance of Kiessig fringes is a sign of higher film quality.

Figure 5.2 compares the specular X-ray diffraction of LMO thin film grown under different O_2 partial pressure. The substrate temperature is fixed at 700 ℃. Normally, the oxides are deposited in O_2 atmosphere to avoid oxygen loss, which may lead to the change of chemical state for cations and ultimately trigger phase transitions. When LMO was deposited without oxygen (0

mTorr O_2 partial pressure), an impure phase was found (referring to the peak at around 19.8°). 50 mTorr O_2 partial pressure gives out pure phase LMO with clear Kiessig fringes. When further increase the O_2 partial pressure to 200 mTorr, diffraction pattern still indicates pure LMO phase but with fewer Kiessig fringes which suggests lower film quality.

Based on the film properties under tweaked deposition condition, we found that the substrate temperature for growing crystallized LMO should be above 600 ℃ and O_2 partial pressure should be around 50 mTorr for best quality.

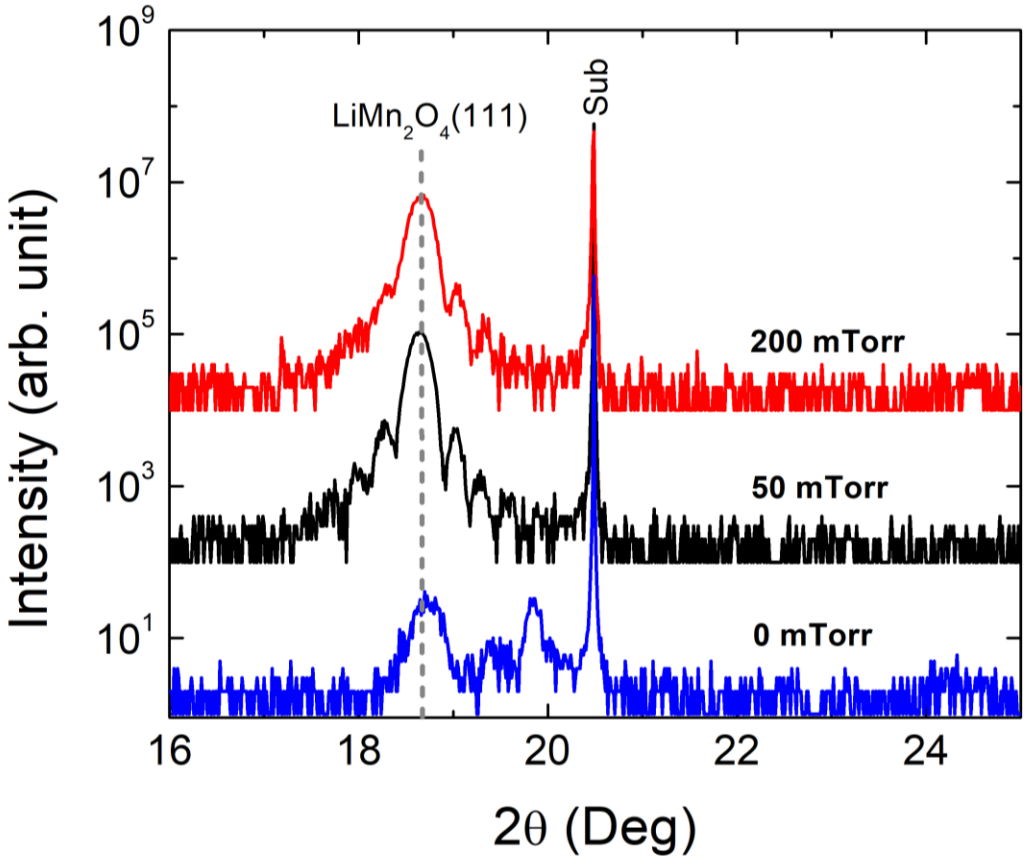

Figure 5.2 Specular XRD of LMO thin film deposited under different O_2 partial pressure

5.2 Substrate selection and in-plain alignment characterization

A common explanation for epitaxy is "a single crystal layer that grows with a particular orientation determined by the single crystal substrate". This definition does not require the film and substrate to be exactly lattice matched, but they must still be similar enough to interact and have a defined relationship.

As the substrates for LMO epitaxial thin film growth, there are 2 key requirements needs to be met. One is the in-plane lattice structure which shall accommodate the epitaxial relation to LMO (i.e. similar structure and close lattice constant). The other one is physically and chemically stability during the deposition of LMO and the electrochemical cycling afterward. Therefore, single crystal oxides with cubic crystal structure are firstly preferred. Besides that, the hexagonal (rhombohedral) oxides with (0001) orientated surface can also provide good epitaxy for the growth

Substrate	Lattice mismatch	LMO orientation	Thickness (Å)	Roughness (Å)
MgO (001)	2.2% (2:1)	(001)	152	23.2
Al_2O_3 (0001)	2.1% (5:2)	(111)	147	5.4
$MgAl_2O_4$ (001)	-1.9% (1:1)	(001) & (111)	---	---
$SrTiO_3$ (001)	-5.2% (2:1)	(001)	122	28.2
$SrTiO_3$ (111)	-5.2% (2:1)	(111)	109	2.5
$LaAlO_3$ (001)	-7.8% (2:1)	(001) & (111)	---	---

Table 5.1 Substrates candidates (first column) for LMO single layer growth and their in-plane lattice mismatch (second column). Third to fifth columns are orientations, thicknesses and roughnesses of LMO thin films on related substrates, respectively. They are obtained from the fitting of XRR data.

of (111) oriented LMO. After comprehensive consideration, MgO, $SrTiO_3$, $LaAlO_3$ and $MgAl_2O_4$ with cubic structure as well as Al_2O_3 with hexagonal structure were chosen as possible candidates for LMO growth.

Table 5.1 column 2 shows the in-plane lattice mismatch for each substrate with respect to LMO (111) plane [156]. Starting from MgO to $LaAlO_3$, the substrate lattice constants generally decrease and provide a tensile (positive) to compressive (negative) stress. During the deposition, substrates were fixed to a resistive heater using silver paint and heated to 650 °C with temperature controlled to ±5 °C and monitored with thermocouple embedded within the heating block. A base pressure of $5x10^{-5}$ Torr ($6.67x10^{-3}$ Pa) was maintained and the background oxygen pressure was set at 50 mTorr (6.6 Pa). The targets were pre-ablated with 300 pulses before each deposition to remove any surface impurities and then expose the plume to substrates for 240 pulses.

The last 3 columns in Table 5.1 present the information about the prepared LMO thin film orientation, thickness and roughness. MgO has a cubic crystal structure with space group Fm-3m. Its lattice constant (a = 4.231Å) is about half as to LMO (a = 8.240Å) with 2.2% mismatch. The LMO thin film deposited on MgO (001) adopts (001) orientation (cube-on-cube growth) with 152Å thickness and 23.2Å roughness. Al_2O_3 has a rhombohedral crystal structure with space group R-3c. In the conventional hexagonal cell, the (0001) plane adopts hexagonal structure which is

same as the (111) plane of LMO. If converted into hexagonal cell, the lattice constant of LMO (111) plane (a = 8.240 / $\sqrt{2}$ = 5.827Å) matches Al_2O_3 (0001) plane (a = 4.759Å) with an integer ratio (5:4) and 2.1% mismatch. The deposition result also shows that LMO adopts (111) orientation on Al_2O_3(0001) substrates with 147Å thickness and 5.4Å roughness. $MgAl_2O_4$, in principle, has the closest lattice spacing to LMO. Both of them have spinel crystal structure with only -1.9% lattice mismatch. However, the LMO thin film deposited on the top of $MgAl_2O_4$ (001) shows split orientations with (001) and (111). $SrTiO_3$ has a cubic structure with space group Pm-3m. Its lattice constant (a = 3.905Å) is half as to LMO with -5.2% mismatch. The LMO thin films deposited on both (001) and (111) orientated $SrTiO_3$ fully adopt the orientations of the corresponding substrates. The thickness and roughness of LMO are 122Å and 28.2Å on $SrTiO_3$(001) and 109Å and 2.5Å on $SrTiO_3$(111), respectively. The last substrate that we tried was $LaAlO_3$. It has the rhombohedral crystal structure with space group R-3c at room temperature, which transforms into ideal cubic structure with space group Pm-3m at 550℃. Since LMO was deposited at 650℃, we expected a cube-on-cube growth of LMO on the top of $LaAlO_3$(001). However, mixed orientations were observed. After careful investigation, we found the $LaAlO_3$ substrate itself was divided by different oriented domains which may result from the rhombohedral-cubic structure transition.

The deposition result in Table 5.1 shows that MgO, Al_2O_3 and $SrTiO_3$ are suitable substrates for single layer LMO epitaxial thin film growth. Moreover, it also suggests that (111) oriented LMO thin film are generally smoother than (001) orientated LMO thin film. The (001) orientated LMO thin films are cube-on-cube grown on the top of MgO(001) and $SrTiO_3$(001) and in-plane aligned with substrates lattice. However, the (111) orientated LMO thin films may present different

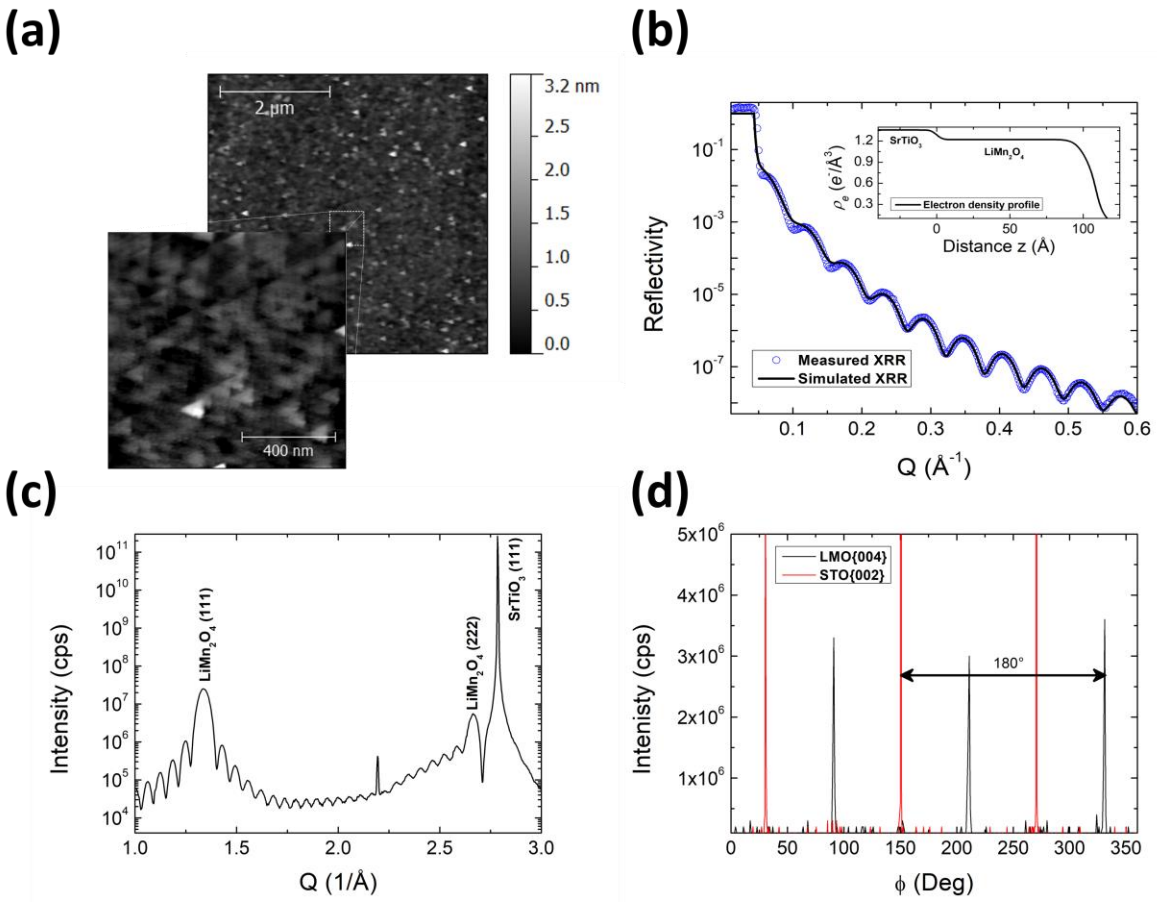

Figure 5.3 Characterizations of $LiMn_2O_4$ single layer thin film on $SrTiO_3$(111) substrates. (a) AFM image for surface morphology. (b) XRR with measured data (blue circle) and fitted curve (black line). Insert is the electron density profile based on the fitting results. (c) Specular X-ray diffraction which shows the Bragg peaks of LMO and substrates along surface normal direction. (d) Azimuthal phi-scans for off-specular LMO {004} and $SrTiO_3$ {002} Bragg peak families.

in-plane alignments as to the substrates. Therefore, we performed further investigation on LMO(111) thin films which are deposited both on $SrTiO_3$(111) and Al_2O_3 (0001).

Figure 5.3 shows a thorough characterization of a LMO thin film deposited on the top of $SrTiO_3$(111) substrate. When deposited on $SrTiO_3$(111), LMO(111) has 2 possible ways for in-plane alignment (as shown in Figure 5.4) . One is "twinned" growth which adopts a mirror structure of substrate with respect to the interface (Figure 5.4 left). The other one is "extended" growth which totally duplicates the substrate lattice structure and in-plane orientation (Figure 5.4 right). The difference between twinned and extended growth can also be illustrated through close-packing stacking consequence. Oxygens in LMO and SrO_3 in $SrTiO_3$ form cubic close-packing with consequence -ABCABC. When LMO is twinned grown, the close-packing stack consequence for

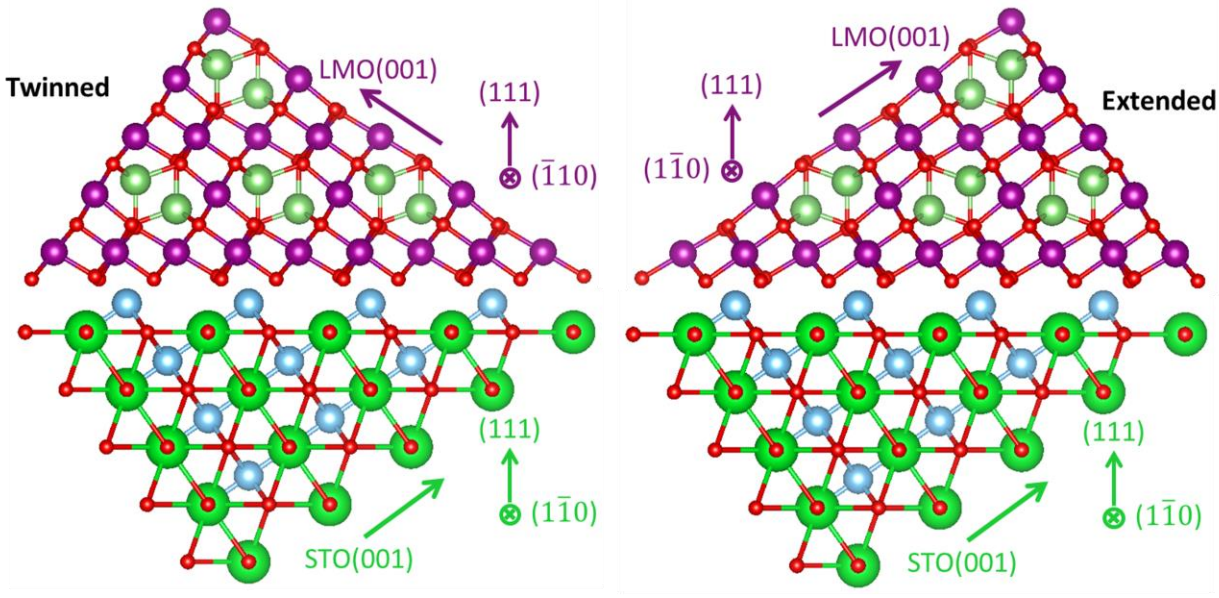

Figure 5.4 Schematic illustration for in-plane alignment of twinned growth (left) and extended growth (right).

whole system can be described as -ABCAB-C-BACBA-, where C is the interface layer, and thus forms a mirror symmetry. While if LMO is extended grown, the close-packing stack consequence will be described as -ABCABC-ABCABC-, where oxygen close-packing in LMO duplicate the stack consequence of SrO_3 in $SrTiO_3$.

Figure 5.3(a) shows an AFM image of LMO(111) thin film surface morphology on $SrTiO_3$(111) substrate. From the zoom-in image, we can clearly observe the triangular shape of domains which are all orientated in the same direction. This directly indicates that LMO thin film only adopts one growth geometry, either "twinned" or "extended". Figure 5.3(b) is the XRR characterization which reveals electron density profile of LMO thin film along [111] direction (Figure 5.3(b) insert). The thin films' thickness and roughness in Table 5.1 also come from the analysis of this characterization. Figure 5.3(c) shows the specular X-ray diffraction. The clear and unique presence of LMO (111) and LMO (222) Bragg peak suggests that the film is well orientated along surface normal. The Kiessig fringes between Bragg peaks indicate a high quality of the film. However, due the same projection of atoms distribution perpendicular to [111] direction, specular X-ray diffraction can't distinguish the 2 different in-plane alignments. Therefore, we performed azimuthal phi-scans at LMO {004} and substrate $SrTiO_3$ {002} off-specular Bragg peak families which are shown in Figure 5.3(d). The azimuthal phi-scan of LMO {004} only shows a set of 3

peaks which indicates a single in-plane orientation that matches the observation form AFM image. Comparing with the azimuthal phi-scan of substrate $SrTiO_3$ {002}, there is a 180° difference between them. From the schematic illustration of 2 different growth paths (Figure 5.4), it can be easily understood that the azimuthal phi-scan of LMO {004} with twinned growth will have 180° difference from the azimuthal phi-scan of $SrTiO_3$ {002}, otherwise they will overlap if LMO is

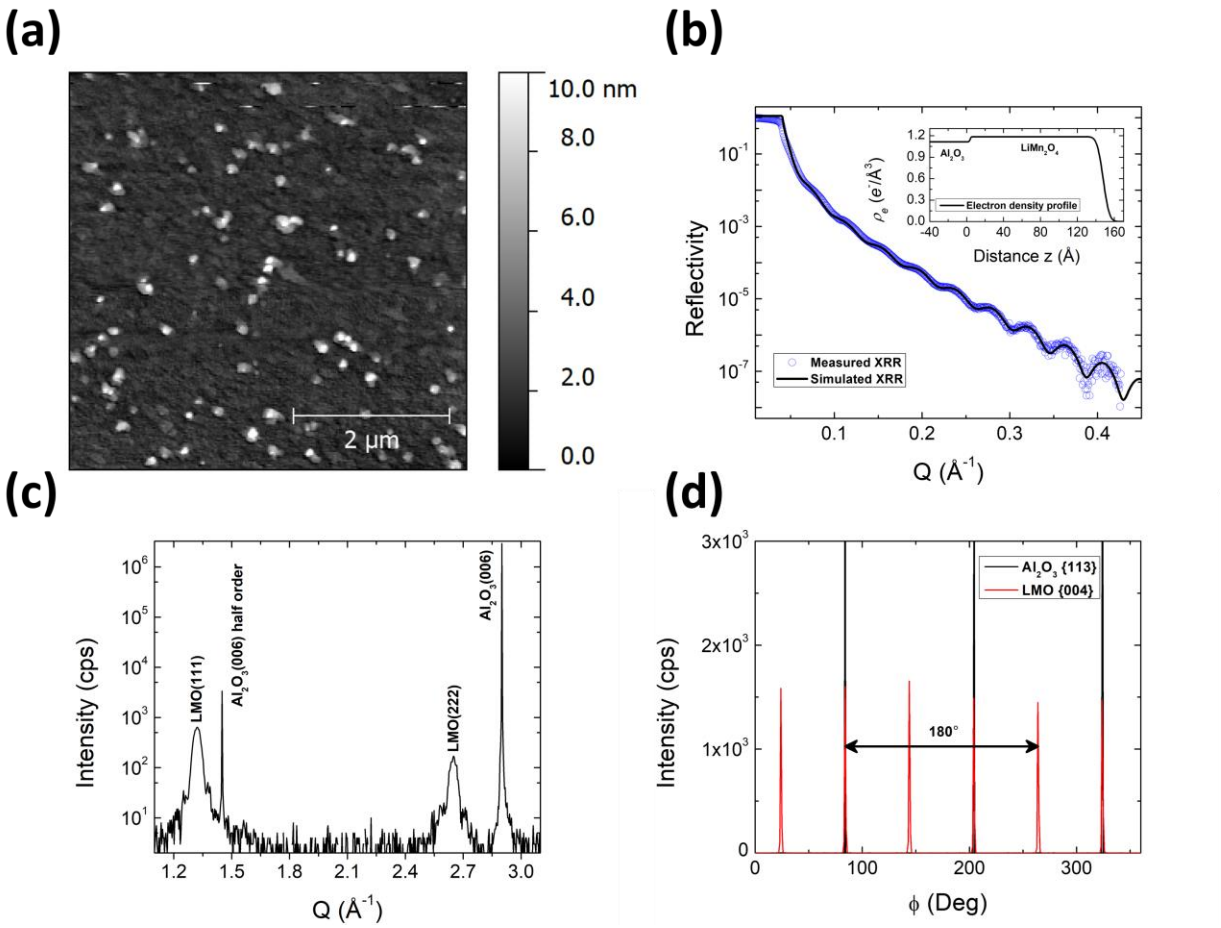

Figure 5.5 Characterizations of $LiMn_2O_4$ single layer thin film on Al_2O_3(0001) substrates. (a) AFM image for surface morphology. (b) XRR with measured data (blue circle) and fitted curve (black line). Insert is the electron density profile based on the fitting results. (c) Specular X-ray diffraction which shows the Bragg peaks of LMO and substrates along surface normal direction. (d) Azimuthal phi-scans for off-specular LMO {004} and Al_2O_3 {113} Bragg peak families.

grown following “extended” way. Combining all the characterization results, we can conclude that LMO thin film is twinned grown on the top of $SrTiO_3$ (111).

Similar characterizations are also performed on the LMO(111) thin film deposited on Al_2O_3(0001) substrate (as shown in Figure 5.5). Figure 5.5(a) shows the surface morphology of the film imaged by AFM. The color bar legend suggests a rougher surface, comparing to LMO on $SrTiO_3$(111). XRR in Figure 5.5(b) verified the result from AFM image. Specular X-ray diffraction (Figure 5.5(c)) shows LMO (111) and (222) Bragg peaks only, indicating a single orientation along surface normal. The in-plane lattice alignment is investigated through azimuthal phi-scans of LMO {004} and Al_2O_3 {113} off-specular Bragg peak families which are shown in Figure 5.5(d). Unlike the growth on cubic $SrTiO_3$, the hetero-epitaxial growth of cubic LMO on hexagonal Al_2O_3 may present 2 in-plane alignment modes (noted as A-mode and B-mode) with 2 different domains in each mode[157]. The A-mode is defined as the mode in which both in-plane fundamental axes are parallel (i.e. LMO$[10\bar{1}]$ // $A_2O_3[10\bar{1}0]$). While the B-mode entails no parallel axes. The 2 different modes have a 30° in-plane rotation difference and the 2 different domains in each mode have a 180° in-plane rotation difference. The azimuthal phi-scan of LMO {004} shows 6 peaks which are 2 sets of 3 peaks with 180° in-plane rotation difference. This indicates that LMO thin film is grown with two domains (noted as domain I and domain II) that belongs to the same mode. Since one set

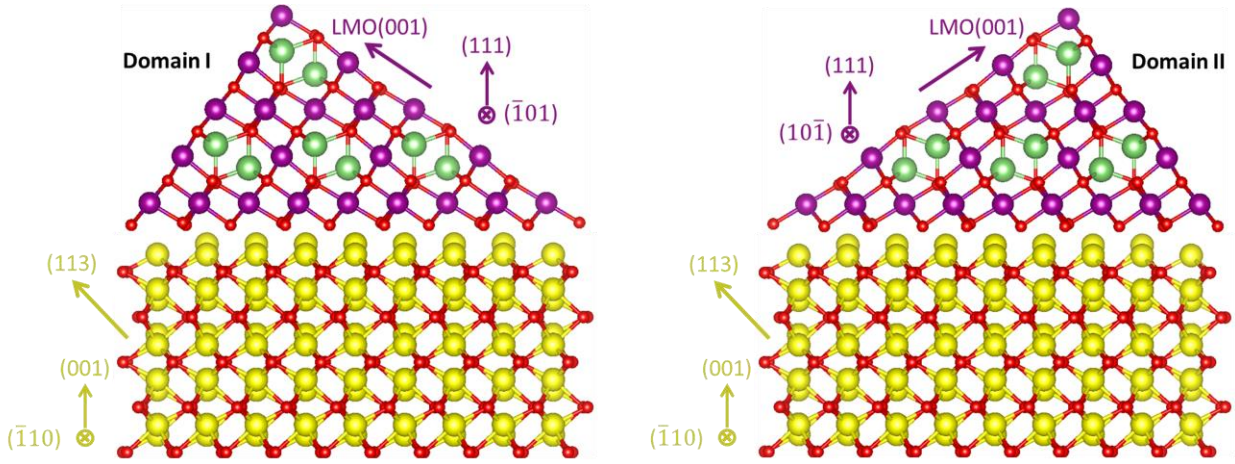

Figure 5.6 Schematic illustration for in-plane alignments of domain I and domain II in A-mode.

of LMO {004} Bragg peak is overlapped with Al_2O_3 {113} Bragg peak, the LMO thin film follows A-mode growth. Figure 5.6 schematically illustrate how LMO epitaxial thin film is aligned on the top of Al_2O_3(0001) substrate. Since the oxygen in Al_2O_3 is hexagonal close-packed with consequence -ABAB, the domain I and domain II can be described with stacking consequence -ABAB-ABCABC- and -ABAB-ACBACB-, respectively.

5.3 Conducting buffer layer seeking and selection

In last section, we successfully prepared LMO thin film with high quality and well-defined orientation. However, the single layer of LMO epitaxial thin film is not good for electrochemical study by itself due to its low electrical conductivity (1.9×10^{-3} S/m)[158]. Thus, either a conducting substrate or a conducting buffer layer is needed to be introduced as current collector. For conducting substrates, metals are apparently the most straight forward ones. But they are hard to provide good epitaxy for LMO due the hetero crystal structures. On the other hand, among

conducting oxide substrates, Nb:$SrTiO_3$ is the most promising one as it has a cubic crystal structure with close lattice constant as to LMO. However, Nb:$SrTiO_3$ is n-type doping with electrons as major carrier, hence can easily loose conductivity[159] during the deposition of LMO which is under relatively high O_2 pressure. As the direct way of using a conducting substrate can't be achieved, the conducting buffer layer method is taken into consideration.

Besides the requirement for high conductivity, this buffer layer should also maintain the epitaxy between substrate and LMO thin film. Therefore, we proposed several candidates (TiN, Al:ZnO, $La_{0.5}Sr_{0.5}CoO_3$ and $SrRuO_3$) based on the substrates selected in previous section (i.e. MgO, Al_2O_3 and $SrTiO_3$) and investigated their properties as a conducting buffer layer. Table 5.2 summarized the deposition results of buffer layers. Since the growth of those buffer layers on the corresponding substrates have been well studied [160-163], their epitaxy and film qualities are mostly guaranteed. The only difference is the ability to keep their properties after LMO being deposited on the top.

Table 5.2 Buffer layer candidates (first column) with related substrates (second column) and shown orientations (third column). The last column shows the properties for each buffer layer after the deposition of LMO on the top.

Buffer layer	Substrate	Buffer layer orientation	Property with $LiMn_2O_4$
TiN	MgO (001)	(001)	The deposition of $LiMn_2O_4$ largely decreases the conductivity of buffer layer.
	Al_2O_3 (0001)	(111)	
Al:ZnO	Al_2O_3 (0001)	(0001)	The deposition of $LiMn_2O_4$ largely decreases the conductivity of buffer layer.
$La_{0.5}Sr_{0.5}CoO_3$	$SrTiO_3$ (111)	(111)	Electrochemically reactive in the $LiMn_2O_4$ cycling voltage window.
$SrRuO_3$	$SrTiO_3$ (001)	(001)	$LiMn_2O_4$ presents (111) orientation.
	$SrTiO_3$ (111)	(111)	Well orientated $LiMn_2O_4$ (111) thin film is grown on the top with relatively smooth surface.

TiN is metallic conducting (3.7×10^6 S/m) and has well-established thin film preparing procedures using reactive DC sputtering deposition[164]. The MgO and Al_2O_3 substrates were fixed to a resistive heater using silver paint and heated to 700 °C. Ti metal target was held 100 mm away from the surface of the substrates. During the deposition, the vacuum chamber maintained the total pressure at 3.6 mTorr (0.48 Pa) with Ar and N_2 flow rates at 30 sccm and 7 sccm respectively. The DC power was set to 200 mA with 45 minutes deposition time. Since TiN has the same crystal structure (Fm-3m) and very close lattice constant (a = 4.242Å) with respect to MgO, this growth

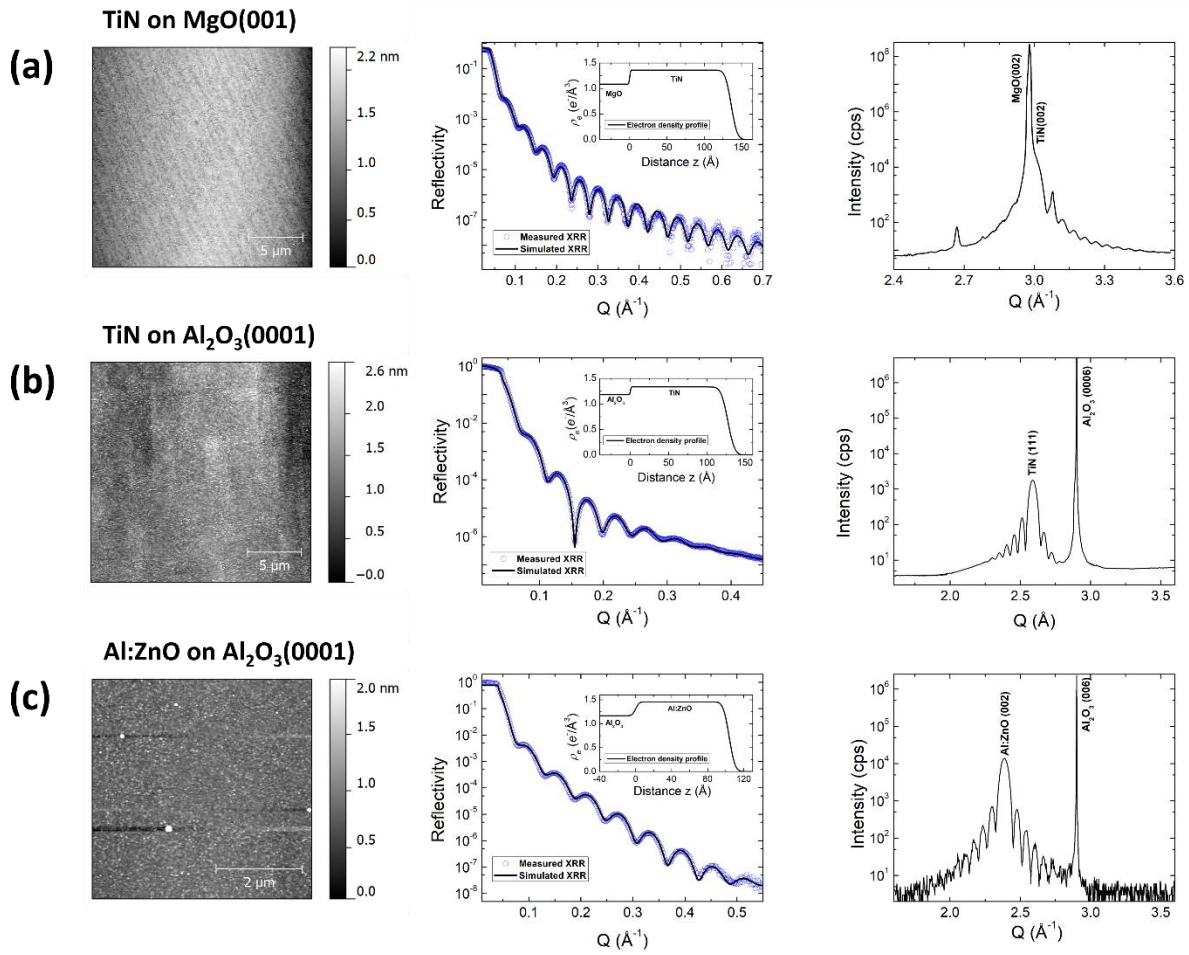

Figure 5.7 AFM (left), XRR (middle) and specular X-ray diffraction characterizations for (a) TiN deposited on MgO(111), (b)TiN on Al_2O_3(0001) and (c) Al:ZnO on Al_2O_3(0001). In XRR characterization, blue circles are measure data points and black line is fitted result. The inserts are electron density based on the fitting results.

follows “cube-on-cube” alignment which completely maintains the crystal structure of MgO. Figure 5.7(a) shows the characterization results of TiN thin film on MgO(001). The left figure is the AFM image of the film surface. The obvious terrace indicates a very smooth surface. The thickness and roughness obtained through the fitting of low angle XR (middle) are 136.2 Å and 3.5Å, respectively. Specular X-ray diffraction (right) shows overlapped MgO (002) and TiN (002) Bragg peaks with a few Kiessig fringes, indicating pure orientation and good film quality. The same characterizations (Figure 5.7(b)) have been done on TiN thin film deposited on Al_2O_3(0001). Similar to the LMO on Al_2O_3(0001), this hetero-epitaxial growth leads to (111) oriented TiN epitaxial thin film with 127.5 Å thickness and 7.2 Å roughness. In general, TiN thin films on both MgO(001) and Al_2O_3(0001) have maintained the expected epitaxy and smooth surface which is suitable for the epitaxial growth of high quality LMO thin film on the top. However, we found that TiN buffer layer totally lost its conductivity after the deposition of LMO. A further investigation reveals that TiN was oxidized during the LMO deposition.

Al doped ZnO (Al:ZnO) is a well know transparent conducting oxide with conductivity ~1.3×10^5 S/m (depends on doping rate) [165]. Since ZnO can maintain good epitaxy on the top of Al_2O_3(0001)[166], we made an attempt to grow Al:ZnO epitaxial thin film on Al_2O_3(0001) substrate. The film was prepared by PLD. Substrate temperature was set to 750 °C and O_2 pressure was kept at 0.4 mTorr (0.05Pa). 2 targets, ZnO and Al_2O_3, were used with 160:1 pulse hitting ratio. Total pulses hit on ZnO target and Al_2O_3 target were 1920 and 12, respectively. Film characterizations are shown in Figure 5.7(c). Al:ZnO thin film is well oriented following the substrate’s orientation with 103.9 Å thickness and 5.2 Å roughness. The high conductivity, good film quality and well-maintained epitaxy on Al_2O_3(0001) make it a good buffer layer choice. However, similar to TiN, Al:ZnO also lost its conductivity after the deposition of LMO. The reason maybe same as that for

Nb:$SrTiO_3$. Since both of them are n-type doped, electrons are the main carrier. Then their conductivity is highly affected by oxygen pressure during LMO deposition.

In order to avoid the oxidation and loss of conductivity upon LMO deposition, we limited our buffer layer seeking area into p-type conducting oxides. After taking the epitaxy into account, 2 possible materials are proposed, which are $La_{0.5}Sr_{0.5}CoO_3$ (LSCO) and $SrRuO_3$. Both of them are with perovskite crystal structure which is essentially same as $SrTiO_3$.

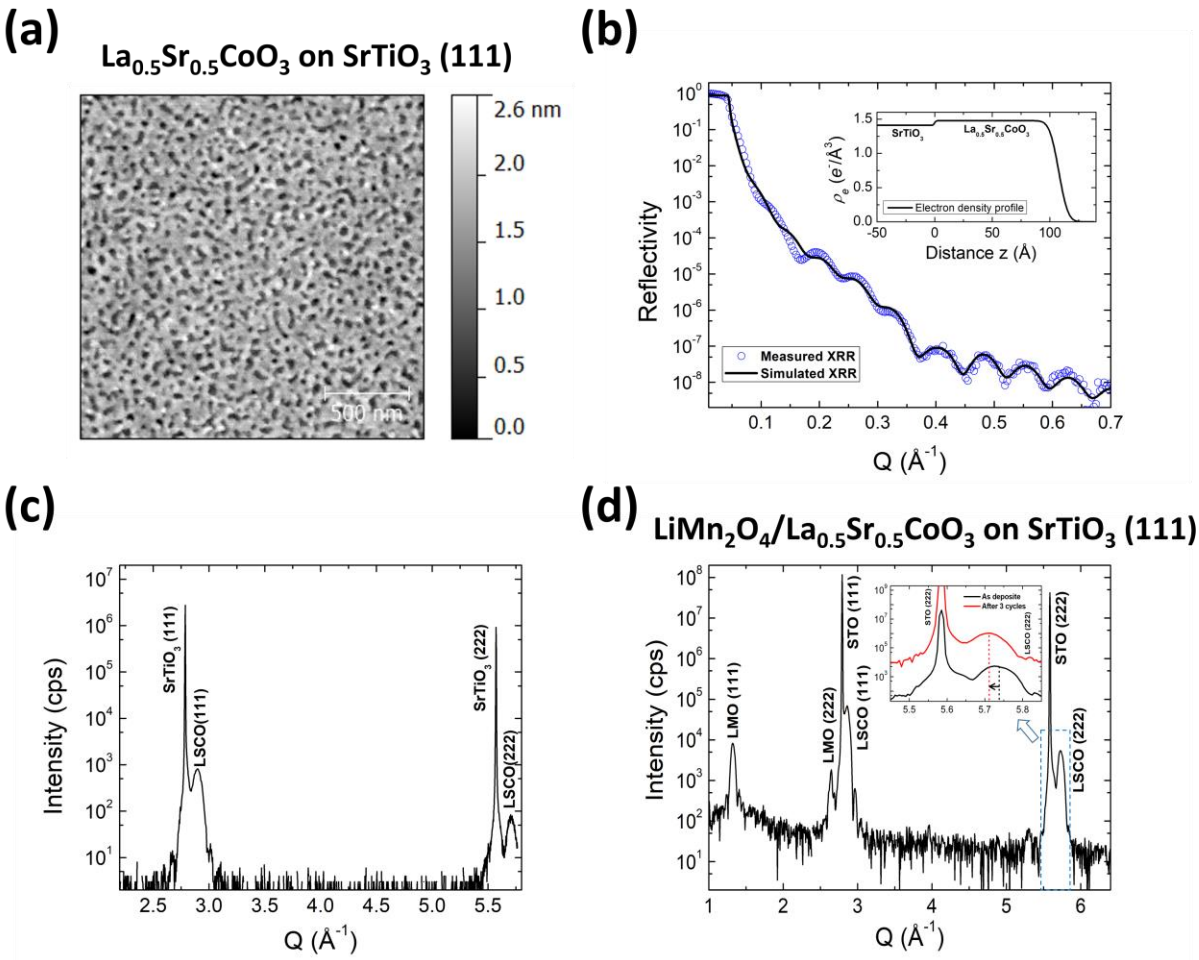

Figure 5.8 Characterizations of LSCO thin film on $SrTiO_3$(111) substrates. (a) AFM image for surface morphology. (b) XRR with measured data (blue circle) and fitted curve (black line). Insert is the electron density profile based on the fitting results. (c) Specular X-ray diffraction which shows the Bragg peaks of LSCO and substrates along surface normal direction. (d) Specular X-ray diffraction for LMO/LSCO bilayer thin film on $SrTiO_3$(111). Insert is the comparing of LSCO (222) Bragg peak before and after electrochemical cycling.

LSCO thin film was prepared by PLD with 650 ℃ substrate temperature, 300 mTorr (40 Pa) O_2 pressure and 300 pulses. Figure 5.8(a)-(c) are the characterizations for LSCO thin film deposited on $SrTiO_3$(111) substrate. The AFM image (Figure 5.8(a)) shows a mosaic-like surface with 5.2 Å average roughness. Analysis of XRR (Figure 5.8(b)) reveals the film thickness to be 107.7 Å and surface roughness to be 6.3 Å which is close to the AFM result. Specular X-ray diffraction (Figure 5.8(c)) verified the epitaxy in which LSCO thin film totally adopted the orientation of $SrTiO_3$(111) substrate. Then we deposited LMO on the top of LSCO using the same condition for LMO single layer deposition. After the deposition of LMO, LSCO still preserved its conductivity. The specular X-ray diffraction for LMO/LSCO bilayer thin film deposited on SrTiO3(111) is shown in Figure 5.8(d). Same as solely grown on $SrTiO_3$(111), LMO adopted (111) orientation without any other phase shown. The electrochemical test on this bilayer system lead to an abnormal cyclic voltammetry (CV) curve which was much different from the reported CV for pure LMO. After carefully comparing, we find that the Bragg peaks of LSCO have also shifted during cycling (as shown in Figure 5.8(d) insert) which indicates that LSCO also undergoes reactions during electrochemical cycling. Further details about the reactions that occur on LSCO are being studied by Xiankai Yu, one of my collaborators.

$SrRuO_3$ thin films were prepared by PLD on both $SrTiO_3$(001) and $SrTiO_3$(111) substrates. Substrates temperature was set to 650 ℃ during deposition. Vacuum chamber maintained 50 mTorr (6.6 Pa) oxygen pressure and 240 pulses were hit on $SrRuO_3$ target for deposition. The characterization results for $SrRuO_3$ deposited on $SrTiO_3$(001) were shown in Figure 5.9. The AFM image (Figure 5.9(a)) shows a smooth and terrace-like surface. Fitting results from low angle XR (Figure 5.9(b)) suggest the thickness and roughness are 99.0 Å and 4.5 Å, respectively. XR in the CTR regime (Figure 5.9(c)) shows perfect cube-on-cube orientation with clear Kiessig fringes

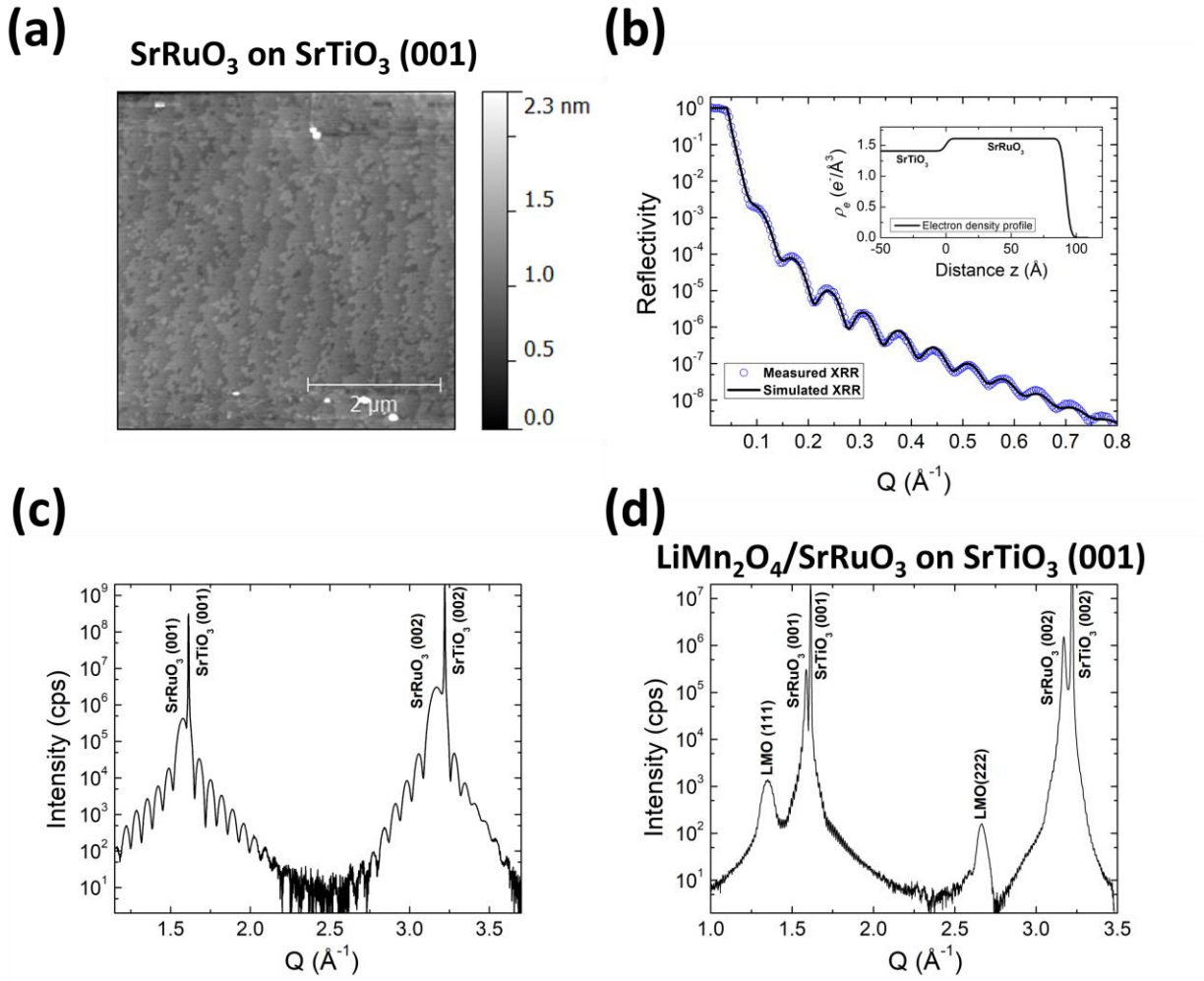

Figure 5.9 Characterizations of $SrRuO_3$ thin film on $SrTiO_3$(001) substrates. (a) AFM image for surface morphology. (b) XRR with measured data (blue circle) and fitted curve (black line). Insert is the electron density profile based on the fitting results. (c) Specular X-ray diffraction which shows the Bragg peaks of $SrRuO_3$ and substrates along surface normal direction. (d) Specular X-ray diffraction regime for LMO/$SrRuO_3$ bilayer thin film on $SrTiO_3$(001) which shows (111) orientated LMO.

between film Bragg peaks. After the deposition of LMO on $SrRuO_3$, the whole system still kept its high conductivity. However, LMO thin film presented (111) orientation instead of expected (001) orientation under the assumption of cubic-on-cubic growth (as shown in Figure 5.9(d)).

Comparable characterizations were also performed on $SrRuO_3$ deposited on $SrTiO_3$(111)

(as shown in Figure 5.10). The AFM image (Figure 5.10(a)) indicates a mosaic-like surface with 5.0 Å average roughness. The thickness and roughness obtained from XRR (Figure 5.10(b)) are 91.9 Å and 5.4 Å respectively, which is close to the result from AFM analysis. Only (111) orientated $SrRuO_3$ are shown in specular X-ray diffraction (Figure 5.10(c)), indicating a good epitaxy persistence. The deposition of LMO didn't affect the conductivity of the whole system.

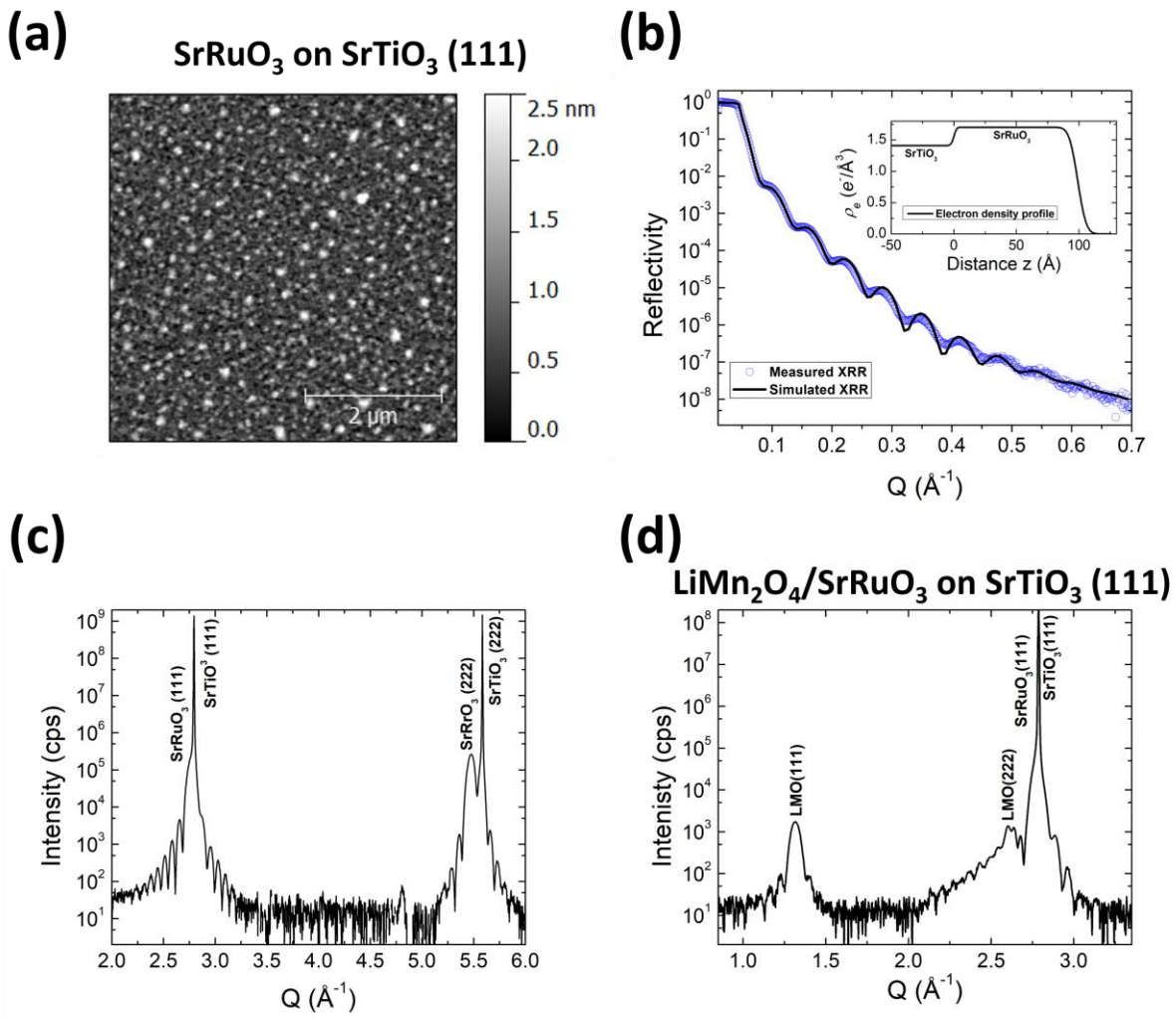

Figure 5.10 Characterizations of $SrRuO_3$ thin film on $SrTiO_3$(111) substrates. (a) AFM image for surface morphology. (b) XRR with measured data (blue circle) and fitted curve (black line). Insert is the electron density profile based on the fitting results. (c) Specular X-ray diffraction which shows the Bragg peaks of LSCO and substrates along surface normal direction. (d) Specular X-ray diffraction for LMO/$SrRuO_3$ bilayer thin film on $SrTiO_3$(111) which shows pure (111) orientated LMO on the top.

Moreover, the LMO/$SrRuO_3$(111) bilayer thin film (Figure 5.10(d)) clearly shows LMO (111) and LMO (222) Bragg peaks without any other orientation. Both LMO and $SrRuO_3$ are grown with expected epitaxy on $SrTiO_3$(111) substrate. This model is good for further *in operando* study.

There are still some of conducting materials we have tried but not mentioned. Among them, In:SnO_2 are the most interesting one. Though it doesn't provide excellent epitaxy for LMO growth, it's very stable and enhanced the cyclability of LMO. The details and data are included in Appendix I.

5.4 Comprehensive characterization of LMO(111)/$SrRuO_3$(111) bilayer epitaxial thin film on $SrTiO_3$(111) substrate

Figure 5.10(d) shows the specular X-ray diffraction for this bilayer system. Besides that, we also performed AFM and XRR, azimuthal phi-scans at typical as well as off-specular CTR scans. Moreover, we also conducted electrochemical test to ensure this system functions as we desire. AFM image (Figure 5.11(a)) shows clear triangles which is similar to that seen on LMO/$SrTiO_3$(111) single layer thin film (Figure 5.3(a)). However, unlike the triangles with uniform orientation shown in Figure 5.3(a), the triangles in Figure 5.11 (a) shows 2 different orientations with 180° difference. This orientation difference indicates 2 different in-plane alignments. The thickness and roughness obtained from XRR (Figure 5.11(b)) are 82.4 Å and 5.0 Å for $SrRuO_3$ buffer layer, 106.5 Å and 4.7 Å for LMO thin film, respectively. Benefitting from the using of area X-ray detector, we convert the specular (XR) and off-specular CTR scans into a reciprocal space map (Figure 5.11(c)). In reciprocal space map, LMO Bragg peaks from both

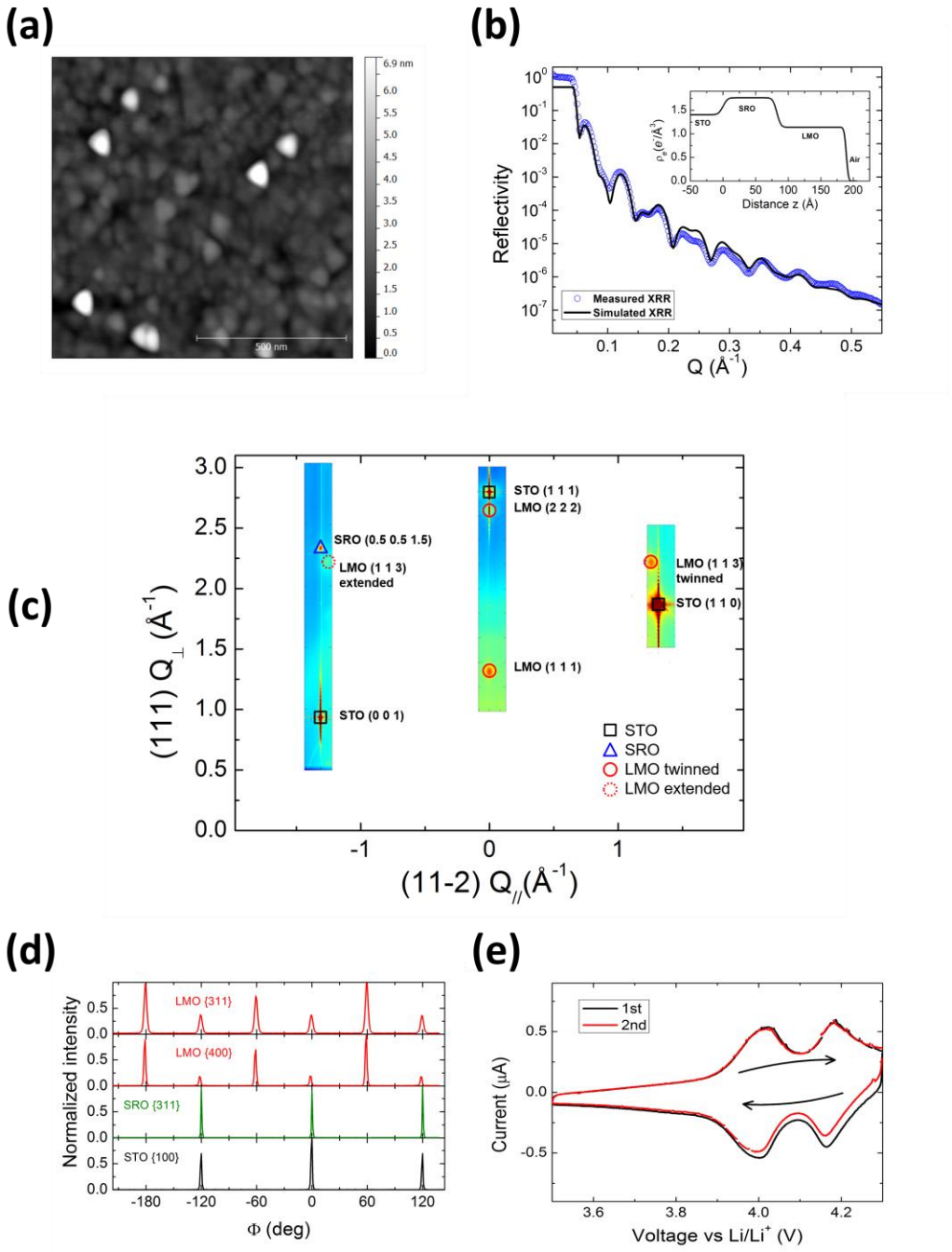

Figure 5.11 Characterizations of LMO/$SrRuO_3$ bilayer thin film on $SrTiO_3$(111) substrates. (a) AFM image for surface morphology. (b) XRR with measured data (blue circle) and fitted curve (black line). Insert is the electron density profile based on the fitting results. (c) Reciprocal map of crystal truncation rods along $SrTiO_3$ (111), $SrTiO_3$ (001) and $SrTiO_3$ (110). (d) Comparing of azimuthal phi-scans about LMO {311}, LMO{400}, SrRuO3 {311} and SrTiO3 {100} off-specular Bragg peak families. (e) CV for the first 2 cycles in the voltage range 3.5V to 4.3V.

twinned growth and extended growth have appeared which agrees with the observation from AFM image. Moreover, off-specular Bragg peak for SrRuO3 is horizontally aligned with the related substrate Bragg peak, while the off-specular Bragg peak for LMO is slightly shifted. This indicates that $SrRuO_3$ is fully in-plane strained on substrate lattice, while LMO is in-plane released. Although the LMO thin film is in-plane released, the relatively sharp peaks with uniform 60° distance in azimuthal phi-scans (Figure 5.11(d)) for LMO off-specular Bragg peak families suggest that LMO is still in-plane textured. The presence of 6 peaks, which are 2 sets of 3 peaks with 180° difference, fully matches the conclusion that LMO is grown in both twinned and extended ways. After comparing the peak intensity of the azimuthal phi-scans, we found that the twinned growth is dominated over extended growth. Cyclic voltammetry data (Figure 5.11(e)) clearly show two redox couples at 4.0 V and 4.16 V with little polarization, matching the known electrochemical response of LMO powders[167].

Therefore, we have successfully prepared smooth and epitaxial LMO(111) thin film on $SrTiO_3$(111) substrate with $SrRuO_3$ as conducting buffer layer. This fundamental work can promote the study about the orientation and surface effects on the electrochemical performance of LMO. It can also provide further insight into long-standing problem of the severe capacity fading in LMO.

Chapter 6 : *In Operando* Study of (111) Orientated $LiMn_2O_4$ Thin Film Cathode

6.1 Crystal structure of $LiMn_2O_4$ and its over-lithiated counterpart $LiMnO_2$.

Our *In operando* X-ray diffraction study mainly focuses on the structure changes under applied electrochemical condition. Therefore, before we go through the experiment details, it's useful to give a general introduction for the crystal structure of $LiMn_2O_4$ and its over-lithiated counterpart $LiMnO_2$.

$LiMn_2O_4$ has a spinel crystal structure (with space-group Fd-3m, as shown in Figure 6.1). Oxygen ions form a cubic close-packed (ccp) array which occupy the 32e position. Mn ions are located in the octahedral sites (16d for the normal spinel), while Li ions sit in tetrahedral sites (8a). MnO6 octahedra share edges in a three-dimensional host for the Li guest ions. The 8a tetrahedral site is situated furthest away from the 16d site among all the interstitial tetrahedra (8a, 8b and 48f) and

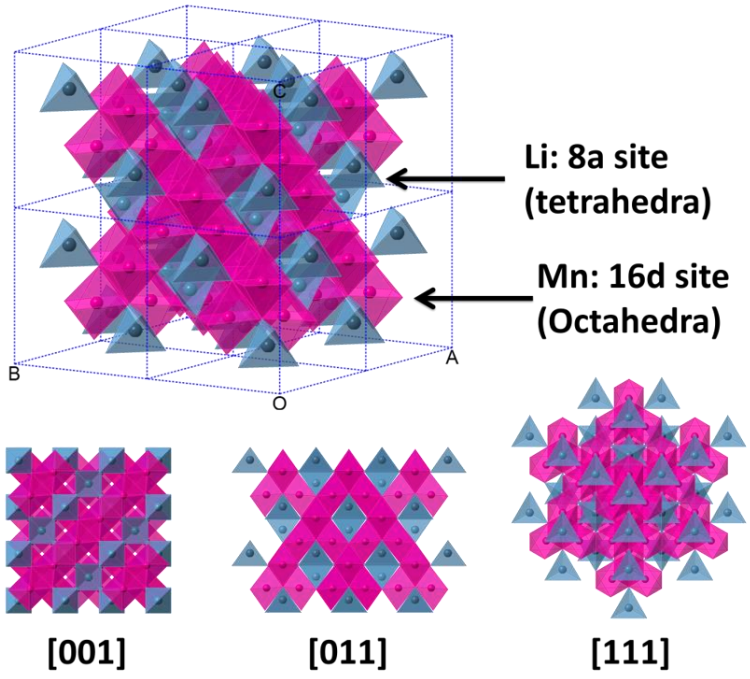

Figure 6.1 Crystal structure of $LiMn_2O_4$ and the top view from 3 typical direction. Blue tetrahedrons and purple octahedrons represent the sites occupied by Li and Mn, respectively.

octahedra (16c). Each of the 8a-tetrahedron faces is shared with an adjacent, vacant 16c site. This combination of structural features in the stoichiometric spinel compound constitutes a very stable structure.

$LiMnO_2$ belongs to the ternary ABO_2 rock-salt type structure family[168, 169]. Oxygen ions still form a ccp array, while all the cations (A and B) are located in the octahedral sites. Based on the cation distribution, the rock-salt type structure presents several polymorphs. Figure 6.2 depicts 3 typical categories of polymorphs. In order to easily understand the difference between those 3 structures, it is useful to consider the A and B cations arranging in layers

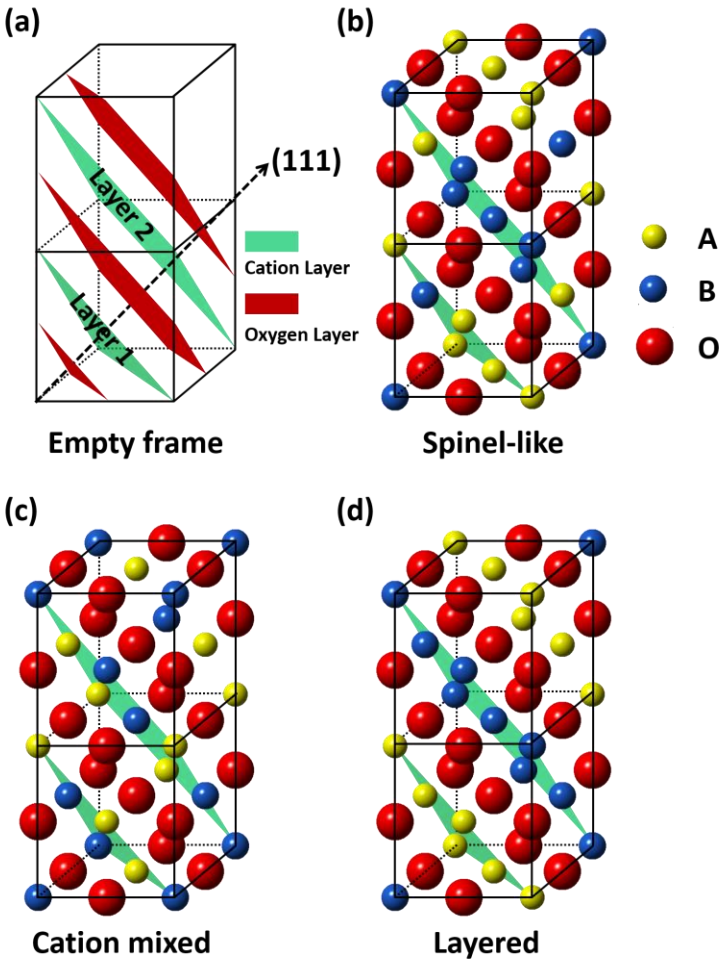

Figure 6.2 Three most common rock-salt type ABO_2 crystal structure. (a) Legend to illustrate different cation layers and (111) direction; (b) s"spinel-like" structure with 1:3 distribution; (c) "cation mixed" structure with all cation sites equivalent; (d) layered structure with cations A and B segregate into separate layers.

between close-packed oxygen layers which is perpendicular to (111) orientation (as shown in Figure 6.2(a)). Light green planes highlight 2 sequential cation layers marked as "layer 1" and "layer 2". The cation A and B ratios between layer 1 and layer 2 distinguished those 3 typical structures. In "spinel-like" structure (Figure 6.2(b)), one category of cations sits between oxygen layers with alternative 1:3 ratio, then the other category of cations takes similar distribution but with 3:1 ratio. The tetragonal phase $Li_2Mn_2O_4$ (t-$Li_2Mn_2O_4$) belongs to this category [10, 170]. The "cation mixed" structure (Figure 6.2(c)) represents a set of structures in which cation A and B are equally distributed (2:2) in the cation layers. Orthorhombic $LiMnO_2$ (o-$LiMnO_2$) belongs to this category [171-173]. In the "layered" structure (Figure 6.2(d)), cations A and B are totally separated

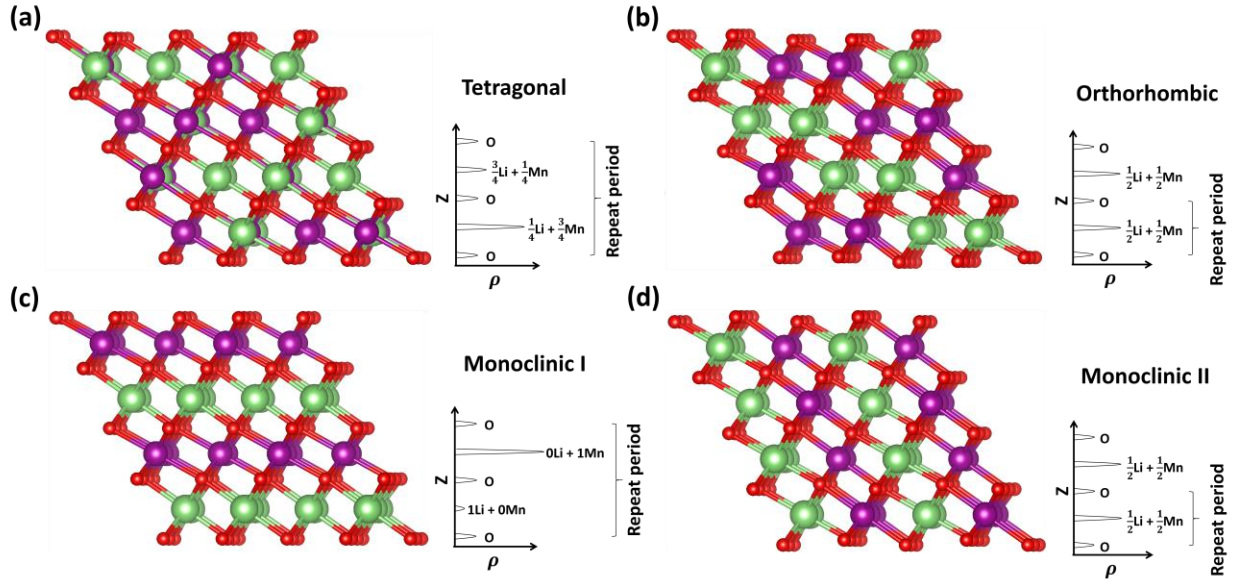

Figure 6.3 Crystal structure (side view of close-packed oxygen arrays) for (a) tetragonal t-$Li_2Mn_2O_4$; (d) orthorhombic o-$LiMnO_2$ and (c)(d) monoclinic m-$LiMnO_2$ with 2 different stacking orientations. Red, purple and green balls represent oxygen, manganese and lithium atoms, respectively. Projected electron density profiles along [111] direction for each structure are depicted on the right.

(0:4) into alternate cation layers. Monoclinic $LiMnO_2$ (m-$LiMnO_2$) belongs to this category [174].

For t-$Li_2Mn_2O_4$ and o-$LiMnO_2$ (Figure 6.3(a) and (d)), there is no difference if viewed from different direction. The always preserve their intrinsic Mn distribution ratio (1:3 and 2:2, respectively). However, in the m-$LiMnO_2$ phase, there are two ways to orient the Mn-layers, either parallel to (Figure 6.3(c)) or at an angle with respect to LMO (111) plane (Figure 3(d)), that lead to projected Mn distribution ratios of 0:4 and 2:2, respectively, along (111). These differences in the cation distributions are directly distinguished by the X-ray diffraction intensity of the LMO Bragg peak at around Q = 1.32 $Å^{-1}$ (for convenience, we will denote this Bragg peak using the spinel notation as LMO(111) throughout this chapter). With respect to the 1:3 Mn distribution found for the t-$Li_2Mn_2O_4$, where LMO (111) and (222) Bragg peaks are observed, the spinel (111) Bragg peak is absent with the 2:2 Mn distribution ratio for the o-$LiMnO_2$ phase (since the repeat period is reduced by half). In contrast, the intensity for the m-$LiMnO_2$ phase will depend on the orientation of the Mn-layers. LMO (111) Bragg peak will increase in the monoclinic phase when the Mn-layers are oriented parallel to (111) with an alternating 0:4 Mn distribution ratio, while this Bragg peak intensity will vanish when orientated at an angle with the (111) plane resulting in a 2:2 distribution ratio.

6.2 *In operando* study of strain-driven Mn-reorganization

In the chapter of LMO growth, we have introduced the procedure to prepare LMO epitaxial thin film with conducting buffer layer. Though the LMO epitaxial thin film is not fully strained with substrate lattice, it's bonded the substrate and will undergo in-plane tensile or compressive strains while contracts or expands, respectively. Our *in operando* study on this LMO epitaxial thin film successfully detected a Mn-reorganization phenomenon under those strains.

6.2.1 Experiment details

The sample fabrication and the characterization of as-deposit film have been thoroughly discussed in chapter 5. We have gotten well-defined (111) orientated LMO epitaxial thin film on $SrTiO_3$(111) substrate with $SrRuO_3$(111) as conducting buffer layer.

The electrochemical measurements are controlled and recorded by a CHI760D potentiostat. Li metal was used as both the counter and reference electrodes forming a half-cell, and all potentials are reported versus the Li/Li^+ redox couple. 1.2M LiPF6 in EC:EMC (3:7 by wt.) was used as the electrolyte. The open circuit potential of the as-deposited film was 3.7 V, indicating a nominal composition of $LiMn_2O_4$. Cyclic voltammetry (CV) measurements were performed in two-stages, each with multiple lithiation/delithiation cycles. The first stage used a potential range between 3.5 V and 4.3 V with a scan rate of 0.2 mV/s, while the second stage scans were performed

at potentials between 2.5 V and 4.3 V with a scan rate of 0.5 mV/s.

In Operando XRR measurements were performed in the low angle and crystal truncation rod (CTR) regimes at beamline 33BM-C of the Advanced Photon Source (APS) in Argonne National Laboratory (ANL) using an X-ray photon energy of 20.00 keV with an incident flux of ~ 10^{10} photons per second (additional measurements were performed at beamlines 12 ID-D). The X-ray beam (with cross-section of 3.8 × 0.3 mm^2 and divergence of 40 μrad = 0.0005 $Å^{-1}$ along 2θ direction) illuminated a 3.8 mm-wide by 2 mm-long area on the sample at the LMO (111) Bragg peak condition. Data were collected at fine intervals (low angle: ΔQ = 0.001 $Å^{-1}$; CTR regimes: ΔL = 0.002 r.l.u., corresponding to ΔQ = 0.0056 $Å^{-1}$) using an X-ray area detector (Pilatus 100k). Each *operando* measurement of the LMO thin film diffraction included 75 data points around LMO (111) Bragg peak (from L = 0.4 to 0.55 r.l.u., corresponding to Q = 1.15 to 1.53 $Å^{-1}$) with a 1 sec image time at each point. Between each scan, the X-ray beam was turned off for 200 sec.

6.2.2 Results and analysis

Ex situ X-ray characterization revealed the structure of as-deposit LMO/SRO/STO(111) thin film. The LMO and SRO layers have thicknesses of 106 $\pm$ 2 Å and 82 $\pm$ 2 Å respectively and electron densities of 1.14 $\pm$ 0.03 $e^-/Å^{-3}$ and 1.77 $\pm$ 0.04 $e^-/Å^3$, respectively, which match the known bulk electron densities for LMO (1.21 $e^-/Å^3$) (measured film electron density is little bit

lower due to inadequate coverage) and SRO (1.77 $e^-/Å^{-3}$).

In the first 2 electrochemical cycles of *in operando* study, the sample voltage is scanned between 3.5 V and 4.3 V at rate of 0.2 mV/s corresponding to Li stoichiometry ranging between $Li_xMn_2O_4$ ($0 < x < 1$). Cyclic voltammetry data (Figure 6.4(a)) clearly show two redox couples at 4.0 V and 4.16 V with little polarization, matching the known electrochemical response of LMO powders[167]. These CVs nearly overlap, indicating good capacity retention in this voltage region. In the second stage of cycling (3rd through 5th cycles), the discharge voltage was lowered to 2.5 V and the scan rate was increased to 0.5 mV/s with an additional redox couple appearing below 3 V (Figure 6.4(b)) from the lithiation range between $1 < x < 2$. In this stage, the redox features exhibit higher polarization and broadening, suggesting a kinetically sluggish process, and

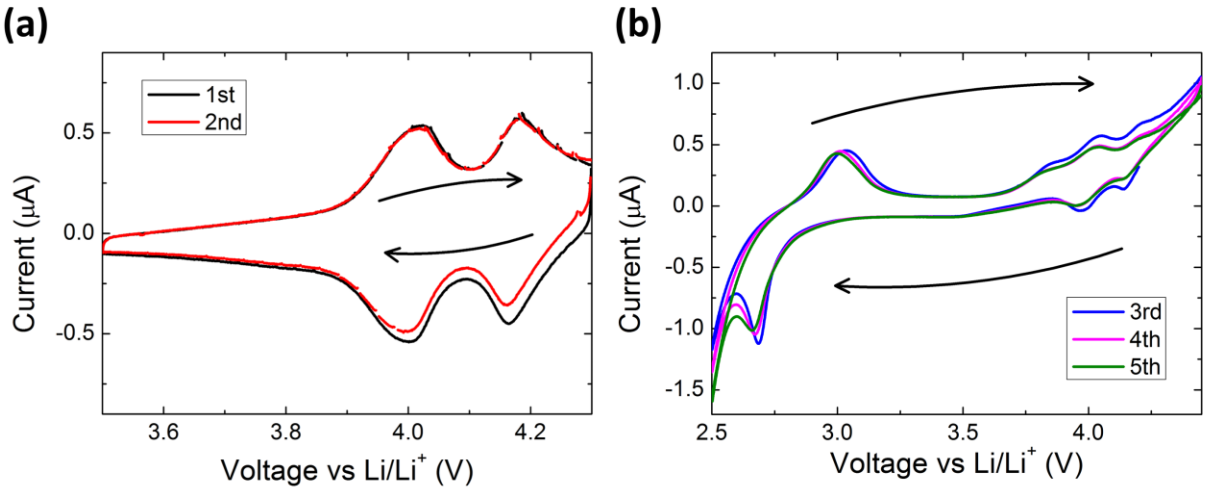

Figure 6.4 CV curve for $LiMn_2O_4/SrRuO_3$ epitaxial thin film on $SrTiO_3(111)$ substrate. (a) first 2 cycles between 3.5 V and 4.3 V; (b) 3rd to 5th cycles between 2.5 V and 4.3V.

generally diminish with each cycle indicating capacity loss.

Repeated CTR measurements near the LMO (111) Bragg peak started in the middle of 2nd cycle (3.5V). The 2D color map in Figure 6.5 provides a general picture of how LMO (111) Bragg peak changes with respect to the voltage. The results show that the LMO Bragg peak change in position, width and intensity as a function of applied potential, indicating that the film structure and morphology evolved during lithiation reactions. These changes are quantified by fitting the

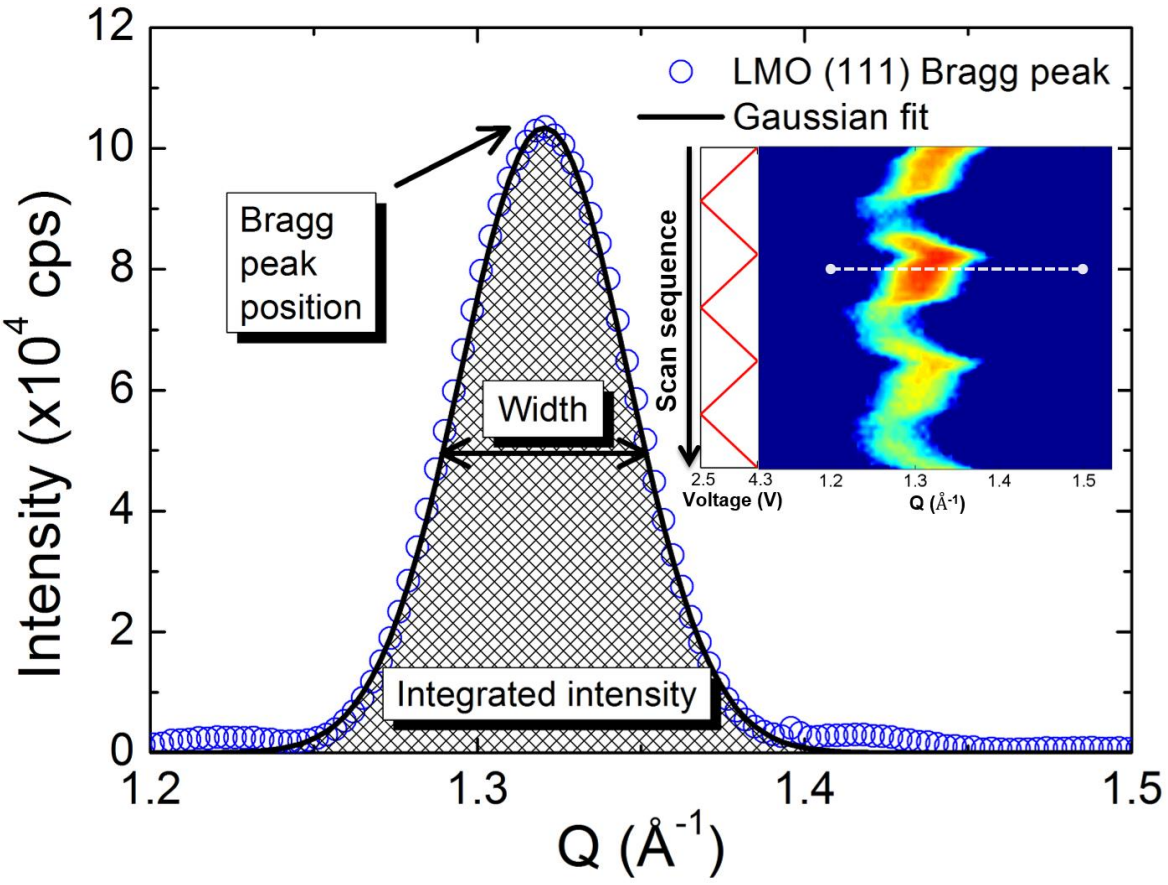

Figure 6.5 one of *in operando* LMO (111) Bragg peak scans with a Gaussian fit to indicate its position, width and integrated intensity. Insert is a 2-D color map of LMO (111) Bragg peak changes through 3rd to 5th cycle. White dash line marks the selected scan which has plotted out.

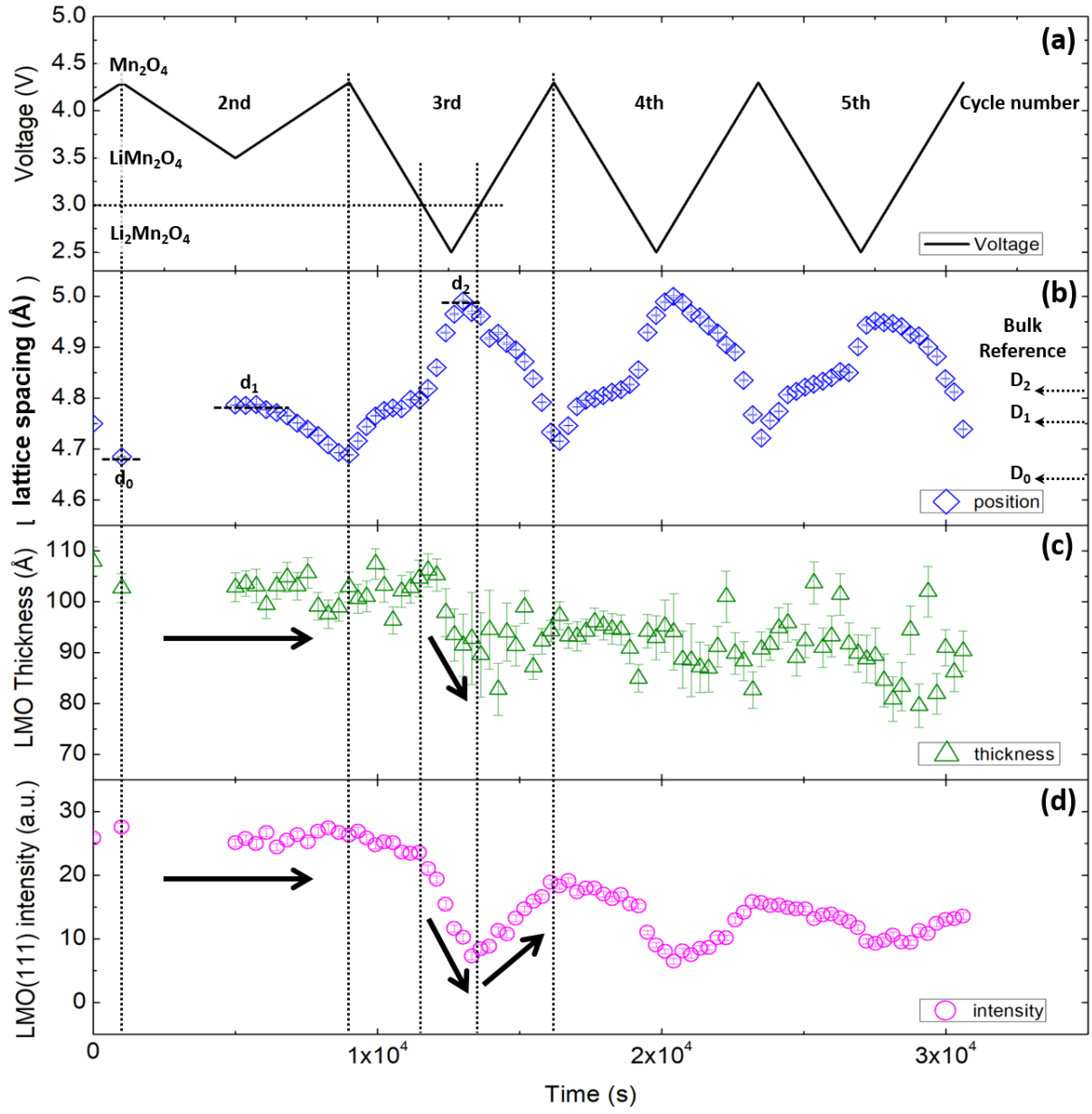

Figure 6.6 The time sequence of the $Li_xMn_2O_4$ $(0 \leq x \leq 2)$ thin film parameters with associated voltage. (a) voltage profile; (b) d-spacing of LMO (111) Bragg peak. D_0, D_1 and D_2 marks the d-spacing of bulk λ-Mn_2O_4, $LiMn_2O_4$ and $Li_2Mn_2O_4$ respectively. d_0, d_1 and d_2 marks the measured d-spacing of LMO(111) at those 3 states; (c) LMO film thickness; (d) integrated intensity of LMO (111) Bragg peak. Vertical dash lines divide 2nd cycle into region ① and 3rd cycle into region ②③④.

LMO(111) Bragg peak with a Gaussian function and a linear background (as shown in Figure 6.5), revealing the peak position (Q111), the peak width (ΔQ111), and the integrated intensity (I) versus time. These parameters reveal the LMO(111) d-spacing, and LMO film thickness (through the Scherrer equation $t = 2\pi/\Delta Q$). The integrated peak intensity is sensitive to multiple factors including the film coverage and the internal LMO crystal structure (e.g., the Mn-site distribution).

The evolution of these parameters is plotted chronologically along with the applied potential (Figure 6.6) , and labelled in four regions corresponding to the following changes in applied potential and lithium stoichiometry: ① a discharge/charge cycle from 4.3 V to 3.5 V and back to 4.3 V (x = 0 to 1, and then 0), ② discharge from 4.3 V to 3 V (x = 0 to 1), ③ deep discharge from 3 V to 2.5 V and back to 3 V (x = 1 to 2 and then 1) and ④ charge from 3 V and to 4.3 V (from x = 1 to 0).

The LMO lattice spacing (Figure 6.6(b)) is a direct indication of the lithiation state as Li insertion into LMO increases its lattice volume. The measured LMO d-spacing at 3 characteristic states is noted as $d_0(Mn_2O_4)$, $d_1(LiMn_2O_4)$ and $d_2(Li_2Mn_2O_4)$, which are compared to the corresponding d-spacing values of bulk LMO (D_0, D_1 and D_2 respectively). The observed values of d_0 and d_1 are close to D_0 and D_1 (within 0.8%), but d_2 is significantly larger than D_2 (by 3.5%). The LMO d-spacing ratio in $d_2/d_1 = 1.042$, is close to the expected volume change in bulk LMO

between $Li_2Mn_2O_4$ to $LiMn_2O_4$ (V_2/V_1 = 1.054). This suggests that, as expected, the LMO epitaxial thin film is laterally pinned to the substrate and compressive in-plane strain builds up for lithium compositions of x >1.

The changes of LMO film thickness (Figure 6.6(c)) with respect to applied voltage provide additional insight into the LMO reactivity. The thickness is stable when cycled above 3 V as shown (regions ① and ②) with a measured thickness of 105 ± 2 Å, consistent with the *ex situ* XRR characterization result (106.4 Å). However, there is a visible decrease of the measured film thickness when LMO film is discharged below 3 V (region ③). This is fully consistent with reported capacity fading in this region, which is due to loss of active material through Mn dissolution. These results, along with the variation in the LMO lattice spacing, are consistent with known lithiation behavior of LMO (except for the evidence for compressive strain in the fully lithiated phase).

Additional insights into the changes to the film structure are revealed in the evolution of the integrated intensity of LMO (111) Bragg peak (Figure 6.6(d)). The intensity is nearly unchanged when cycled beyond 3.5 V (regions ① and ②). However, a largely 80% decrease is observed for applied voltages below 3 V (region ③, the onset potential for lithiation to x=2). This change is partially recovered upon delithiation above 3 V (region ④ for x < 1) (maybe fully recovered if

stays with adequate time). The LMO thickness reveals only a loss of 10% of material in region ③, the 80% intensity drop in this region is not due to a loss of the LMO, especially given the observation that this intensity is partially recovered at higher applied potentials. Subsequent scans reveal similar behavior, with largely reversible changes in lattice spacing, a slow loss of film thickness below ~3 V, and an oscillatory variation in the LMO(111) Bragg peak intensity indicating that the behavior seen in the first few cycles was representative for the epitaxial LMO electrode.

To fully explore the apparent loss of LMO(111) intensity, we performed several full CTR measurements for a similar, separately prepared, electrode (deposited with nominal thicknesses of 10 nm LMO / 30 nm SRO / STO (111)), comparing the film structure in the as-deposited state and after 10 lithiation/delithiation cycles (Figure 6.7) (between 2.5 V and 4.3 V at a rate of 0.5 mV/s, the final state was held at 3.8 V for measurement). Comparison of these results reveal

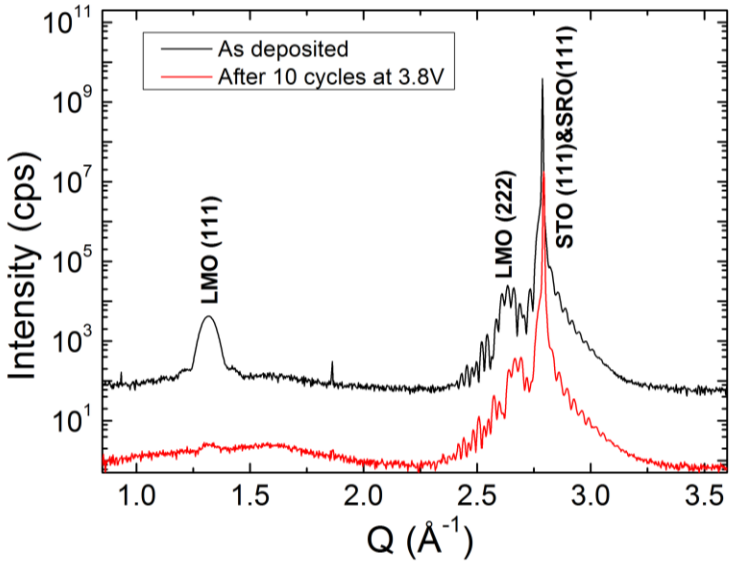

Figure 6.7 Full range specular CTR scans for a 10 nm LMO / 30 nm SRO / STO (111) thin film sample at as-deposited state and after 10 cycles.

that although the as-deposited film has well-defined LMO (111) and (222) Bragg peaks, after cycling the LMO(111) Bragg peak is strongly attenuated while the LMO (222) Bragg peak remains with only modest changes in position and intensity. This is direct evidence that while the LMO(111) Bragg peak is lost, the LMO film retains its crystallinity.

This large decrease in the LMO(111) intensity without significant changes in the LMO(222) reflection is explained by changes in the internal structure. The intensity of the LMO(111) Bragg peak derives from the modulation of the Mn ion occupation in alternating layers with a 1:3 ratio. A simple explanation for the observed loss of intensity is that the Mn site distribution changed to approximate 2:2 ratio due to the migration of Mn ions from the Mn-rich layer to the Mn-poor layer. For such a structure, the LMO (111) Bragg peak diffraction becomes forbidden (i.e., zero in intensity) while LMO (222) is largely unaffected. Combining all results, we conclude that the slow loss of LMO(111) Bragg peak intensity on subsequently deep lithiation cycles is associated with a kinetically limited reorganization of the Mn ions within the LMO host lattice.

6.3 Density functional theory calculation for the energy of different $LiMnO_2$ structures under specific in-plane strain condition.

Additional insights into the possible changes of $Li_xMn_2O_4$ film as a function of strain and lithiation level were obtained by density functional theory calculations (DFT). This work is performed by my collaborators, Márton Vörös and Juan C. Garcia.

The question that these calculations were designed to answer was whether the presence of compressive strain in the epitaxial film for compositions of $1 < x < 2$ could change the relative stability of the different LMO phases, as suggested by X-ray characterization. Since the unexpected loss of the LMO(111) Bragg peak intensity occurs at the second lithiation plateau at 3

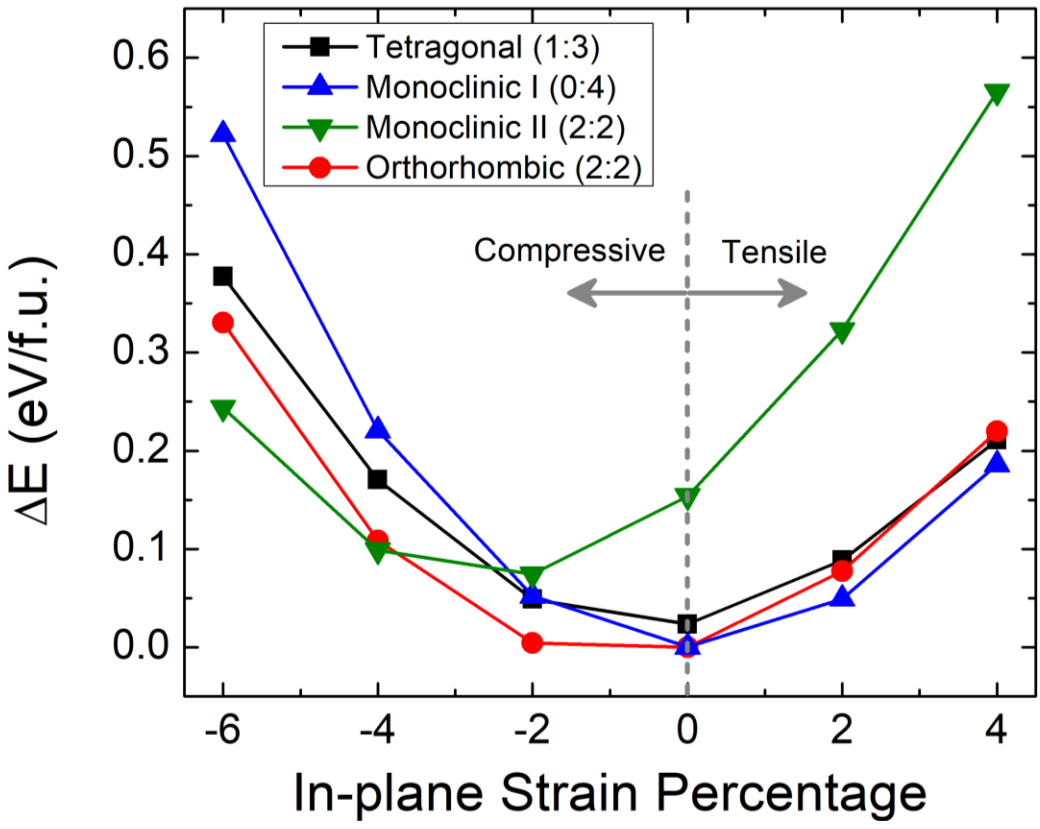

Figure 6.8 DFT results for relative energy per formula unit vs in-plane strain percentage for various LMO phases (see Figure 6.3) that differ solely by their Mn-site distributions. The vertical grey dash line separates the in-plane strain into compressive and tensile regimes.

V, we concentrate on the over-lithiated phase with composition $Li_2Mn_2O_4$. In order to be consistent with the experimental conditions, the DFT calculation adopted a hexagonal unit cell with a fixed in-plane lattice spacings, a = b, and the angle between these directions, $\gamma = 120°$. To address these questions, we calculate the relative energy per formula unit for $Li_2Mn_2O_4$ as a function of the in-plane lattice constant (Figure 6.8) for the four structures shown in Figure 6.3. In the absence of lateral strain, the tetragonal phase has ground state energies that are similar to that of the monoclinic I and orthorhombic phases with energy differences within a few tens of meV per formula unit, but it is not the energetically most favorable structure, in agreement with prior theoretical calculations[175]. The monoclinic phase I (Figure 6.3(c)) is energetically highly unfavorable with compressive in-plain strain. However, the monoclinic phase II (Figure 6.3(d)) develops a cooperative Jahn-Teller distortion that leads to a decreased energy. The JT distortion is cooperative since every Mn-O octahedron distorts in the same manner. In the cooperative JT phase, the fcc oxygen lattice became corrugated in the plane parallel to the substrate to accommodate the elongation of the Mn-O octahedrons perpendicular to the substrate. The energetic stabilization of the monoclinic phase II can also be attributed to its ability to accommodate compressive strains since it has a strongly anisotropic elastic response. Indeed, the monoclinic phase II is "softer" in the direction of the applied strain since it has more Li-O bonds whereas the monoclinic phase I only has the "harder" Mn-O bonds within the Mn-O plane in the direction of the strain. Moreover, the orthorhombic phase (Figure 6.3(b)) is also more energetically favored than tetragonal phase with compressive in-plain strain. Both the monoclinic II and orthorhombic phases have lower energy than tetragonal under experimental condition (i.e. around -4% in-plain strain (compressive) due to frozen in-plane lattice), and both have the Mn-site distribution that leads to the loss of the LMO(111) Bragg peak. From this and the apparent reversibility of the intensity loss upon

delithiation, we can conclude that there is a thermodynamic driving force for Mn migration that changes the Mn distribution from that found for the spinel phase (1:3) to the observed 2:2 ratio for $1 < x < 2$. Therefore, the calculation results reveal that the LMO structure is susceptible to internal redistribution of the Mn site distribution under compressive in-plane strain (imposed by epitaxial constraint of the thin-film).

6.4 Conclusion and discussion

These studies demonstrate a new way to control Mn ions distribution in $LiMn_2O_4$ cathode material during lithiation / delithiation. By means of epitaxial growth in (111) orientation, LMO lattice builds up compressive in-plane strain at overlithiated state. Both experimental observation and theoretical calculation suggest that, in this state, strain enables Mn ions migrate through oxygen layers and lead to a change of Mn distribution ratio at alternative cation layers from 1:3 in tetragonal phase to 2:2 that is equally distributed.

This work brings new thoughts about how can stain and stress affect the structure and properties of a material. If we can manipulate it properly, it may intrinsically solve the problems which can only be partially alleviated through outside compensation. For example, we can artificially introduce strain and stress to prevent Mn^{2+} from showing on the surface of LMO, and thus avoid the dissolution of LMO during cycling. To be more general, this strain-driven relocation of atoms may also provide instructive inspiration when dealing with structure crush in some electrode materials upon volume change. As well, this will deliver more insight into the study of surface phase which can be treated as surface layer bounded on the core. Moreover, as a strain-driven phenomenon, it can enrich the research range of the non-equilibrium study which attracts more and more attention in recent years.

Chapter 7 : Mg-Based Multi-Valent Cathode Materials

Although the Lithium ion battery (LIB) technology represents the current state-of-the-art rechargeable batteries and has steadily improved over the past decades (~8% increase in energy capacity and ~5% reduction in cost per year), they are unlikely to meet the future needs for transportation and electric grid that account for two-thirds of US energy use [176]. This recognition has driven substantial research into "beyond-lithium ion battery" technologies [177, 178] that would lead to either increase gravimetric/volumetric capacities or substantially reduced costs. Multivalent (MV) battery systems[71, 179-181] (using di- or trivalent ions, e.g., Mg^{2+} or Al^{3+} as the charge carrier instead of Li^{+}) are one possible candidate for beyond lithium systems. Theoretically, they are able to deliver folders (depending on the valent of charge carrier) of higher energy density comparing to LIBs[182, 183]. However, the search for an improved MV battery system has been impeded by the need to identify a suitable cathode material that addresses both the prohibitively high diffusional barriers that are expected for MV ion transport and the need for electrochemical stability in contact with relevant multivalent electrolytes (e.g., typically non-aqueous, non-Grignard electrolytes).

The knowledge accumulated from the study of $LiMn_2O_4$ cathode material gives us lot of inspiration on exploring the cathode of MV battery system. In analogy to $LiMn_2O_4$, with a very straightforward thought, we replaced charge carrier from Li^{+} to Mg^{+}. This idea is also supported

by a recent study showing that the delithiated (i.e. original from $LiMn_2O_4$) cubic phase λ-Mn_2O_4 can be inserted by Mg^{2+} in both aqueous and non-aqueous electrolytes[184]. However, this insertion is not reversible as $MgMn_2O_4$ (MMO) is a subsistent material and has already been proved to be electrochemically inert. After a deeper investigation, we found that the naturally existed MMO is with tetragonal crystal structure (noted as MMO_T), but it has a cubic polymorph which exists phase only at high temperature (>950 °C) or high pressure (>15.6 GPa). The cubic MMO (noted as MMO_C) film has quite different properties compared to its tetragonal phase. Previous work on powder materials have shown that MMO_C has only tens of Ω resistance instead of MΩ as in the tetragonal phase which indicates that their intrinsic transport properties maybe very different.

7.1 Preparing $MgMn_2O_4$ epitaxial thin film electrode with cubic and tetragonal structures

From the last chapter and works by other researchers[185, 186], we learn that epitaxial thin films often follow the structures of the underlying substrates and the relative stability of different phases can be controlled by lattice strain. Under this thought, we tried to seek proper substrate and conduction buffer layer to prepare MMO_C as well as tetragonal MMO_T (for comparison).

Similar procedures as for the growth of LMO epitaxial thin film (in chapter 5) have been made to explore proper deposition condition and auxiliary materials for the growth of MMO

epitaxial thin film. Finally, we found that conducting buffer layer TiC(001), which is epitaxially grown on MgO(001) substrate, can effectively stabilize the cubic phase of MMO. While another conducting buffer layer $La_{0.7}Sr_{0.3}FeO_3$ (LSFO), which is also epitaxially grown on MgO(001), leads to tetragonal phase of MMO on the top.

All the film depositions are fulfilled by PLD. Before deposition, MgO(001) substrates were annealed at 1100℃ in air for 12h to obtain atomically flat surface. Then, LSFO and TiC were deposited individually on MgO substrates with nominal thickness of 50 nm. After the deposition

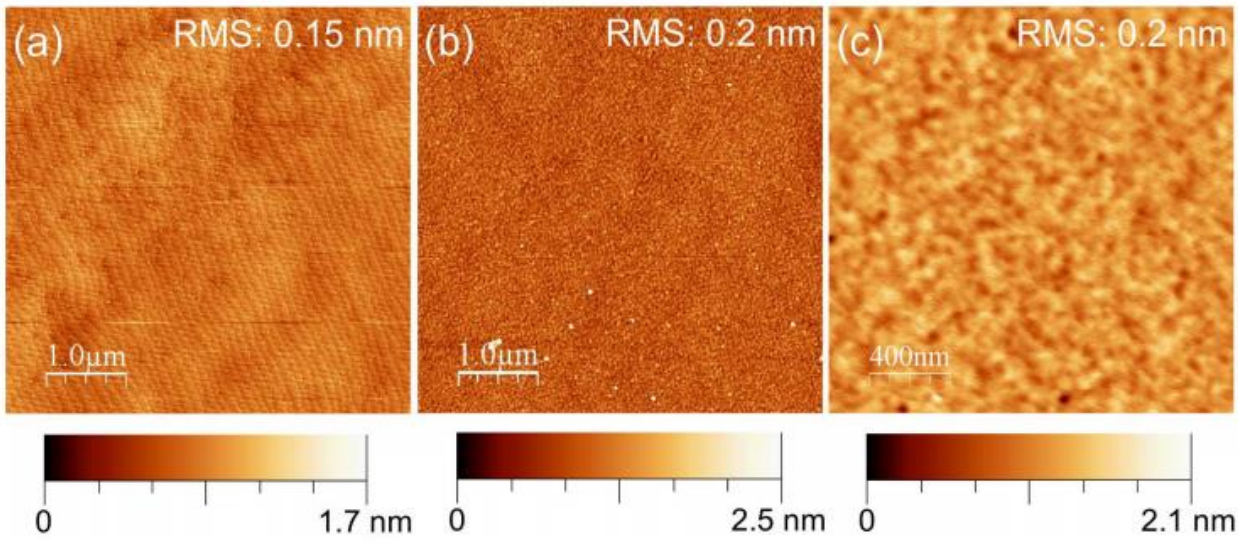

Figure 7.1 AFM images of (a) blank MgO substrate with clear terraces separated by ~ 40 nm. (b) Tetragonal $MgMn_2O^4$ grown on LSFO/MgO(001). (c) Cubic $MgMn_2O_4$ grown on TiC/MgO(001). Both MMO_T and MMO_C have same root-mean-square roughness of 0.2 nm.

of conducting buffer layer, MMO was deposited on the top of each buffer layer with nominal thickness of 70 nm. AFM measurement indicated that MMO thin film have smooth surface with root-mean-square roughness of 2Å (figure 7.1). Specular X-ray diffraction (Figure 7.2) for both MMO_T/LSFO/MgO(001) and MMO_C/TiC/MgO(001) confirmed the phase purity of MMO, LSFO and TiC thin films. When grown on LSFO/MgO(001), the MMOT phase is obtained with epitaxial alignment of MMO_T[001]//LSFO[001]//MgO[001] with $c_{tetragonal}$ = 9.244 Å. Together with off-specular XRD and in-plan scans (data not shown here), the in-plane epitaxy is confirmed as

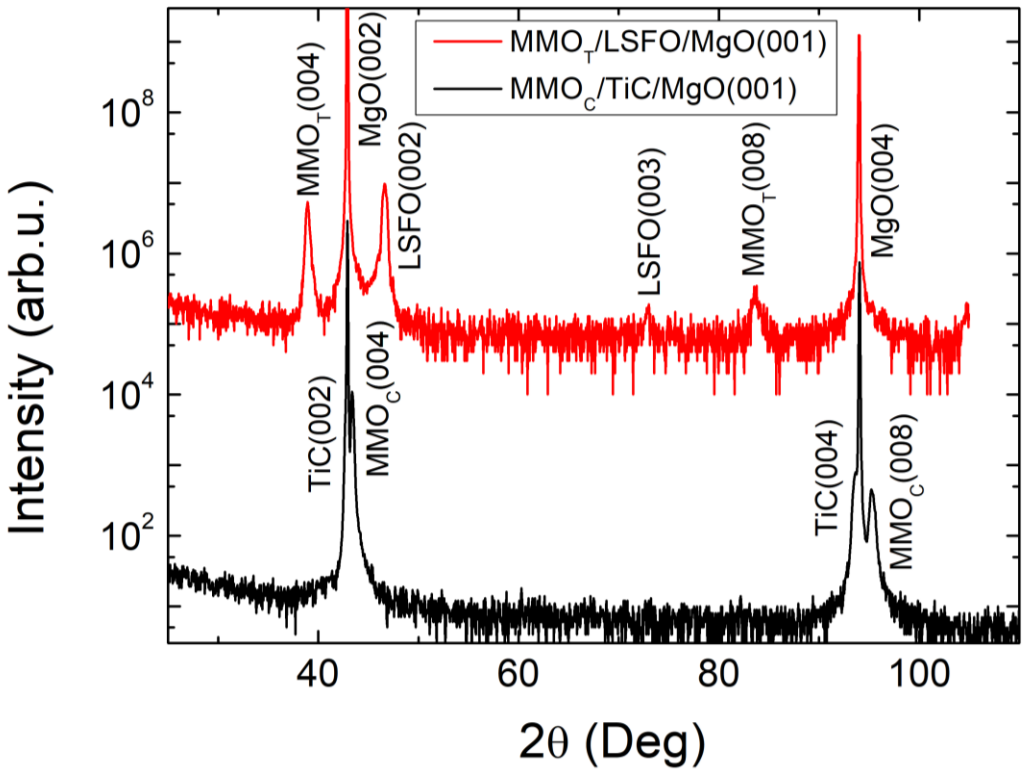

Figure 7.2 Specular X-ray diffraction on MMOT/LSFO/MgO(001) and MMOC/TiC/MgO(001). All Bragg peaks have been assigned to expected material.

MMO_T[101]//LSFO[111]//MgO[111] with $a_{tetragonal}$ = 5.722 Å. This tetragonal MMO (MMO_T) film has a 45° in-plane rotation with respect to LSFO and MgO substrates. In contrast, the cubic phase MMO_C was obtained when grown on TiC buffer layer. It follows the specular epitaxial relationships of MMO_C[001]//TiC[001]//MgO[001] and off-specular epitaxial relationships of MMO_C[404]//TiC[202]//MgO[202]. The lattice constants of MMO_C are measured to be a_{cubic} = 8.440 Å and c_{cubic} = 8.339 Å, which show a nearly perfect lateral lattice match (within experimental uncertainties) to the TiC film (a = 4.224Å, c = 4.218Å) and the MgO substrate (a = 4.212Å), namely $a_{MMO} \approx 2a_{TiC} \approx 2a_{MgO}$. This suggests that the strain of forming a MMO film that is fully commensurate with its TiC buffer layer stabilizes the cubic MMO phases.

This controlled growth of tetragonal and cubic phases of MMO can be understood by the different strains induced by the two buffer layers (TiC and LSFO). Although LSFO and TiC are both cubic phases, the TiC buffer layer on MgO(001) has a lattice constant 4.218 Å, while LSFO has a lattice constant 3.931 Å. Compared to the bulk lattice constants of 8.6 Å for MMO_C and 5.727 Å for MMO_T, the in-plane strain induced by TiC, $(a_{MMO} - 2a_{TiC})/(2a_{TiC})$ = 1.94%, is much less than the strain if MMOT is grown on TiC, $(\sqrt{2}a_{MMO} - 2a_{TiC})/(2a_{TiC})$ = −3.99%. However, to grow MMO on LSFO, the tetragonal phase has an advantage due to the smaller in-plane strain, $(\sqrt{2}a_{MMO} - 2a_{LSFO})/(2a_{LSFO})$ = 3.02%, as compared to that of MMO_C on LSFO, $(a_{MMO} - 2a_{LSFO})/(2a_{LSFO})$ = 9.39%.

Therefore, we conclude that epitaxial strain is a dominant factor to control and stabilize the different MMO phases in thin film form as we originally designed.

7.2 Electrochemical response of cubic $MgMn_2O_4$ vs tetragonal $MgMn_2O_4$

MMO_C/TiC/MgO(001) and MMO_T/LSFO/MgO(001) thin films were glued onto stainless steel supports and electrically connected to a stainless steel foil by silver paste that was sealed by Hysol 9462 epoxy. A capacitive anode was prepared by mixing BP2000 carbon (Cabot Corp.) with 40 wt % polyvinylidene difluoride (PVDF) and n-methyl-2-pyrrolidinone to make a viscous slurry. This slurry was then coated onto 304 stainless steel foil with a loading of ~4 mg/cm^2 and then dried in a vacuum oven at 75 °C for at least 8 h. Electrodes with a 7/16 in. diameter were punched from the sheet for use in the coin cell. These thin film cathodes were assembled in coin cell holders for battery tests, using a 0.2 $Mg(TFSI)_2$ in propylene carbonate (PC) electrolyte. Cyclic voltammetry measurements were performed at 1 mV/s scan rate using a CHI660E potentiostat. The charged (i.e., Mg-extracted) and discharged (i.e., Mg-inserted) states of these thin film cathodes were obtained after several cycles by holding the potential at 1 V for 14 h and at ~0 V for 5 h, respectively.

The CV curves for both MMO_T and MMO_C are shown in Figure 7.3(a). Little or no significant electrochemical current is observed for MMO_T, which is similar to the background CV curves of the epoxy on stainless steel reference. In contrast, MMO_C shows substantial redox activity. On the basis of the integrated charge from CV curves and the known thickness of the MMO_C film, the charge capacity is estimated to be 250 mAh/g (in the second cycle), which is comparable to the MMO theoretical value of 270 mAh/g[75]. These redox peaks gradually faded with increasing

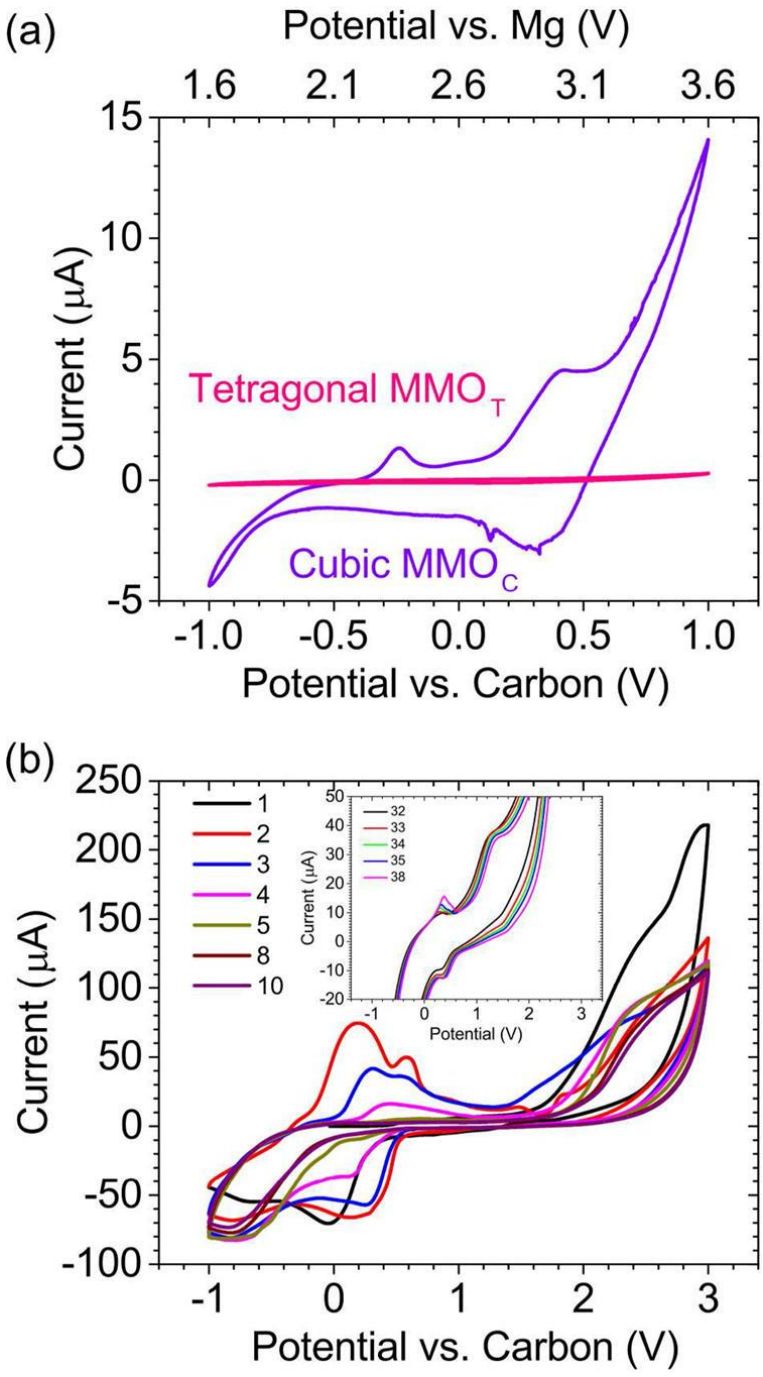

Figure 7.3 (a) Cyclic voltammetry (CV) of tetragonal MMO_T (pink) and cubic MMO_C (purple) thin film coin cells at 1 mV/s scan rate. The bottom axis is the measured voltage versus carbon, and the top axis is the estimated Mg/Mg^{2+} voltage. (b) extended CV data for cycling tests of the MMO_C at 1 mV/s scan rate.

cycle number; electrochemical activity can still be observed even after 38 cycles (with a capacity of 70 mAh/g), as shown in Figure 7.3(b). It obvious from these results that MMO_C exhibits substantially improved electrochemical performance compared to MMO_T.

Evidence that these observed redox reactions are due to changes in Mg^{2+} stoichiometry (i.e., removal and insertion of Mg) is obtained by characterizing MMO_T and MMO_C samples through multiple structural and spectroscopic approaches. Specular X-ray diffraction of MMO_T at the as deposited and charged states (Figure 7.4 (a)) shows no significant changes (e.g., in the peak position or width), consistent with the negligible electrochemical currents that were observed. In contrast, the MMO_C (004) lattice spacing (as measured by the (004) and (008) Bragg peak position)

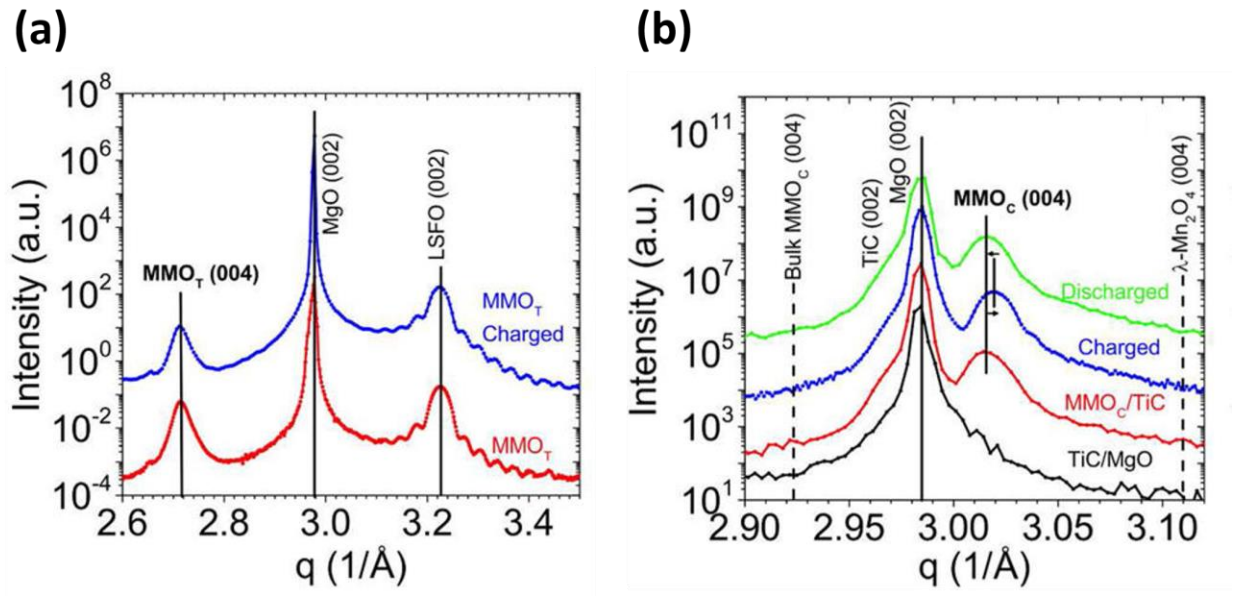

Figure 7.4 (a) Specular X-ray diffraction of tetragonal MMO_T around MgO (002) at as-deposited and charged states. (b) Specular X-ray diffraction of cubic MMO_c around MgO (002) at as-deposited, charged and discharged states.

exhibits small but significant shifts between the charged and discharged states (Figure 7.4(b)). This reversible change in the MMO_C lattice constant, $\Delta_{ccubic} = 0.01$ Å, is a direct indication of structure changes associated with the extraction of Mg^{2+} from the MMO_C lattice.

The activity of MMO_C was further demonstrated by observing the associated changes to the Mn oxidation state. X-ray absorption near edge spectroscopy (XANES) measurements at the Mn K absorption edge (Figure 7.5) reveals systematic shifts of the Mn K edge energies (E) following the trend $E(MnO_2) > E(MMO_C \text{ charged}) > E(MMO_C \text{ discharged})$, with an obvious edge shift of ~1.7 eV. This observation is consistent with the expected trend for Mn oxidation states, which is Mn(III) for $MgMn_2O_4$ and Mn(IV) for Mn_2O_4. These observations confirm that the charged MMO_C has an average Mn oxidation state between III and IV, demonstrating that magnesium was at least partially extracted.

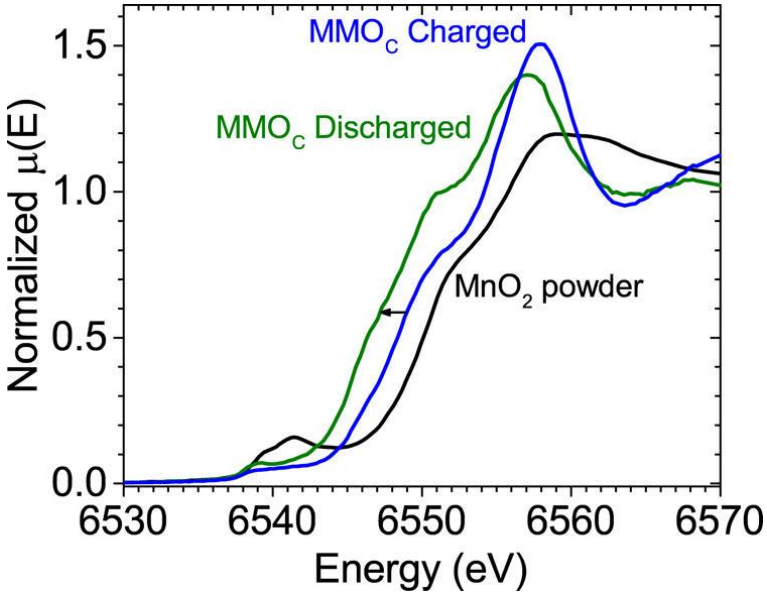

Figure 7.5 Mn K edge X-ray absorption near edge spectroscopy of the charged and discharged cubic MMO_C thin films and a MnO_2 reference powder. The small arrow indicates the edge shift (~1.7 eV) associated with the chemical state changes due to $Mg2^+$ extraction.

7.3 Conclusion and discussion

By means of epitaxial growth, we obtained cubic phase MMO epitaxial thin film in ambient environment whose bulk counterpart only exists at high temperature or in high pressure. This is another successful case about the phase-control through epitaxial bonding. From the results of further electrochemical investigation, we found that the cubic phase MMO exhibit dramatically different electrochemical properties as to the naturally exited tetragonal phase MMO. While no significant insertion behavior is found during charge / discharge cycles for tetragonal MMO films, reversible Mg^{2+} insertion was observed in cubic MMO films under identical experimental conditions.

This study provides a new though for seeking and evaluating the potential active materials in MV battery systems. Even with same stoichiometry, different phases may present totally different properties. Moreover, this research idea originates from the study of $LiMn_2O_4$, a cathode material for Li-ion battery. Therefore, we may further this research into more analogous area of Li-ion battery. The knowledge accumulated from decades of study on Li-ion battery can provide lots of insight into the MV battery investigation and avoid unnecessary waste of time.

Chapter 8 : Summary and outlook

Throughout six years' learning and research, I do have some small successes. But all of them are based on ten times of failure which is quite normal for all researchers. If I need to choose one part of my research that most important to me, I would say the LMO epitaxial thin film growth. Although this fundamental work may not attract much attention, it took most of my time in the past years with deposition, characterization, optimizing and repeat. Fortunately, I got well-defined (111) orientated LMO epitaxial thin film with proper conducting buffer layer. Based on this epitaxial thin film, we observed *in operando* changes of LMO crystal structure during electrochemical cycling. Those changes are attributed to a strain-driven cation redistribution. The ultimate reason is that the strain, which is induced from epitaxial bonding, largely affects the forming energies of different phases. This strain-induced phenomenon provides a useful thought for stabilizing disfavored phase or artificially manipulate the atoms distribution in a material.

Although, we got some interesting results from this LMO epitaxial thin film with highest quality (to my knowledge so far), there is still a long distance from our original goal. One the one hand, the film quality (i.e. roughness and coherence) is not high enough for crystal truncation rod measurement which is the starting motivation for this project. We are still curious about the structure changes and the solid-electrolyte interface reactions at the very surface of LMO during

electrochemical cycling. One the other hand, cyclable epitaxial LMO thin films with orientations other than (111) are still unavailable. I used to think LMO/SRO/STO(001) should be the most promising model to obtain LMO(001) epitaxial thin film, but it failed with (111) orientated LMO presenting. If we could acquire LMO epitaxial thin films with various well-defined orientations, we would be able to tell if there are different behaviors between different surface orientation. Then we can try to enlarge surface area ratio with superior orientation and thus improve the overall performance.

The study of the multi-valent cathode material $MgMn_2O_4$ is essentially the extending research of LMO. We stabilized the cubic phase of MMO through epitaxial bonding which is well explored in LMO study. Surprisingly, cubic phase MMO exhibits dramatically enhanced electrochemical properties as to the common existed tetragonal phase MMO. This result brings us to rethink about the materials that we claimed to be not suitable for MV battery system. It also provides a strong evidence that the phase difference (morphology or crystal structure) is able to dramatically change the transport properties of a material.

Multi-valent battery, as one category of beyond Li-ion battery systems, will undoubtedly attract more and more attention in the near future. We can fully utilize the analogous parts from Li-ion battery system, draw its experience and learn its lessons. Moreover, the electrolyte is also

an important part for MV battery system. Although our study hasn't reached this area, it does largely limit the choosing of electrode material.

For group IV intermetallic anode materials, they have highest capacity (besides pure Li) in theory. Therefore, the study focus is put on how to maximize its capacity utilization and how to avoid capacity fading. Multilayer architecture with metal interlayers is one of good approaches to alleviate the structure collapse along with large volume changes during electrochemical cycling. It's also an easy method to be realized in industry. The recently popular concept "solid state battery" also gets along well with multilayer architecture. Moreover, we have observed a reversible conversion reaction of Ti_xGe alloy, which is naturally formed at the interface between Ti and Ge, during electrochemical cycling. This conversion reaction makes Ti layers even more adhesive to the Ge layers, the active anode material. In this aspect, the utilization of Ti won't be limited in the multilayer architecture. It can be used as binder in any formats. In a more general view, Ti shouldn't be the only metal that can alloy with group IV intermetallic and undergo a reversible conversion reaction during electrochemical cycling. Therefore, we can keep exploring more suitable metal binders for specific anode materials.

At the end of this thesis, I would like to thank the six years of research. It changed not only my attitude to science, but also my way of thinking.

Reference

[1] E.S. Takeuchi, W.C. Thiebolt, The Reduction of Silver Vanadium-Oxide in Lithium Silver Vanadium-Oxide Cells, J Electrochem Soc, 135 (1988) 2691-2694.
[2] M.S. WHITTINGHAM, Electrical Energy Storage and Intercalation Chemistry, Science, 192 (1976) 1126-1127.
[3] D.R. Vissers, Z. Tomczuk, Steunenb.Rk, Preliminary Investigation of High-Temperature Lithium-Iron Sulfide Secondary Cells, J Electrochem Soc, 121 (1974) 665-667.
[4] E.C. Gay, D.R. Vissers, F.J. Martino, K.E. Anderson, Performance-Characteristics of Solid Lithium-Aluminum Alloy Electrodes, J Electrochem Soc, 123 (1976) 1591-1596.
[5] S. LeVine, The great battery race, Foreign Policy, (2010) 88.
[6] F.R. Gamble, J.H. Osiecki, M. Cais, Pisharod.R, Intercalation Complexes of Lewis Bases and Layered Sulfides - Large Class of New Superconductors, Science, 174 (1971) 493-&.
[7] J. Besenhard, G. Eichinger, High energy density lithium cells: Part I. Electrolytes and anodes, Journal of Electroanalytical Chemistry and Interfacial Electrochemistry, 68 (1976) 1-18.
[8] G. Eichinger, J. Besenhard, High energy density lithium cells: Part II. Cathodes and complete cells, Journal of Electroanalytical Chemistry and Interfacial Electrochemistry, 72 (1976) 1-31.
[9] J.J. Auborn, Y.L. Barberio, Lithium Intercalation Cells without Metallic Lithium - Moo2/Licoo2 and Wo2/Licoo2, J Electrochem Soc, 134 (1987) 638-641.
[10] M.M. Thackeray, W.I.F. David, P.G. Bruce, J.B. Goodenough, Lithium Insertion into Manganese Spinels, Mater Res Bull, 18 (1983) 461-472.
[11] C. Delmas, A. Nadiri, J.L. Soubeyroux, The Nasicon-Type Titanium Phosphates Liti2(Po4)3, Nati2(Po4)3 as Electrode Materials, Solid State Ionics, 28 (1988) 419-423.
[12] A. Manthiram, J.B. Goodenough, Lithium Insertion into Fe2(So4)3 Frameworks, J Power Sources, 26 (1989) 403-408.
[13] A. Nyten, A. Abouimrane, M. Armand, T. Gustafsson, J.O. Thomas, Electrochemical performance of Li2FeSiO4 as a new Li-battery cathode material, Electrochem Commun, 7 (2005) 156-160.
[14] R.K.B. Gover, P. Burns, A. Bryan, M.Y. Saidi, J.L. Swoyer, J. Barker, LiVPO4F: A new active material for safe lithium-ion batteries, Solid State Ionics, 177 (2006) 2635-2638.
[15] V. Legagneur, Y. An, A. Mosbah, R. Portal, A.L. La Salle, A. Verbaere, D. Guyomard, Y. Piffard, LiMBO3 (M = Mn, Fe, Co): synthesis, crystal structure and lithium deinsertion/insertion properties, Solid State Ionics, 139 (2001) 37-46.
[16] K. Mizushima, P. Jones, P. Wiseman, J. Goodenough, LixCoO2 ($0< x\leqslant 1$): A new cathode

material for batteries of high energy density, Solid State Ionics, 3 (1981) 171-174.
[17] M. Thackeray, W. David, P. Bruce, J. Goodenough, Lithium insertion into manganese spinels, Mater Res Bull, 18 (1983) 461-472.
[18] R. Yazami, P. Touzain, A reversible graphite-lithium negative electrode for electrochemical generators, J Power Sources, 9 (1983) 365-371.
[19] S. Basu, C. Zeller, P. Flanders, C. Fuerst, W. Johnson, J. Fischer, Synthesis and properties of lithium-graphite intercalation compounds, Mater Sci Eng, 38 (1979) 275-283.

[20] A. Yoshino, The Birth of the Lithium-Ion Battery, Angewandte Chemie International Edition, 51 (2012) 5798-5800.

[21] A.K. Padhi, K. Nanjundaswamy, J.B. Goodenough, Phospho-olivines as positive-electrode materials for rechargeable lithium batteries, J Electrochem Soc, 144 (1997) 1188-1194.
[22] S. Mizutani, H. Inoue, Anode active material method of manufacturing the same and nonaqueous electrolyte secondary battery using the same, in, Google Patents, 2010.
[23] D. Deng, Li-ion batteries: basics, progress, and challenges, Energy Sci Eng, 3 (2015) 385-418.
[24] J.M. Tarascon, M. Armand, Issues and challenges facing rechargeable lithium batteries, Nature, 414 (2001) 359-367.
[25] E. Peled, The electrochemical behavior of alkali and alkaline earth metals in nonaqueous battery systems—the solid electrolyte interphase model, J Electrochem Soc, 126 (1979) 2047-2051.
[26] M.N. Obrovac, V.L. Chevrier, Alloy Negative Electrodes for Li-Ion Batteries, Chem Rev, 114 (2014) 11444-11502.
[27] S. Goriparti, E. Miele, F. De Angelis, E. Di Fabrizio, R.P. Zaccaria, C. Capiglia, Review on recent progress of nanostructured anode materials for Li-ion batteries, J Power Sources, 257 (2014) 421-443.
[28] H. Wu, Y. Cui, Designing nanostructured Si anodes for high energy lithium ion batteries, Nano Today, 7 (2012) 414-429.
[29] C.K. Chan, H. Peng, G. Liu, K. McIlwrath, X.F. Zhang, R.A. Huggins, Y. Cui, High-performance lithium battery anodes using silicon nanowires, Nat Nanotechnol, 3 (2008) 31-35.
[30] H. Li, X. Huang, L. Chen, Z. Wu, Y. Liang, A high capacity nano Si composite anode material for lithium rechargeable batteries, Electrochemical and Solid-State Letters, 2 (1999) 547-549.
[31] M.T. McDowell, S.W. Lee, W.D. Nix, Y. Cui, 25th Anniversary Article: Understanding the Lithiation of Silicon and Other Alloying Anodes for Lithium-Ion Batteries, Adv Mater, 25 (2013)

4966-4985.
[32] H. Zhao, W. Yuan, G. Liu, Hierarchical electrode design of high-capacity alloy nanomaterials for lithium-ion batteries, Nano Today, 10 (2015) 193-212.
[33] M. Ko, S. Chae, J. Cho, Challenges in Accommodating Volume Change of Si Anodes for Li-Ion Batteries, Chemelectrochem, 2 (2015) 1645-1651.
[34] A. Mauger, H.M. Xie, C.M. Julien, Composite anodes for lithium-ion batteries: status and trends, Aims Mater Sci, 3 (2016) 1054-1106.
[35] X. Chen, T.T. Fister, J. Esbenshade, B. Shi, X.Y. Hu, J.S. Wu, A.A. Gewirth, M.J. Bedzyk, P. Fenter, Reversible Li-Ion Conversion Reaction for a TixGe Alloy in a Ti/Ge Multilayer, Acs Appl Mater Inter, 9 (2017) 8169-8176.
[36] E.M. Conwell, Properties of Silicon and Germanium, P Ire, 40 (1952) 1327-1337.
[37] C.S. Fuller, J.C. Severiens, Mobility of Impurity Ions in Germanium and Silicon, Phys Rev, 96 (1954) 21-24.
[38] J. Graetz, C.C. Ahn, R. Yazami, B. Fultz, Nanocrystalline and thin film germanium electrodes with high lithium capacity and high rate capabilities, J Electrochem Soc, 151 (2004) A698-A702.
[39] N. Nitta, F.X. Wu, J.T. Lee, G. Yushin, Li-ion battery materials: present and future, Mater Today, 18 (2015) 252-264.
[40] M.S. Whittingham, Lithium batteries and cathode materials, Chem Rev, 104 (2004) 4271-4301.
[41] G. Amatucci, A. Du Pasquier, A. Blyr, T. Zheng, J.M. Tarascon, The elevated temperature performance of the LiMn2O4/C system: failure and solutions, Electrochim Acta, 45 (1999) 255-271.
[42] Y.Y. Xia, Y.H. Zhou, M. Yoshio, Capacity fading on cycling of 4 V Li/LiMn2O4 cells, J Electrochem Soc, 144 (1997) 2593-2600.
[43] D. Aurbach, M.D. Levi, K. Gamulski, B. Markovsky, G. Salitra, E. Levi, U. Heider, L. Heider, R. Oesten, Capacity fading of Li(x)Mn(2)O(4) spinel electrodes studied by XRD and electroanalytical techniques, J Power Sources, 81 (1999) 472-479.
[44] K. Amine, J. Liu, S. Kang, I. Belharouak, Y. Hyung, D. Vissers, G. Henriksen, Improved lithium manganese oxide spinel/graphite Li-ion cells for high-power applications, J Power Sources, 129 (2004) 14-19.
[45] K.S. Lee, S.T. Myung, H.J. Bang, S.J. Chung, Y.K. Sun, Co-precipitation synthesis of spherical Li1.05M0.05Mn1.9O4 (M = Ni, Mg, Al) spinel and its application for lithium secondary battery cathode, Electrochim Acta, 52 (2007) 5201-5206.
[46] R.J. Gummow, A. Dekock, M.M. Thackeray, Improved Capacity Retention in Rechargeable

4v Lithium Lithium Manganese Oxide (Spinel) Cells, Solid State Ionics, 69 (1994) 59-67.
[47] Y.J. Lee, S.H. Park, C. Eng, J.B. Parise, C.P. Grey, Cation ordering and electrochemical properties of the cathode materials LiZnxMn2-O-x(4), 0 < x <= 0.5: A Li-6 magic-angle spinning NMR spectroscopy and diffraction study, Chem Mater, 14 (2002) 194-205.
[48] L. Hernan, J. Morales, L. Sanchez, J. Santos, Use of Li-M-Mn-O [M = Co, Cr, Ti] spinels prepared by a sol-gel method as cathodes in high-voltage lithium batteries, Solid State Ionics, 118 (1999) 179-185.
[49] J.H. Kim, S.T. Myung, C.S. Yoon, S.G. Kang, Y.K. Sun, Comparative study of LiNi0.5Mn1.5O4-delta and LiNi0.5Mn1.5O4 cathodes having two crystallographic structures: Fd(3)over-barm and P4(3)32, Chem Mater, 16 (2004) 906-914.
[50] G.H. Li, H. Ikuta, T. Uchida, M. Wakihara, The spinel phases LiM(y)Mn(2-y)O(4) (M=Co,Cr,Ni) as the cathode for rechargeable lithium batteries, J Electrochem Soc, 143 (1996) 178-182.
[51] J. Molenda, J. Marzec, K. Swierczek, D. Palubiak, W. Ojczyk, M. Ziemnicki, The effect of 3d substitutions in the manganese sublattice on the electrical and electrochemical properties of manganese spinel, Solid State Ionics, 175 (2004) 297-304.
[52] T. Ohzuku, S. Takeda, M. Iwanaga, Solid-state redox potentials for Li[Me1/2Mn3/2]O-4 (Me : 3d-transition metal) having spinel-framework structures: a series of 5 volt materials for advanced lithium-ion batteries, J Power Sources, 81 (1999) 90-94.
[53] R. Singhal, S.R. Das, M.S. Tomar, O. Ovideo, S. Nieto, R.E. Melgarejo, R.S. Katiyar, Synthesis and characterization of Nd doped LiMn2O4 cathode for Li-ion rechargeable batteries, J Power Sources, 164 (2007) 857-861.
[54] J. Tu, X.B. Zhao, D.G. Zhuang, G.S. Cao, T.J. Zhu, J.P. Tu, Studies of cycleability of LiMn2O4 and LiLa0.01Mn1.99O4 as cathode materials for Li-ion battery, Physica B-Condensed Matter, 382 (2006) 129-134.
[55] S.T. Yang, J.H. Jia, L. Ding, M.C. Zhang, Studies of structure and cycleability of LiMn2O4 and LiNd0.01Mn1.99O4 as cathode for Li-ion batteries, Electrochim Acta, 48 (2003) 569-573.
[56] D. Shu, G. Kumar, K.B. Kim, K.S. Ryu, S.H. Chang, Surface modification of LiMn2O4 thin films at elevated temperature, Solid State Ionics, 160 (2003) 227-233.
[57] A. Eftekhari, LiMn2O4 electrode prepared by gold-titanium codeposition with improved cyclability, J Power Sources, 130 (2004) 260-265.
[58] H.W. Liu, C.X. Cheng, Zongqiuhu, K.L. Zhang, The effect of ZnO coating on LiMn2O4 cycle life in high temperature for lithium secondary batteries, Mater Chem Phys, 101 (2007) 276-279.
[59] J.Q. Zhao, Y. Wang, Ultrathin Surface Coatings for Improved Electrochemical Performance

of Lithium Ion Battery Electrodes at Elevated Temperature, J Phys Chem C, 116 (2012) 11867-11876.
[60] D. Arumugam, G.P. Kalaignan, Synthesis and electrochemical characterizations of Nano-SiO2-coated LiMn2O4 cathode materials for rechargeable lithium batteries, J Electroanal Chem, 624 (2008) 197-204.
[61] H. Sahan, H. Goktepe, S. Patat, A. Ulgen, The effect of LBO coating method on electrochemical performance of LiMn2O4 cathode material, Solid State Ionics, 178 (2008) 1837-1842.
[62] X.F. Li, Y.L. Xu, C.L. Wang, Suppression of Jahn-Teller distortion of spinel LiMn2O4 cathode, J Alloy Compd, 479 (2009) 310-313.
[63] R. Vidu, P. Stroeve, Improvement of the thermal stability of Li-ion batteries by polymer coating of LiMn2O4, Ind Eng Chem Res, 43 (2004) 3314-3324.
[64] R.K. Guduru, J.C. Icaza, A Brief Review on Multivalent Intercalation Batteries with Aqueous Electrolytes, Nanomaterials-Basel, 6 (2016).
[65] P. Canepa, G.S. Gautam, D.C. Hannah, R. Malik, M. Liu, K.G. Gallagher, K.A. Persson, G. Ceder, Odyssey of Multivalent Cathode Materials: Open Questions and Future Challenges, Chem Rev, 117 (2017) 4287-4341.
[66] T.D. Gregory, R.J. Hoffman, R.C. Winterton, Nonaqueous electrochemistry of magnesium applications to energy storage, J Electrochem Soc, 137 (1990) 775-780.
[67] P. Novak, J. Desilvestro, Electrochemical Insertion of Magnesium in Metal-Oxides and Sulfides from Aprotic Electrolytes, J Electrochem Soc, 140 (1993) 140-144.
[68] M.E. Spahr, P. Novak, B. Schnyder, O. Haas, R. Nesper, Characterization of layered lithium nickel manganese oxides synthesized by a novel oxidative coprecipitation method and their electrochemical performance as lithium insertion electrode materials, J Electrochem Soc, 145 (1998) 1113-1121.
[69] P. Novak, R. Imhof, O. Haas, Magnesium insertion electrodes for rechargeable nonaqueous batteries - a competitive alternative to lithium?, Electrochim Acta, 45 (1999) 351-367.
[70] D.B. Le, S. Passerini, F. Coustier, J. Guo, T. Soderstrom, B.B. Owens, W.H. Smyrl, Intercalation of polyvalent cations into V2O5 aerogels, Chem Mater, 10 (1998) 682-+.
[71] D. Aurbach, Z. Lu, A. Schechter, Y. Gofer, H. Gizbar, R. Turgeman, Y. Cohen, M. Moshkovich, E. Levi, Prototype systems for rechargeable magnesium batteries, Nature, 407 (2000) 724-727.
[72] Z.X. Feng, X. Chen, L. Qiao, A.L. Lipson, T.T. Fister, L. Zeng, C. Kim, T.H. Yi, N. Sa, D.L. Proffit, A.K. Burrell, J. Cabana, B.J. Ingram, M.D. Biegalski, M.J. Bedzyk, P. Fenter, Phase-

Controlled Electrochemical Activity of Epitaxial Mg-Spinel Thin Films, Acs Appl Mater Inter, 7 (2015) 28438-28443.
[73] J.K. Kim, A. Manthiram, A manganese oxyiodide cathode for rechargeable lithium batteries, Nature, 390 (1997) 265-267.
[74] R.D. Shannon, Revised Effective Ionic-Radii and Systematic Studies of Interatomic Distances in Halides and Chalcogenides, Acta Crystallogr A, 32 (1976) 751-767.
[75] M. Liu, Z.Q. Rong, R. Malik, P. Canepa, A. Jain, G. Ceder, K.A. Persson, Spinel compounds as multivalent battery cathodes: a systematic evaluation based on ab initio calculations, Energ Environ Sci, 8 (2015) 964-974.
[76] R. Manaila, P. Pausescu, Structural Changes in Mgmn2o4 at High Temperatures, Phys Status Solidi, 9 (1965) 385-&.
[77] L. Malavasi, M.C. Mozzati, G. Chiodelli, C.B. Azzoni, G. Flor, RF sputtering deposition of MgMn2O4 spinel thin films, J Mater Sci, 39 (2004) 1671-1675.
[78] C. Kim, P.J. Phillips, B. Key, T.H. Yi, D. Nordlund, Y.S. Yu, R.D. Bayliss, S.D. Han, M.N. He, Z.C. Zhang, A.K. Burrell, R.F. Klie, J. Cabana, Direct Observation of Reversible Magnesium Ion Intercalation into a Spinel Oxide Host, Adv Mater, 27 (2015) 3377-3384.
[79] S. Mukerjee, T.R. Thurston, N.M. Jisrawi, X.Q. Yang, J. McBreen, M.L. Daroux, X.K. Xing, Structural evolution of LixMn2O4 in lithium-ion battery cells measured in situ using synchrotron X-ray diffraction techniques, J Electrochem Soc, 145 (1998) 466-472.
[80] M. Rosenberg, P. Nicolau, Electrical Properties and Cation Migration in Mgmn2o4, Phys Status Solidi, 6 (1964) 101-110.
[81] L. Malavasi, C. Tealdi, M. Amboage, M.C. Mozzati, G. Flor, High pressure X-ray diffraction study of MgMn2O4 tetragonal spinel, Nucl Instrum Meth B, 238 (2005) 171-174.
[82] D.M. Mattox, Handbook of physical vapor deposition (PVD) processing, William Andrew, 2010.
[83] R. Eason, Pulsed laser deposition of thin films: applications-led growth of functional materials, John Wiley & Sons, 2007.
[84] D.H. Lowndes, D. Geohegan, A. Puretzky, D. Norton, C. Rouleau, Synthesis of novel thin-film materials by pulsed laser deposition, Science, 273 (1996) 898.
[85] G. Binnig, C.F. Quate, C. Gerber, Atomic Force Microscope, Phys Rev Lett, 56 (1986) 930-933.
[86] G. Haugstad, Atomic force microscopy: understanding basic modes and advanced applications, John Wiley & Sons, 2012.
[87] O. Darrigol, The Electron Theories of Larmor and Lorentz - a Comparative-Study, Hist Stud

Phys Biol, 24 (1994) 265-336.
[88] P. Willmott, An introduction to synchrotron radiation: techniques and applications, John Wiley & Sons, 2011.
[89] D.H. Tomboulian, P.L. Hartman, Spectral and Angular Distribution of Ultraviolet Radiation from the 300-Mev Cornell Synchrotron, Phys Rev, 102 (1956) 1423-1447.
[90] K. Zhukovsky, Undulators for Short Pulse X-Ray Self-Amplified Spontaneous Emission-Free Electron Lasers, in: High Energy and Short Pulse Lasers, InTech, 2016.
[91] D. Attwood, B. Hartline, R. Johnson, The Advanced Light Source: Scientific Opportunities, Lawrence Berkeley Laboratory Publication, 511 (1984) 251-267.
[92] J.P. Blewett, Synchrotron radiation—1873 to 1947, Nuclear Instruments and Methods in Physics Research Section A: Accelerators, Spectrometers, Detectors and Associated Equipment, 266 (1988) 1-9.
[93] R.Z. Bachrach, Synchrotron Radiation Research: Advances in Surface and Interface Science Techniques, Springer Science & Business Media, 2012.
[94] H. Winick, G. Brown, K. Halbach, J. Harris, Wiggler and Undulator Magnets, Phys Today, 34 (1981) 50-&.
[95] S. Sasaki, K. Miyata, T. Takada, A new undulator for generating variably polarized radiation, Japanese journal of applied physics, 31 (1992) L1794.
[96] G. García, Synchrotron radiation: basics, methods and applications, in, Taylor & Francis, 2016.
[97] A. Baron, Y. Tanaka, S. Goto, K. Takeshita, T. Matsushita, T. Ishikawa, An X-ray scattering beamline for studying dynamics, J Phys Chem Solids, 61 (2000) 461-465.
[98] J.B. Hastings, X-Ray Optics and Monochromators for Synchrotron Radiation, J Appl Phys, 48 (1977) 1576-1584.
[99] M. Hart, L. Berman, X-ray optics for synchrotron radiation; Perfect crystals, mirrors and multilayers, Acta Crystallogr A, 54 (1998) 850-858.
[100] D.M. Mills, X-ray optics developments at the APS for the third generation of high-energy synchrotron radiation sources, J Synchrotron Radiat, 4 (1997) 117-124.
[101] A.K. Freund, X-Ray Optics for Synchrotron Radiation, Basic Life Sci, 51 (1989) 255-292.
[102] C. Malgrange, X-Ray Optics for Synchrotron Radiation, Acta Phys Pol A, 82 (1992) 13-32.
[103] B.D. Cullity, S.R. Cullity, S. Stock, Elements of X-ray Diffraction, 2001.
[104] C.J. Sparks, G.E. Ice, J. Wong, B.W. Batterman, Sagittal focusing of synchrotron x-radiation with curved crystals, Nuclear Instruments and Methods in Physics Research, 195 (1982) 73-78.
[105] D.M. Jens Als-Nielsen, Elements of Modern X-ray Physics

[106] A.A. Bunaciu, E.G. Udristioiu, H.Y. Aboul-Enein, X-Ray Diffraction: Instrumentation and Applications, Crit Rev Anal Chem, 45 (2015) 289-299.
[107] W.R. Busing, H.A. Levy, Angle calculations for 3-and 4-circle X-ray and neutron diffractometers, Acta Crystallogr, 22 (1967) 457-464.
[108] S. Mochrie, Four-circle angle calculations for surface diffraction, J Appl Crystallogr, 21 (1988) 1-4.

[109] G. Bushnell-Wye, R. Cernik, The general purpose two-circle diffractometer on Station 9.1,

Daresbury Laboratory, Rev Sci Instrum, 63 (1992) 999-1001.
[110] H. You, Angle calculations for a '4S+2D' six-circle diffractometer, J Appl Crystallogr, 32 (1999) 614-623.
[111] S.M. Gruner, E.F. Eikenberry, M.W. Tate, Comparison of X-ray detectors, in: M.G. Rossmann, E. Arnold (Eds.) International Tables for Crystallography Volume F: Crystallography of biological macromolecules, Springer Netherlands, Dordrecht, 2001, pp. 143-147.
[112] G. Rossi, M. Renzi, E.F. Eikenberry, M.W. Tate, D. Bilderback, E. Fontes, R. Wixted, S. Barna, S.M. Gruner, Tests of a prototype pixel array detector for microsecond time-resolved X-ray diffraction, J Synchrotron Radiat, 6 (1999) 1096-1105.
[113] J.S. Iwanczyk, E. Nygard, O. Meirav, J. Arenson, W.C. Barber, N.E. Hartsough, N. Malakhov, J.C. Wessel, Photon counting energy dispersive detector arrays for x-ray imaging, Ieee T Nucl Sci, 56 (2009) 535-542.
[114] J. Miyahara, K. Takahashi, Y. Amemiya, N. Kamiya, Y. Satow, A new type of X-ray area detector utilizing laser stimulated luminescence, Nuclear Instruments and Methods in Physics Research Section A: Accelerators, Spectrometers, Detectors and Associated Equipment, 246 (1986) 572-578.
[115] T. Taguchi, C. Bronnimann, E.F. Eikenberry, Next generation X-ray detectors for in-house XRD, Powder Diffr, 23 (2008) 101-105.
[116] B. Henrich, A. Bergamaschi, C. Broennimann, R. Dinapoli, E. Eikenberry, I. Johnson, M. Kobas, P. Kraft, A. Mozzanica, B. Schmitt, PILATUS: A single photon counting pixel detector for X-ray applications, Nuclear Instruments and Methods in Physics Research Section A: Accelerators, Spectrometers, Detectors and Associated Equipment, 607 (2009) 247-249.
[117] M. Bech, O. Bunk, C. David, P. Kraft, C. Brönnimann, E. Eikenberry, F. Pfeiffer, X-ray imaging with the PILATUS 100k detector, Applied Radiation and Isotopes, 66 (2008) 474-478.
[118] D. Attwood, A. Sakdinawat, X-rays and Extreme Ultraviolet Radiation: Principles and Applications, Cambridge university press, 2017.

[119] B.E. Warren, X-ray Diffraction, Courier Corporation, 1969.
[120] C. Hammond, C. Hammond, Basics of crystallography and diffraction, Oxford, 2001.
[121] W.H. Zachariasen, Theory of X-ray Diffraction in Crystals, Courier Corporation, 2004.
[122] R. Van Grieken, A. Markowicz, Handbook of X-ray Spectrometry, CRC Press, 2001.
[123] J. Waser, V. Schomaker, The Fourier inversion of diffraction data, Rev Mod Phys, 25 (1953) 671.
[124] M. Birkholz, Thin film analysis by X-ray scattering, John Wiley & Sons, 2006.
[125] V. Holy, J. Kubena, I. Ohli, K. Lischka, W. Plotz, X-ray reflection from rough layered systems, Phys Rev B, 47 (1993) 15896.
[126] E. Chason, T. Mayer, Thin film and surface characterization by specular X-ray reflectivity, Critical Reviews in Solid State and Material Sciences, 22 (1997) 1-67.
[127] J. Daillant, A. Gibaud, X-ray and neutron reflectivity: principles and applications, Springer, 2008.
[128] S. Sinha, E. Sirota, S. Garoff, H. Stanley, X-ray and neutron scattering from rough surfaces, Phys Rev B, 38 (1988) 2297.
[129] H. Zabel, X-ray and neutron reflectivity analysis of thin films and superlattices, Applied Physics A: Materials Science & Processing, 58 (1994) 159-168.
[130] J. Lekner, Theory of reflection, Springer, 1987.
[131] J.W. Shirley, An early experimental determination of Snell's law, American Journal of Physics, 19 (1951) 507-508.
[132] C.L. Giles, W.J. Wild, Fresnel reflection and transmission at a planar boundary from media of equal refractive indices, Appl Phys Lett, 40 (1982) 210-212.
[133] F.P. Miller, A.F. Vandome, M.B. John, Fresnel Equations, VDM Publishing, 2010.
[134] F.P. Miller, A.F. Vandome, J. McBrewster, Bragg's Law, Alphascript Publishing, 2010.
[135] A. Nelson, Co-refinement of multiple-contrast neutron/X-ray reflectivity data using MOTOFIT, J Appl Crystallogr, 39 (2006) 273-276.
[136] I.K. Robinson, Crystal truncation rods and surface roughness, Phys Rev B, 33 (1986) 3830.
[137] I. Robinson, D. Tweet, Surface X-ray diffraction, Reports on Progress in Physics, 55 (1992) 599.
[138] S. Dietrich, A. Haase, Scattering of x-rays and neutrons at interfaces, Physics Reports, 260 (1995) 1-138.
[139] L.M. Surhone, M.T. Timpledon, S.F. Marseken, X-Ray Crystal Truncation Rod, Betascript Publishing, 2010.
[140] U. Pietsch, V. Holy, T. Baumbach, High-resolution X-ray scattering: from thin films to

lateral nanostructures, Springer Science & Business Media, 2013.
[141] T. Kuech, Handbook of Crystal Growth: Thin Films and Epitaxy, Elsevier, 2014.
[142] P.F. Fewster, Reciprocal space mapping, Crit Rev Solid State, 22 (1997) 69-110.
[143] V. Kaganer, R. Köhler, M. Schmidbauer, R. Opitz, B. Jenichen, X-ray diffraction peaks due to misfit dislocations in heteroepitaxial structures, Phys Rev B, 55 (1997) 1793.
[144] H. Yoshida, K. Inaba, N. Sato, X-ray diffraction reciprocal space mapping study of the thin film phase of pentacene, Appl Phys Lett, 90 (2007) 181930.
[145] T. Boggon, J. Helliwell, R.A. Judge, A. Olczak, D. Siddons, E. Snell, V. Stojanoff, Synchrotron X-ray reciprocal-space mapping, topography and diffraction resolution studies of macromolecular crystal quality, Acta Crystallographica Section D: Biological Crystallography, 56 (2000) 868-880.
[146] T.T. Fister, J. Esbenshade, X. Chen, B.R. Long, B. Shi, C.M. Schleputz, A.A. Gewirth, M.J. Bedzyk, P. Fenter, Lithium Intercalation Behavior in Multilayer Silicon Electrodes, Adv Energy Mater, 4 (2014).
[147] R.J. Roe, Methods of X-ray and Neutron Scattering in Polymer Science, Oxford University Press, 2000.
[148] J. Als-Nielsen, Synchrotron X-Ray Studies of Liquid-Vapor Interfaces, Physica A, 140 (1986) 376-389.
[149] A.L. Patterson, A Fourier series method for the determination of the components of interatomic distances in crystals, Phys Rev, 46 (1934) 0372-0376.
[150] S.B. Astaf'ev, B.M. Shchedrin, L.G. Yanusova, Estimation of the Characteristic Parameters of the Multilayered Film Model Using the Patterson Differential Function, Crystallogr Rep+, 55 (2010) 127-135.
[151] C. Cao, H.G. Steinruck, B. Shyam, K.H. Stone, M.F. Toney, In Situ Study of Silicon Electrode Lithiation with X-ray Reflectivity, Nano Lett, 16 (2016) 7394-7401.
[152] Z.G. Wang, M. Gu, Y.G. Zhou, X.T. Zu, J.G. Connell, J. Xiao, D. Perea, L.J. Lauhon, J. Bang, S.B. Zhang, C.M. Wang, F. Gao, Electron-Rich Driven Electrochemical Solid-State Amorphization in Li-Si Alloys, Nano Lett, 13 (2013) 4511-4516.
[153] O. Thomas, F.M. Dheurle, S. Delage, Some Titanium Germanium and Silicon-Compounds - Reaction and Properties, J Mater Res, 5 (1990) 1453-1462.
[154] G. Evmenenko, T.T. Fister, D.B. Buchholz, Q. Li, K.-S. Chen, J. Wu, V.P. Dravid, M.C. Hersam, P. Fenter, M.J. Bedzyk, Morphological Evolution of Multilayer Ni/NiO Thin Film Electrodes during Lithiation, Acs Appl Mater Inter, 8 (2016) 19979-19986.
[155] T.T. Fister, X.Y. Hu, J. Esbenshade, X. Chen, J.S. Wu, V. Dravid, M. Bedzyk, B. Long, A.A.

Gewirth, B. Shi, C.M. Schleputz, P. Fenter, Dimensionally Controlled Lithiation of Chromium Oxide, Chem Mater, 28 (2016) 47-54.
[156] H.E. Swanson, E. Tatge, R.K. Fuyat, Standard X-ray diffraction powder patterns, (1953).
[157] K. Uehara, A. Okada, A. Okamoto, M. Yokura, S.L. Reddy, S. Kobayashi, K. Inaba, N. Iwata, R. Philip, H. Kezuka, M. Matsui, T. Endo, Hetero-epitaxial Growth of Cubic La(Sr)MnO3 on Hexagonal ZnO, In-Plane Orientations of La(Sr)MnO3 (001), (110), and (111) Phases, Japanese Journal of Applied Physics, 51 (2012).
[158] S. Chitra, P. Kalyani, T. Mohan, M. Massot, S. Ziolkiewicz, R. Gangandharan, M. Eddrief, C. Julien, Physical Properties of LiMn2O4 Spinel Prepared at Moderate Temperature, Ionics, 4 (1998) 8-15.
[159] T. Tomio, H. Miki, H. Tabata, T. Kawai, S. Kawai, Control of Electrical-Conductivity in Laser-Deposited Srtio3 Thin-Films with Nb Doping, J Appl Phys, 76 (1994) 5886-5890.
[160] L. Hultman, S. Barnett, J.-E. Sundgren, J. Greene, Growth of epitaxial TiN films deposited on MgO (100) by reactive magnetron sputtering: The role of low-energy ion irradiation during deposition, J Cryst Growth, 92 (1988) 639-656.
[161] H. Agura, A. Suzuki, T. Matsushita, T. Aoki, M. Okuda, Low resistivity transparent conducting Al-doped ZnO films prepared by pulsed laser deposition, Thin Solid Films, 445 (2003) 263-267.
[162] J.T. Cheung, P.E. Morgan, D.H. Lowndes, X.Y. Zheng, J. Breen, Structural and electrical properties of La0. 5Sr0. 5CoO3 epitaxial films, Appl Phys Lett, 62 (1993) 2045-2047.
[163] C. Chen, Y. Cao, Z. Huang, Q. Jiang, Z. Zhang, Y. Sun, W. Kang, L. Dezaneti, W. Chu, C. Chu, Epitaxial SrRuO 3 thin films on (001) SrTiO 3, Appl Phys Lett, 71 (1997) 1047-1049.
[164] L. Toth, Transition metal carbides and nitrides, Elsevier, 2014.
[165] N.P. Dasgupta, S. Neubert, W. Lee, O. Trejo, J.R. Lee, F.B. Prinz, Atomic Layer Deposition of Al-doped ZnO Films: Effect of Grain Orientation on Conductivity, Chem Mater, 22 (2010) 4769-4775.
[166] E. Kaidashev, M.v. Lorenz, H. Von Wenckstern, A. Rahm, H.-C. Semmelhack, K.-H. Han, G. Benndorf, C. Bundesmann, H. Hochmuth, M. Grundmann, High electron mobility of epitaxial ZnO thin films on c-plane sapphire grown by multistep pulsed-laser deposition, Appl Phys Lett, 82 (2003) 3901-3903.
[167] L. Feng, Y. Chang, L. Wu, T. Lu, Electrochemical behaviour of spinel LiMn2O4 as positive electrode in rechargeable lithium cells, J Power Sources, 63 (1996) 149-152.
[168] G.C. Mather, C. Dussarrat, J. Etourneau, A.R. West, A review of cation-ordered rock salt superstructure oxides, J Mater Chem, 10 (2000) 2219-2230.

[169] A. Urban, J. Lee, G. Ceder, The Configurational Space of Rocksalt-Type Oxides for High-Capacity Lithium Battery Electrodes, Adv Energy Mater, 4 (2014).
[170] A. Mosbah, A. Verbaere, M. Tournoux, Phases LixMnO2λ rattachees au type spinelle, Mater Res Bull, 18 (1983) 1375-1381.
[171] W. Johnston, R. Heikes, A Study of the LixMn (1-x) O System1, J Am Chem Soc, 78 (1956) 3255-3260.
[172] R. Hoppe, G. Brachtel, M. Jansen, Zur Kenntnis der Oxomanganate (III):, Über LiMnO2 und β-NaMnO2 [1], Z Anorg Allg Chem, 417 (1975) 1-10.
[173] Y. Wei, H. Ehrenberg, N.N. Bramnik, K. Nikolowski, C. Baehtz, H. Fuess, In situ synchrotron diffraction study of high temperature prepared orthorhombic LiMnO 2, Solid State Ionics, 178 (2007) 253-257.
[174] A.R. Armstrong, P.G. Bruce, Synthesis of layered LiMnO2 as an electrode for rechargeable lithium batteries, Nature, 381 (1996) 499.
[175] S.K. Mishra, G. Ceder, Structural stability of lithium manganese oxides, Physical Review B, 59 (1999) 6120-6130.
[176] Energy Information Administration Monthly Energy Review, in: May, 2014.
[177] J.B. Goodenough, K.S. Park, The Li-Ion Rechargeable Battery: A Perspective, Journal of the American Chemical Society, 135 (2013) 1167-1176.
[178] M.S. Whittingham, Materials challenges facing electrical energy storage, Mrs Bull, 33 (2008) 411-419.
[179] H.D. Yoo, I. Shterenberg, Y. Gofer, G. Gershinsky, N. Pour, D. Aurbach, Mg rechargeable batteries: an on-going challenge, Energy & Environmental Science, 6 (2013) 2265-2279.
[180] N. Jayaprakash, S.K. Das, L.A. Archer, The rechargeable aluminum-ion battery, Chem Commun, 47 (2011) 12610-12612.
[181] Y.Y. Shao, M. Gu, X.L. Li, Z.M. Nie, P.J. Zuo, G.S. Li, T.B. Liu, J. Xiao, Y.W. Cheng, C.M. Wang, J.G. Zhang, J. Liu, Highly Reversible Mg Insertion in Nanostructured Bi for Mg Ion Batteries, Nano Lett, 14 (2014) 255-260.
[182] R. Van Noorden, A Better Battery, Nature, 507 (2014) 26-28.
[183] M. Liu, Z. Rong, R. Malik, P. Canepa, A. Jain, G. Ceder, K. Persson, Spinel Compounds as Multivalent Battery Cathodes: A Systematic Evaluation Based on ab initio Calculations, Energy & Environmental Science, (2014).
[184] N.N. Sinha, N. Munichandraiah, Electrochemical Conversion of LiMn2O4 to MgMn2O4 in Aqueous Electrolytes, Electrochemical and Solid-State Letters, 11 (2008) F23-F26.

[185] H. Jeen, W.S. Choi, M.D. Biegalski, C.M. Folkman, I.C. Tung, D.D. Fong, J.W. Freeland, D. Shin, H. Ohta, M.F. Chisholm, H.N. Lee, Reversible redox reactions in an epitaxially stabilized SrCoOx oxygen sponge, Nat. Mater., 12 (2013) 1056-1062.
[186] R.G. Palgrave, P. Borisov, M.S. Dyer, S.R.C. McMitchell, G.R. Darling, J.B. Claridge, M. Batuk, H.Y. Tan, H. Tian, J. Verbeeck, J. Hadermann, M.J. Rosseinsky, Artificial Construction of the Layered Ruddlesden-Popper Manganite La2Sr2Mn3O10 by Reflection High Energy Electron Diffraction Monitored Pulsed Laser Deposition, J. Am. Chem. Soc., 134 (2012) 7700-7714.

Appendix A Electrochemical Cells

A.1 Beaker cell

Most electrochemical testing took place in two-electrode or three-electrode cells. The three-electrode cell has a working electrode, counter electrode, and reference electrode. In a two-electrode cell, the counter electrode acts as both the counter and reference electrodes. The electrodes of a beaker cell are immersed in an electrolyte in a beaker with some physical distance between the electrodes. Based on the general beaker cell principle, I designed a totally-enclosed beaker cell, which has defined sample exposure area, sealed environment as well as better electrical contact. It also reduced the electrolyte consumption for each experiment.

Name	Beaker cell
Designer	Xiao Chen
Sample size	10 ± 0.2 mm × 10 ± 0.2 mm
Type	Half cell
Working electrode	Sample for testing
Counter electrode	Lithium metal
Reference electrode	Lithium metal
Application	Long-term electrochemical cycling of thin film electrode material (with insulating substrate).

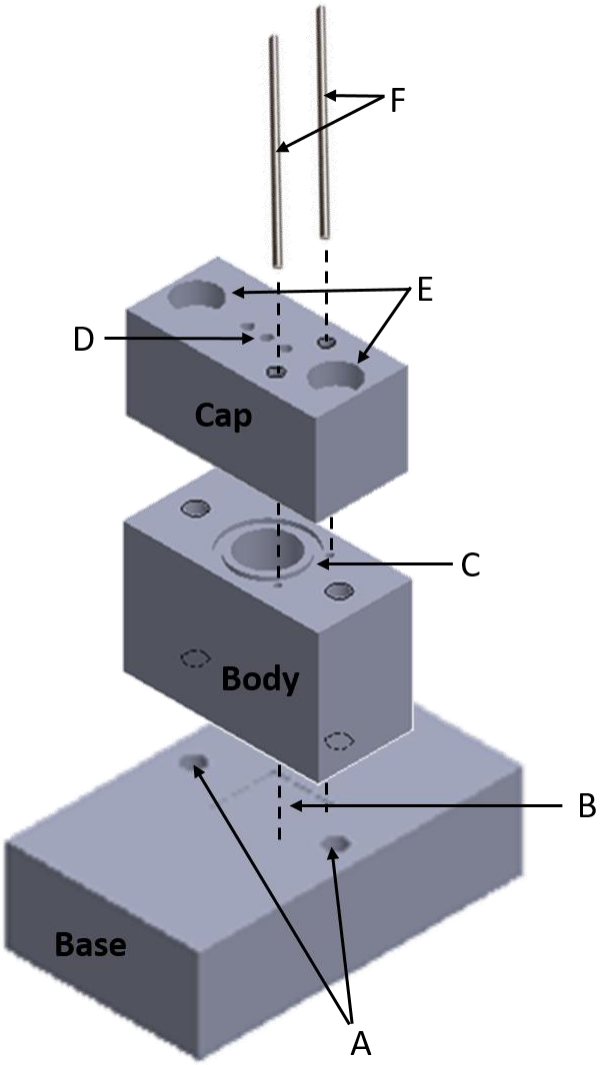

A. Base-Body connection (M3*20 mm Hex Socket Head Cap Screws).

B. Sample mounting slot (10 mm × 10 mm).

C. O-ring slot (⌀11 mm)

D. Three holes for ① hanging Li metal (counter and reference electrode), ② injecting electrolyte, ③ gas as extra electrolyte venting

E. Cap-Body connecting (M3*20 mm Hex Socket Head Cap Screws).

F. Metal rods (⌀1 mm) which contact the sample surface (working electrode).

Figure A1. Exploded view of beaker cell

The whole cell is made with Polychlorotrifluoroethylene (Kel-f). Sample is placed in the mounting slot (B), pressed by the body part and then sealed by the cap part. 2 metal rods (F) stab through the holes and contact sample surface. Li metal is attached to the copper wire and hung in the body part. Electrolyte is injected by a 10 mL syringe with needle tip through the holes on the cap (D). Li metal attaching and electrolyte injection should be done in glove box.

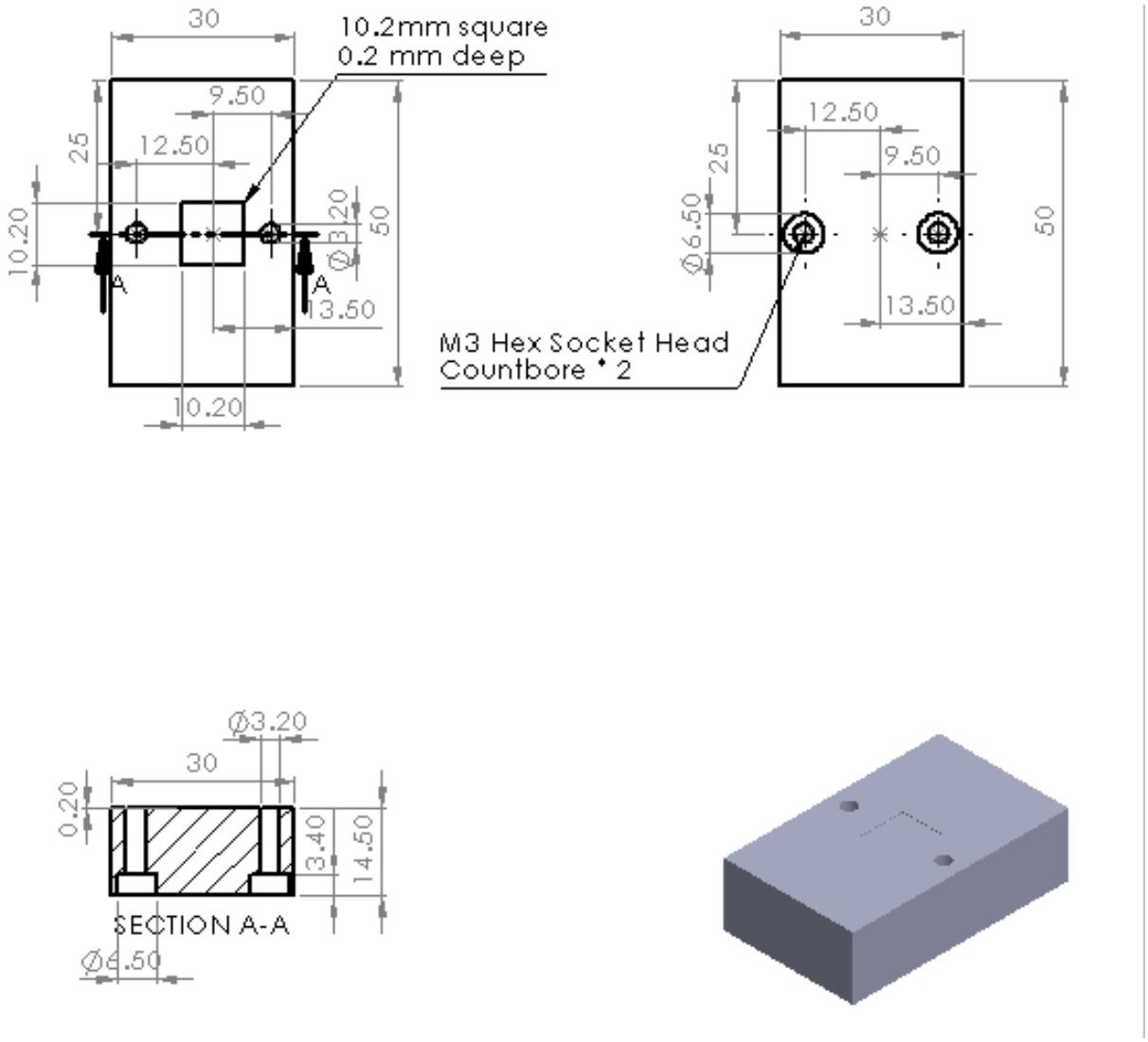

Figure A2. CAD drawing of base part of beaker cell

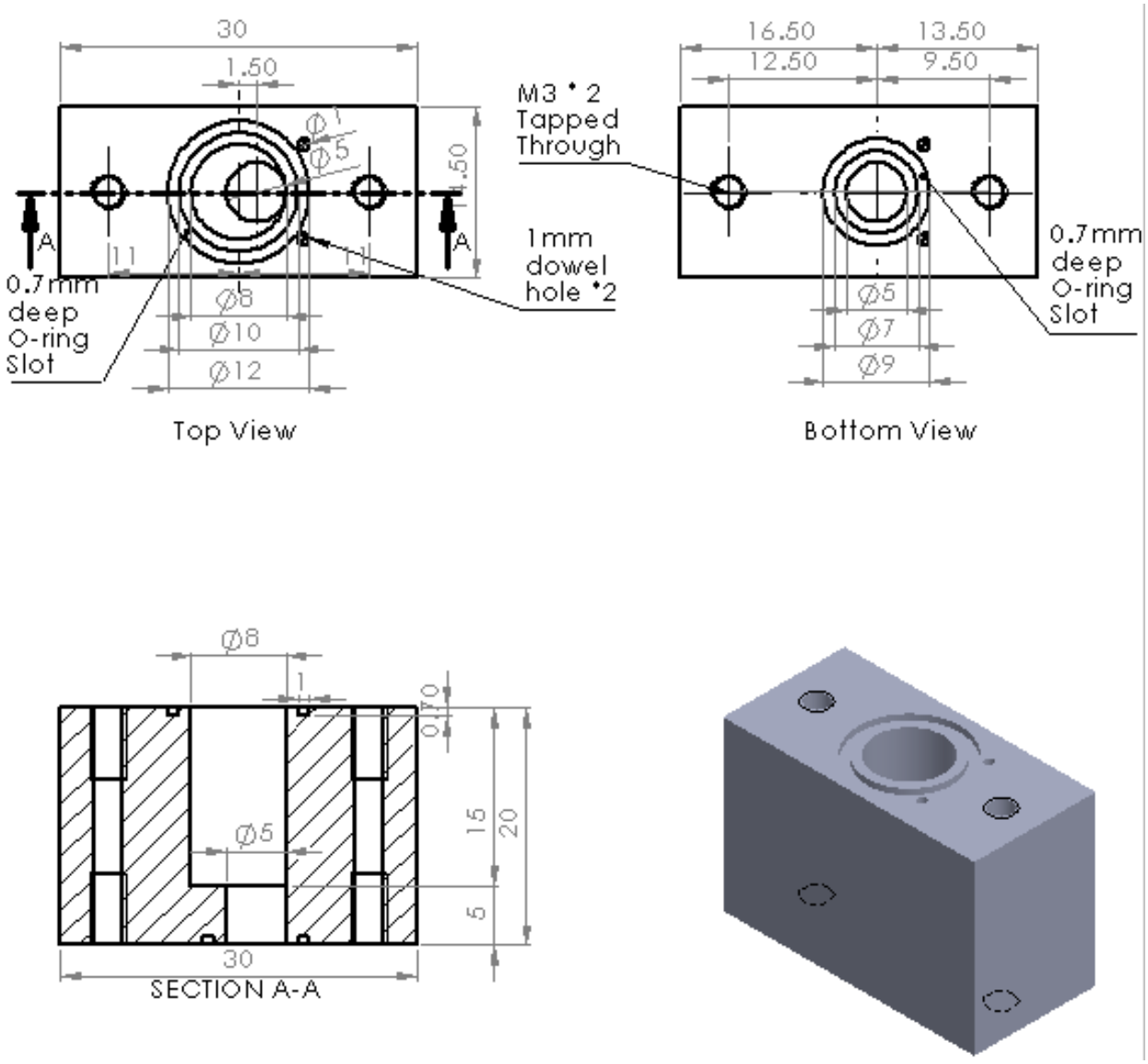

Figure A3. CAD drawing of body part of beaker cell

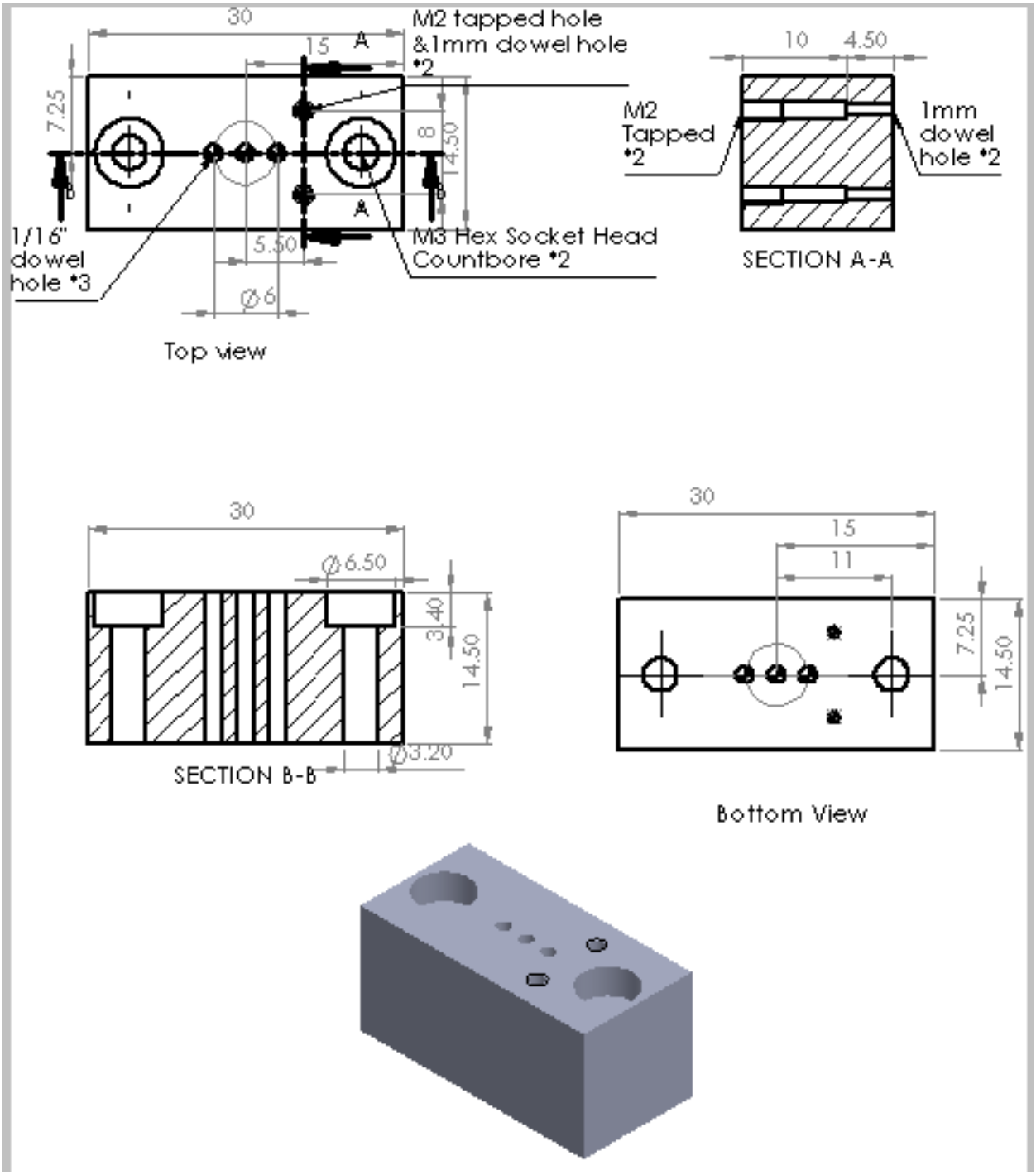

Figure A4. CAD drawing of cap part of beaker cell

A.2 Transmission cell

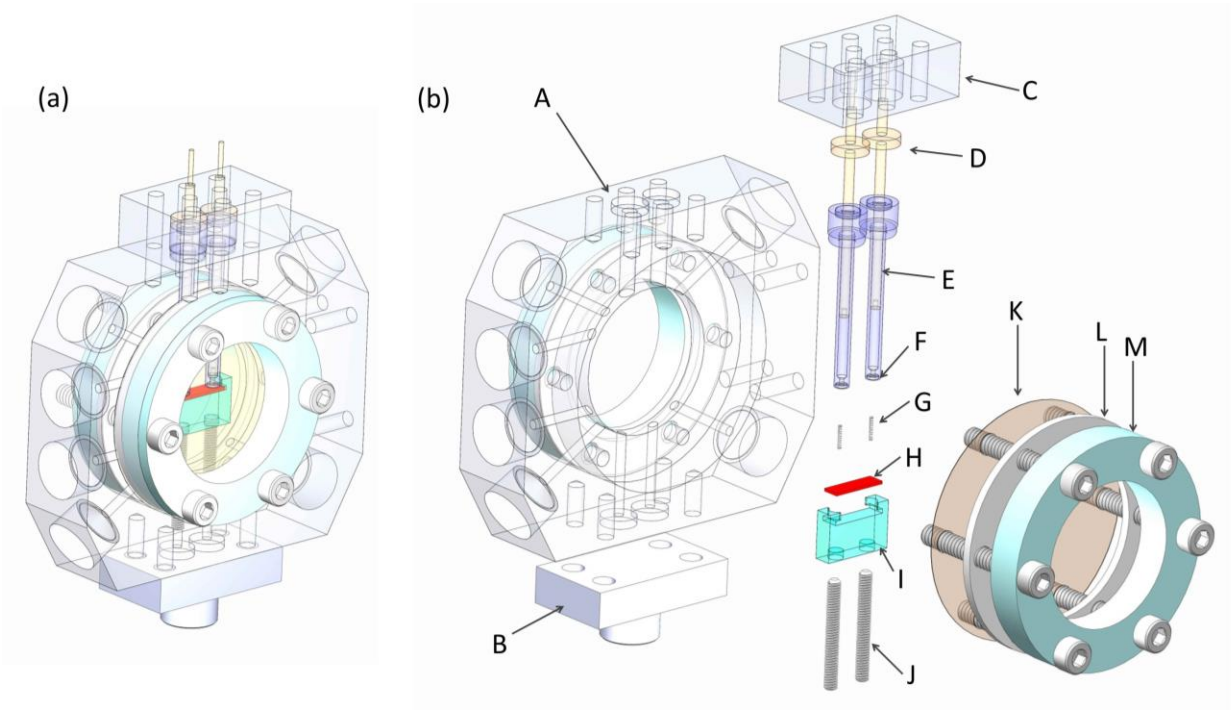

Figure A5. (a) Fully assembled transmission cell and (b) exploded view of cell with each part label A-M. Parts are described in the text.

Name	Transmission cell
Designer	Timothy Fister
Sample size	10 ± 0.2 mm × 3 ± 0.5 mm
Type	Half cell
Working electrode	Sample for testing
Counter electrode	Lithium metal
Reference electrode	Lithium metal
Application	Electrochemical cycling with *in situ* X-ray characterizations

This cell is referred to as a ‘transmission-geometry’ cell because the x-rays pass through the circular opening in the cell. The sample is fully immersed in the 1:1EC/DMC+1 M $LiPF_6$ electrolyte (Novolyte), in analogy with a traditional beaker electrochemical cell. At the working energy of 20 keV, the 3.5 mm path length leads to 20% x-ray absorption. The solution also increases the amount of background scatter, which was subtracted by fitting the specular rod peak in each image acquired by the area detector. The individual parts, as labeled in Figure A5 are:

(A) Kel-f cell body;

(B) Al goniometer adaptor;

(C) Kel-f working electrode clamp;

(D) stainless steel working electrode plungers;

(E) Kel-f plunger shells;

(F) 20-30 kfm O-ring (PSI);

(G) 0.024 in. OD stainless steel compression spring (Lee, CIM010ZA);

(H) 10x3x1 mm sample;

(I) Kel-f sample holder;

(J) 2-56 stainless steel set screw for sample height adjustment;

(K) Al_2O_3-coated 75 μm Kapton window (the coating prevents air/water permeation);

(L)Teflon flange;

(M) Kel-f window clamp.

The electrolyte inlet and outlet (syringe+stopcock+Teflon tubing, not shown) are attached via PVDF compression fittings on the cell body's NPT fittings. The counter/reference electrode is a piece of lithium foil crimped to a copper wire and laid above the sample in the cell. The copper wire is epoxied to glass tubing (to seal from outside air) and attached using a compression fitting. The other NPT fittings are capped, but could be used for additional electrodes or a bubbler.

The working electrode has a primary O-ring seal at the sample using a custom miniature O-ring and secondary O-ring seals at the working clamp. We found that the working electrode seal is particularly important for samples with non-ideal conductivity and nanoscale thicknesses. In this case, IR losses appeared to be minimal. The exposed area of the electrode is 0.25 cm^2.

All Kel-f and Teflon parts in contact with the electrolyte were soaked overnight in concentrated (97%) sulfuric acid + nochromix and then rinsed repeatedly with DI water until the pH of the effluent was above 6.5. The remaining parts were sonicated in methanol and rinsed with DI water. All parts are dried in a vacuum furnace for at least 12 hours before assembly. The cell is mostly assembled outside of the glovebox; the lithium metal, windows, and electrolyte are attached inside an Ar-filled glovebox (O_2 < 1 ppm).

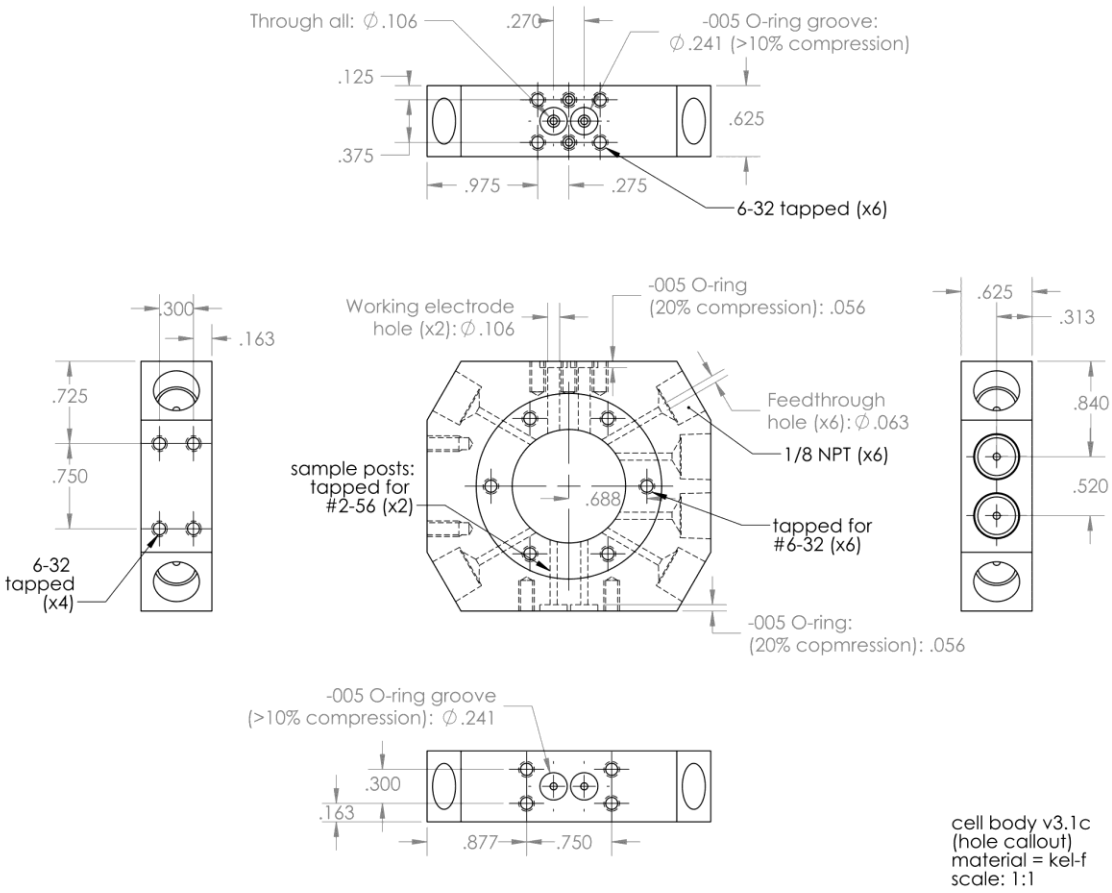

Figure A6. CAD drawing of cell body for transmission cell

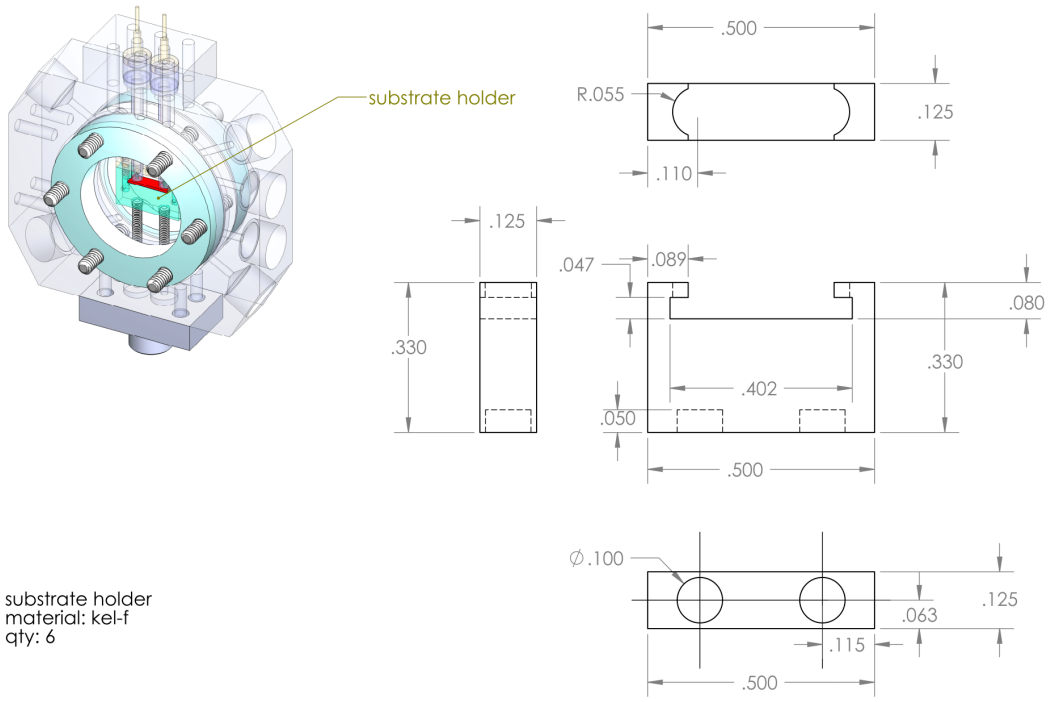

Figure A7. CAD drawing of substrate holder for transmission cell

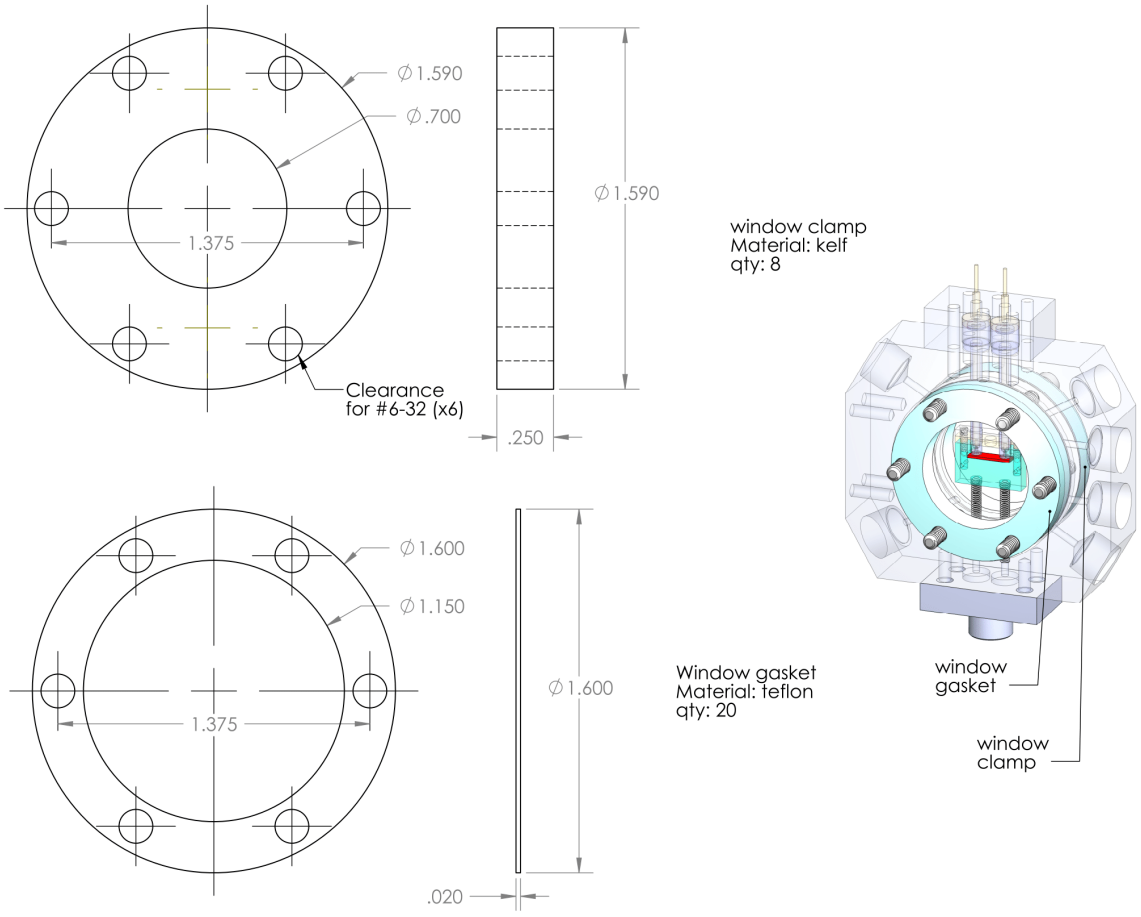

Figure A8. CAD drawing of window clamp for transmission cell

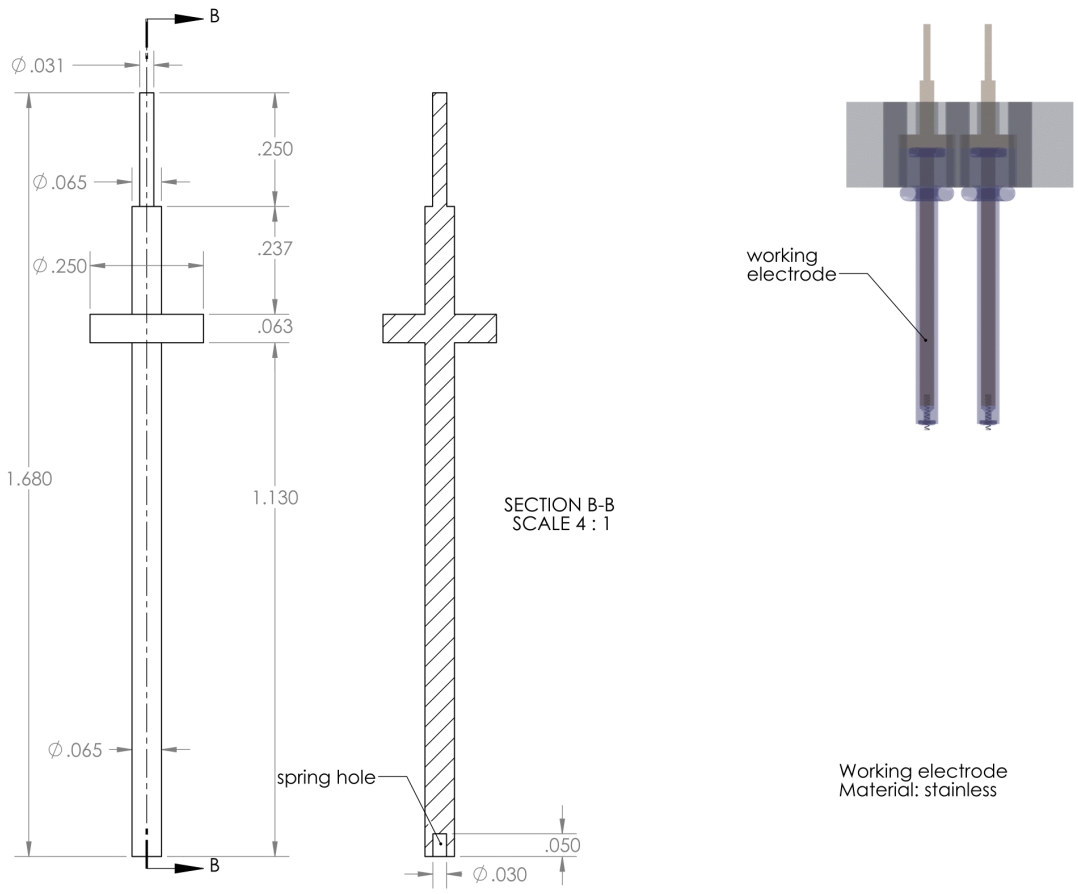

Figure A9 CAD drawing of working electrode for transmission cell

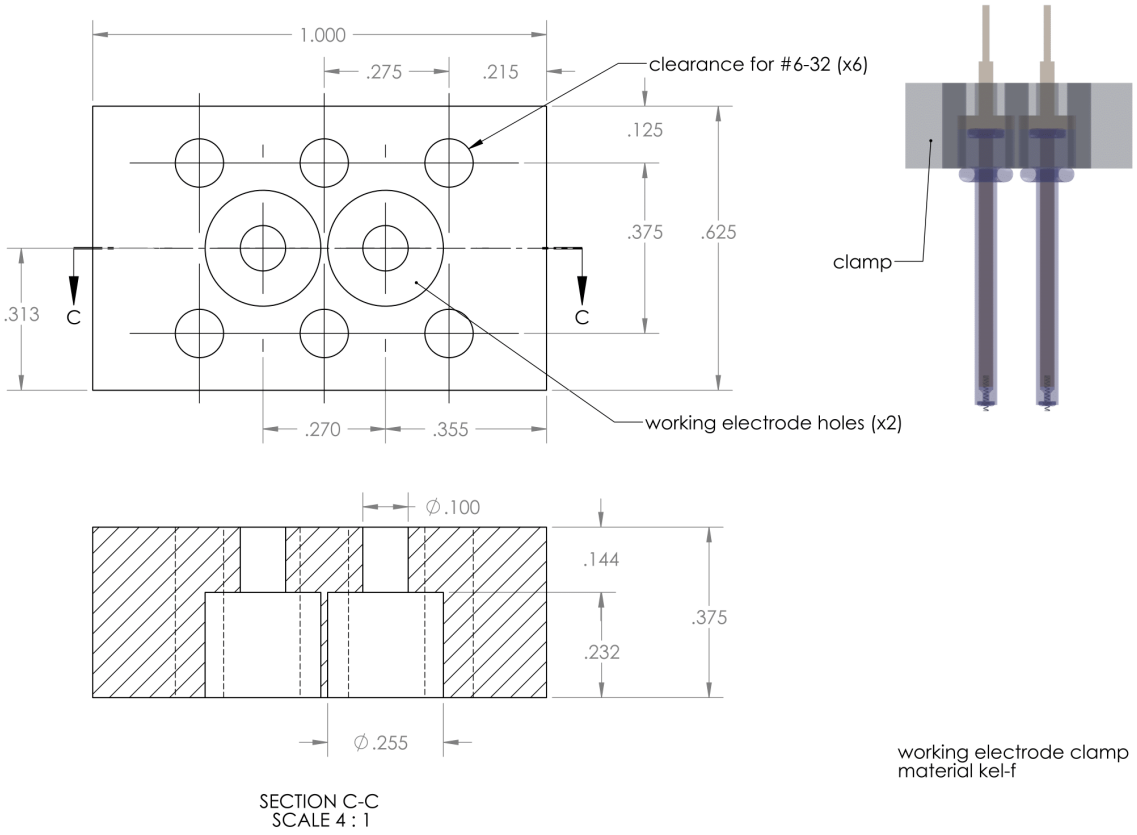

Figure A10. CAD drawing of working electrode clamp for transmission cell

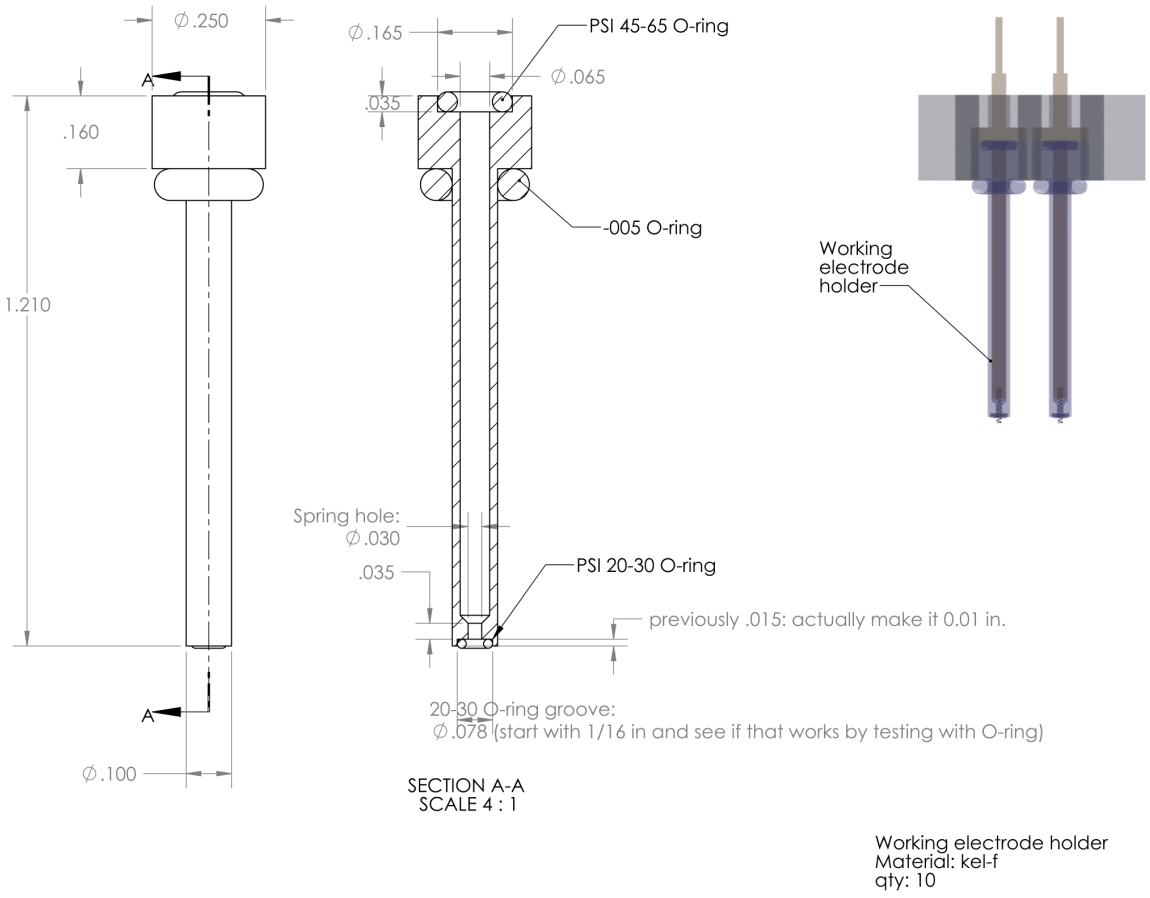

Figure A11. CAD drawing of working electrode holder for transmission cell

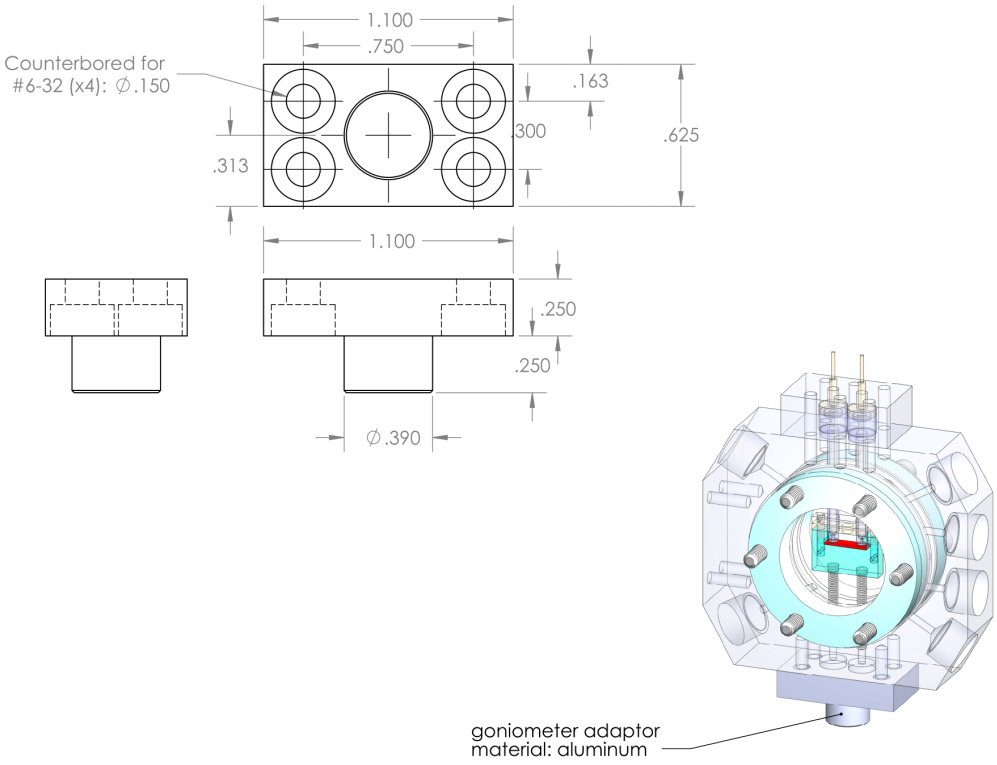

Figure A12. CAD drawing of goniometer adaptor for transmission cell

Appendix B Patterson function analysis of multilayer XRR

Patterson function analysis mainly includes 2 parts. The first part is the calculation of Patterson function from low-angle X-ray reflectivity data. This part has been thoroughly discussed in Chapter 4. This calculation contains 2 steps, which are XRR normalization and Fourier transformation. After Fourier transformation, the XRR data are converted into Patterson function. Then the layer thicknesses and the density contrast can be directly figured out (model-independent). The second part is the model fitting of Patterson function. Based on the pre-knowledge obtained in the first part and other sources, we can build an approximate structure as the initial state for fitting. This structure is presented as the format of electron density profile. This profile is a function of layer thicknesses, interface roughnesses and layer electron densities. As the Patterson function equals to autocorrelation of the derivative of the electron density profile, the least squares fitting routine is used to optimize these parameters and make the best match of them. After fitting process, the optimized parameters will be used to form the fitted structure (mode-dependent).

Following are the MATLAB codes for analysis process. The origin codes (scripts and functions) and analysis examples can be found in the digital documents for this thesis.

B.1 Convert low-angle X-ray reflectivity into Patterson function

Script name	Patterson_selfmode.m
Required function	FT_directqtox.m
Input	Low-angle reflectivity (Q and intensity)
Output	Fresnel-normalized reflectivity and Patterson function
Application	Patterson function calculation

```
%% data and parameter input
scan = 120; % scan number (only for plot legend)
load scan120.norm % data file for low-angle XRR (Q and intensity)
q = scan120(1:400,1); % momentum transfer Q
intens = scan120(1:400,3); % measured intensity
norm = mean(intens(1:15));
intens = intens/norm; % nomalize XRR (based on the total reflection)
clat =5.4; % substrate d-spacing along surface normal
q2 = q;
beta =0.6; % parameter for the roughness of substrate surface (0<beta<1)
qc = .03; % critical angle


%% calculation of Fresnel reflectivity
roughness = (1-beta^2)./(1+beta^2-2*beta*cos(q*clat))./(4*sin(.5*q*clat).^2);
rnorm = (1-beta^2)./(1+beta^2-2*beta*cos(qc*clat))./(4*sin(.5*qc*clat).^2);
roughness = roughness/rnorm;
sigma = beta^.5/(1-beta)*clat;
fresnel = (q2/qc - .00001).^-4.*roughness;
fresnel(q2<qc)=1;
```

```
%% calculation and plotting of patterson function
subplot(3,1,1) % measured reflectivity and Fresnel reflectivity
semilogy(q,intens); hold on;
semilogy(q,fresnel,'--'); hold off;
xlabel('q'); ylabel('R');
title(['Scan ' num2str(scan) ]);
ylim([1e-10,2]); xlim([0 .72]);
legend('reflectivity',['fresnel (\sigma = ' num2str(sigma) ')']);

subplot(3,1,2) % Fresnel-normalized reflectivity
reflnorm = intens./fresnel;
semilogy(q,reflnorm); xlim([0 .72]);
xlabel('q'); ylabel('R/R_F');
zmax = 1000;

subplot(3,1,3); % Patterson function
qlo = 2*qc; qhi = .4; % range for Fourier transform
[x,Patt] = FT_directqtox(q(qlo<q ),reflnorm(qlo<q),1,zmax); % FT
plot(x,Patt,'r');
xlabel('z (Ang)'); ylabel('FT(R/R_F)');
ylim(1.5*[min(Patt),-min(Patt)]);
set(gcf,'PaperPosition',[1 1 5 6]);
print('-f1','-djpeg', ['GeTi_scan' num2str(scan)],'-r600')
```

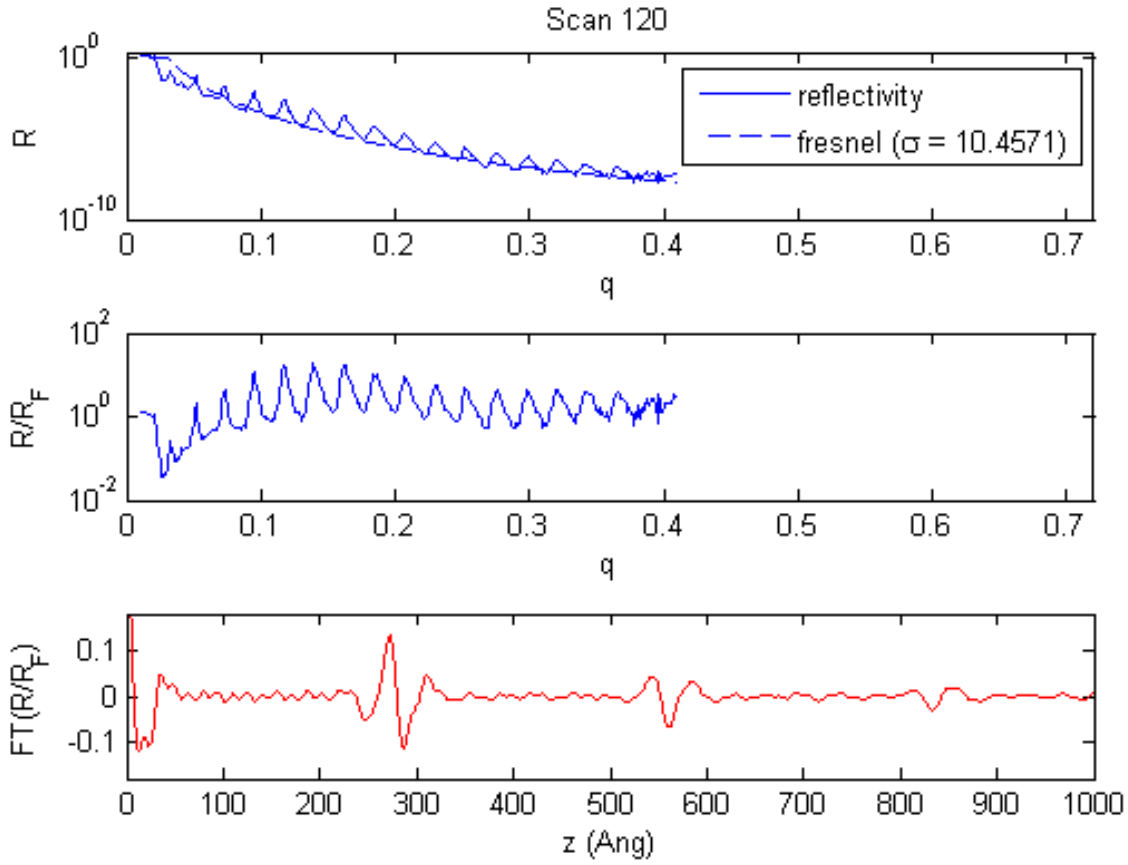

Figure B1. Output example of "Patterson_selfmode.m"

The main idea for Patterson function calculation is normalizing measured reflectivity by substrate Fresnel reflectivity and then performing Fourier transform on it. In the "parameter input" part, we need to adjust the substrate roughness (beta) and critical angle (qc) to make the normalized reflectivity (R/R_F, as shown in Figure B1 middle) varying around 1 as close as possible. Then the Fourier transform of the Fresnel-normalized reflectivity will give out the Patterson function (as shown in Figure B1 bottom).

Script name	XRRmap.m
Required function	None
Input	Low-angle reflectivity (Q and intensity) Patterson function (z and value)
Output	2D color map or curve set of input data
Application	Plotting 2D color map or curve set for a series of reflectivity or Patterson functions from *in situ* measurements

```
scan = [58 61 76 82 88 91 96 99 105 120 132 145 157 173 177];

%% color map
d2 = [];
for ii = 1:length(scan)
   dat = dlmread(['scan' num2str(scan(ii)) '.norm']);
   d2 = [d2 dat(:,2)];
end %data input
q = dat(:,1); % momentum transfer
d2 = log(abs(d2)); %log scale of reflectivity
time=1:1:length(scan);
q_i=q(1):(q(2)-q(1))/2:q(length(q)); % horizontal interpolation scale (1
point between each data point)
time_i=time(1):(time(2)-time(1))/20:time(length(time)); % vertical
interpolation scale (19 points between each data point)
d2_i=[];
for i=1:length(q_i) % interpolation
    for j=1:length(time_i)
        d2_i(i,j)=interp2(time,q,d2,time_i(j),q_i(i));
    end
end
```

```
figure (1)
imagesc(q_i',time_i',d2_i');figure(gcf);



%% curve set
figure (2)
set(gcf,'paperposition',[1 1 5 6]);
set(gcf,'position',[800 0 800 800]);
for ii = 1:length(scan) % plot curves one by one with fixed vertical offsite
   dat = dlmread(['scan' num2str(scan(ii)) '.norm']);
   plot(dat(:,1),-ii*.5+dat(:,2)/max(dat(:,2)*1.5),'-r','color',
        [ii/length(scan),0,1-ii/length(scan)],'LineWidth',2);
   hold on;
end
xlim ([0 0.6]);
ylim([-7.9 0]);
set(gca,'FontSize',20);
hold off;
```

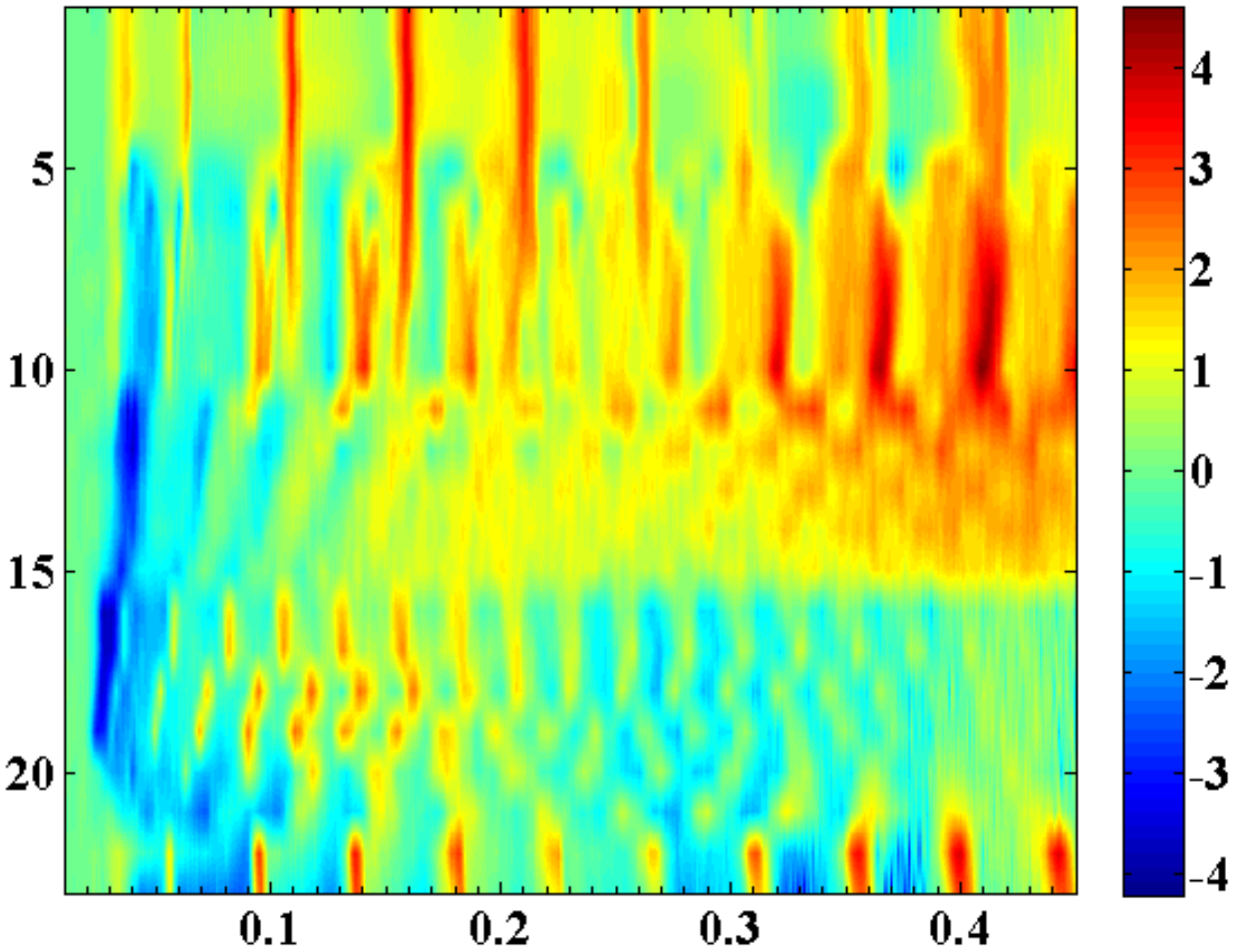

Figure B2. Output example of reflectivity 2D color map

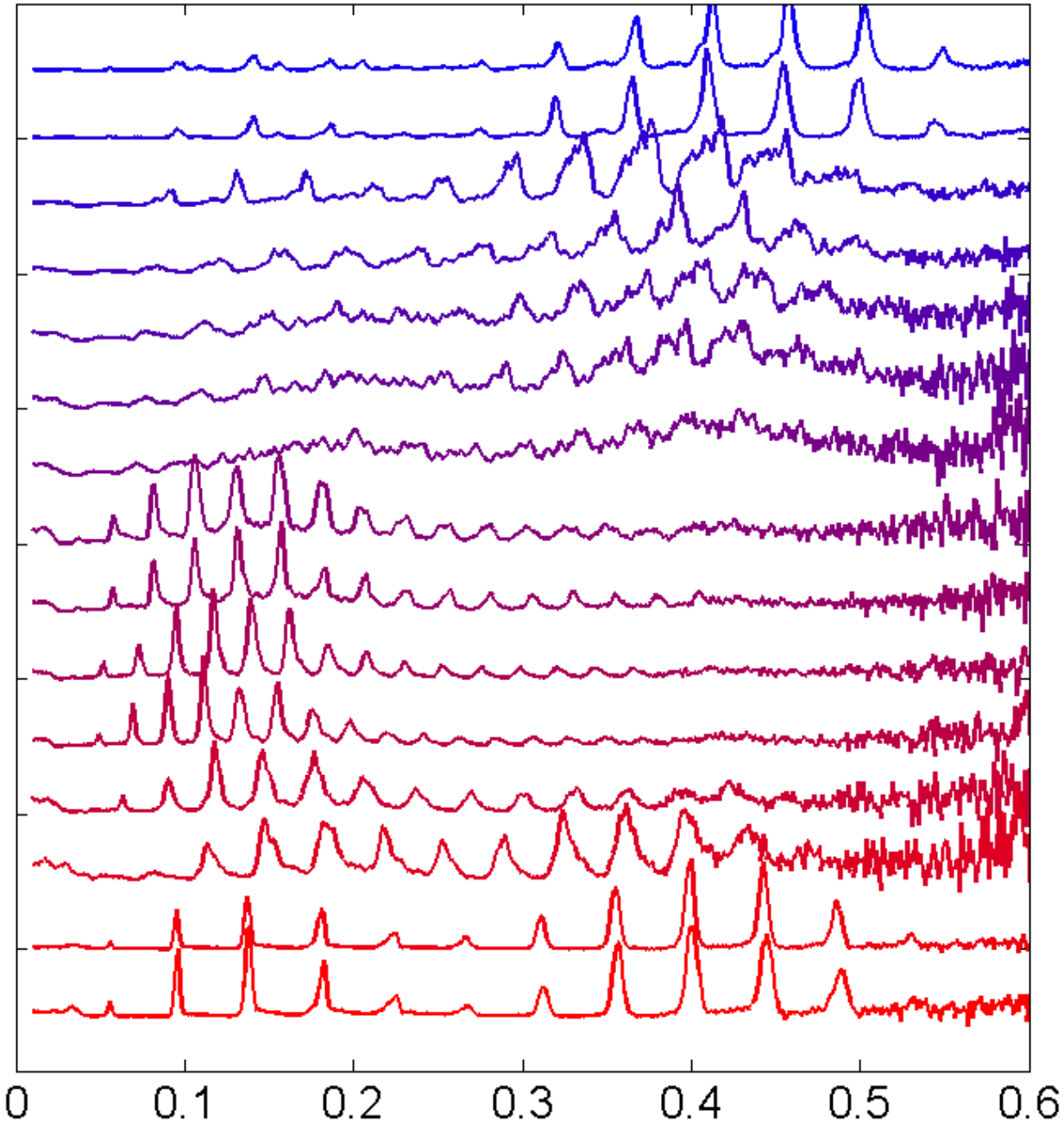

Figure B3. Output example of reflectivity curve set

B.2 Patterson function fitting

Script name	Patt_fit_4L.m
Required function	fACF_4L.m dfdppf_2014.m leasqrpf_2014.m
Input	Patterson function and estimated film parameters
Output	Fitted Patterson function and film electron density profile
Application	Fitting the Patterson function of a multilayer thin film with 4 layers in one unit cell

```
mul=20; % how many unit cells
z1=7.4; % layer 1 thickness
z2=7.4; % layer 2 thickness
z3=7.4; % layer 3 thickness
z4=116; % layer 4 thickness
z=z1+z2+z3+z4; % one unit cell thickness
sigma12=2; % related to roughness of interface layer1-layer2
sigma23=2; % related to roughness of interface layer2-layer3
sigma34=2; % related to roughness of interface layer3-layer4
sigma41=2; % related to roughness of interface layer4-layer1
rho1=40; % electron density of layer 1
rho2=36.6; % electron density of layer 2
rho3=rho1; % electron density of layer 3
rho4=36.4; % electron density of layer 4
scan=load ('Patt_scan61.txt'); % data input
```

```
param0=[z1, z2, z3, z4, sigma12, sigma23, sigma34, sigma41, rho1, rho2, rho3,
rho4]; % initial parameter table

x=scan(:,1); % distance z
sig=scan(:,2); % patterson function

max_step =[0.2*[1,1,1,1],  0.01*[1,1,1,1],  0.2*[1,1,1,1]]'; % maximum fitting
range for each parameter
dp =0.0001*[[1,1,1,1],      [1,1,1,1],        [1,0,1,1]]'; % fitting step for
each parameter
options = ones(length(param0),2);
options(:,1) = 0.001*options(:,1);
options(:,2) = max_step;

eb = 0.05*sqrt(abs(sig));  % error bar making up (use real ones if data have)
ebmin = 0.005;
eb = (eb<0.01)*ebmin + eb;
wt = 1./eb;

xmin = 70;
xmax = 200;
wt = wt.*(x>xmin).*(x<xmax)+1e-16; % define fitting range

% Least squares fitting
for i=1:5  % number of fitting runs
[CALC,p,stdev,kvg,iter,corp,covp,covr,stdresid,Z,r2,schi2]=leasqrpf_2014(x,si
g,param0,...
    'fACF_4L',0.0001,200,wt,dp,'dfdppf_2014',options);
param0=[p(1),p(2),p(3),p(4),p(5),p(6),p(7),p(8),p(9),p(10),p(11),p(12)];
end

% rebuild the electron denisty profile from fitting results
z=p(1)+p(2)+p(3)+p(4);
rho=0;
```

```
for i=1:mul
    rho=rho...
        +p(9)*box_self(x,(i-1)*z, (i-1)*z+p(1))...
        +p(10)*box_self(x, (i-1)*z+p(1), (i-1)*z+p(1)+p(2))...
        +p(11)*box_self(x, (i-1)*z+p(1)+p(2), (i-1)*z+p(1)+p(2)+p(3))...
        +p(12)*box_self(x, (i-1)*z+p(1)+p(2)+p(3), i*z);
end

figure(1); % plot of fitted electron density profile
plot(x,rho);
xlim ([0.01 1.5*z]);

figure(2); % comparing plotting of original and fitted Patterson function
plot(x)
plot(x,CALC);
hold on;

plot (scan(:,1),scan(:,2),'-r');
xlim ([0.01 1.5*z]);
hold off;
```

*In digital documents, I have also included the fitting script for 2 layers model (i.e. 2 layers in one unit cell) under the name of “Patt_fit_2L.m”.

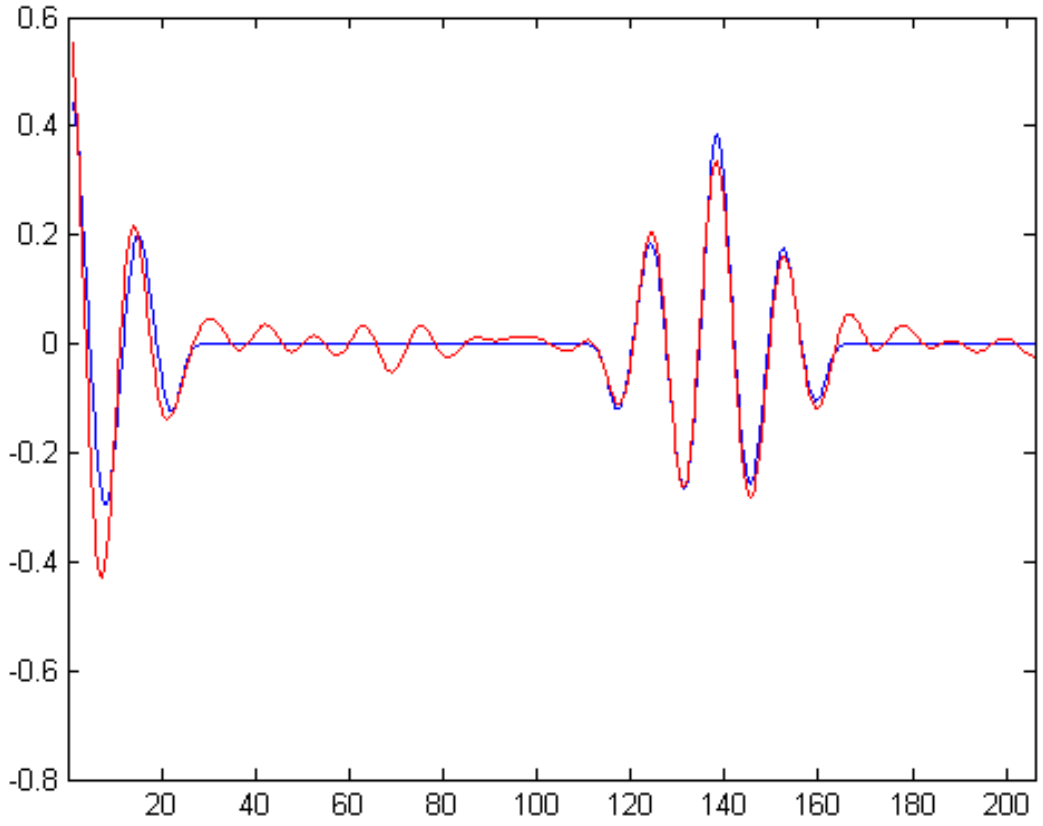

Figure B4. Output example of Patterson funtion fitting

The initial input parameters are directly figured out from Patterson function, which are estimated numbers. These initial input parameters are used to calculate the autocorrelation of the derivative of the electron density profile. Then the calculated autocorrelation function is compared with Patterson function and optimized through least squares method. After a few of fitting runs, the fitted autocorrelation function is compared with original Patterson function and plotted as the output image.